Tracking volcanic plume thermal evolution and eruption source unsteadiness in ground-based thermal imagery using spectral-clustering

Colin Rowell[1], Mark Jellinek[1], and Johanand Gilchrist[1]

[1]University of British Columbia

September 26, 2023

Tracking eruption column thermal evolution and source unsteadiness in ground-based thermal imagery using spectral-clustering

C. R. Rowell[1], A. M. Jellinek[1], J. T. Gilchrist[1]

[1]Department of Earth, Ocean, and Atmospheric Sciences, University of British Columbia, Vancouver , British Columbia , Canada

Key Points:

- Unsupervised machine learning algorithm tracks evolving plume structures in thermal imagery at Sabancaya Volcano.
- Temperature evolution in both space and time reflects unsteady transitions between steady plume and discrete thermal regimes.
- We propose a quantitative unsteadiness metric for the prediction of entrainment regimes as a function of eruption source unsteadiness.

Corresponding author: Colin R. Rowell, `crowell@eoas.ubc.ca`

Abstract

Volcanic eruption columns typically have unsteady source conditions, where mass and heat fluxes from the vent evolve or fluctuate on time scales from seconds to hours. However, integral plume models routinely assume source conditions that are statistically stationary, and the degree to which source unsteadiness influences the mechanics of column rise and air entrainment has not been established with quantitative predictions. We address this knowledge gap by examining eruptions with varying unsteady character at Sabancaya Volcano, Peru. Using a novel tracking algorithm based on spectral clustering, we track the spatiotemporal evolution of coherent turbulent structures in columns using ground-based, thermal infrared imagery. For turbulent structures tracked in time and space, we calculate the power law decay exponent of excess temperature with height. In general, the starting pulses of transient events are characterized by power law exponents matching theoretical predictions for an instantaneous point release of buoyancy (i.e. a thermal), which evolve with sustained emissions to values consistent with steady plumes. Our results support previous findings from field evidence and laboratory experiments that entrainment and gravitational stability in unsteady volcanic columns are inadequately captured by time-averaging or constant entrainment coefficients. We propose a quantitative definition for column source unsteadiness which captures the timing and magnitude of source fluctuations on time scales that influence entrainment mechanics, and which provisionally predicts our observed differences in power law behavior. We argue for systematic experimental and numerical studies of the relationship between source unsteadiness and entrainment to develop unsteady entrainment parameterizations for integral plume models.

Plain Language Summary

Volcanic eruptions are routinely simulated as sustained, jet-like flows of gas and ash. However, most eruptions in nature are unsteady at the source vent, meaning the flow rate and heat content of erupted material varies substantially over time scales ranging from seconds to hours. This variation impacts mixing of eruption plumes with the background atmosphere (a process called entrainment), ultimately affecting how high plumes rise and where they disperse hazardous ash. To better understand how unsteady conditions influence eruption behavior and hazard, we analysed infrared camera imagery of eruption plumes at Sabancaya Volcano, Peru. By developing a new algorithm which tracks individual turbulent eddies in the rising plume, we measure how the heat content in the plumes evolve with entrainment of atmosphere. Our measurements show the plume mixing process evolving between theoretical predictions for sustained, jet-like flows and single, brief pulses, as a result of unsteady, evolving conditions at the plume source. We use our measurements to propose a mathematical framework for quantifying unsteadiness in volcanic plumes, enabling future experiments and computer simulations that include unsteady effects. Ultimately, this will lead to improved forecasts of ash dispersal and resulting hazards for unsteady eruptions.

1 Introduction

Accurate, real-time characterization of the dynamics and behavior of explosive volcanic eruptions is a cornerstone objective of modern volcano hazard monitoring. The type, timing and severity of hazards related to ash clouds and pyroclastic density currents depend on the gravitational stability, rise height and wind dispersal of eruption columns (Sparks & Wilson, 1976; Bonadonna et al., 2015; Cole et al., 2015; Prata & Rose, 2015). For example, initially dense volcanic jets of ash, pyroclasts and entrained gases can evolve to become positively buoyant plumes and generate tall convective columns through turbulent entrainment, mixing, and thermal expansion of ambient air into the column interior, and through particle loss and sedimentation. We use 'jet" herein to refer to sustained momentum-driven flows, while "plume" defines flows driven predominantly by the buoyancy of the erupted mixture, and "column" refers generally to buoyantly rising volcanic flows. Evolution of volcanic columns above the vent and the resulting partitioning of erupted ash and gas between buoyant, wind-dispersed clouds and locally destructive pyroclastic density currents depend critically on the "vent source conditions" such as mass flow rate of magma, gas, content, vent shape, and particle size distribution, as well as local atmospheric stratification and wind profiles. (Sparks, 1986; Woods, 1988, 1995, 2010; Koyaguchi et al., 2010; Degruyter & Bonadonna, 2013; Jessop & Jellinek, 2014; Aubry et al., 2017; Lherm & Jellinek, 2019; Gilchrist & Jellinek, 2021). Assessment of characteristic or average vent source conditions that are critical inputs for eruption models is, however, challenging. In addition to being extremely challenging to observe visually or infer, vent source conditions are typically time-varying, or "unsteady". Fluctuations in vent source conditions on timescales of seconds to hours are ubiquitous during explosive volcanism, but their effects on eruption behavior are poorly understood and remain a core challenge in understanding the dynamics and hazards of volcanic columns and ash clouds (National Academies of Sciences, 2017).

Conventional models of the dynamics of large eruption columns (e.g. Sparks & Wilson, 1976; Sparks, 1986; Woods, 1988) are based on theory for statistically steady vent source conditions defined in terms of time-averaged mean mass, momentum and buoyancy fluxes. Intrinsically unsteady processes related to turbulent fluctuations are treated with insightful closures including the "entrainment hypothesis", where the rate of turbulent atmospheric entrainment is proportional to the mean rise speed (Morton et al., 1956; Morton, 1959; Turner, 1986). Sustained Plinian eruptions, for example, are often approximated as steady buoyant plumes and analyzed with corresponding integral (1D) column models (Morton et al., 1956; Woods, 1988, 2010; Degruyter & Bonadonna, 2013; Woodhouse et al., 2013). In this framework, the time-averaged radial velocity, density, and temperature profiles across the plume are self-similar (i.e. of the same functional shape) with height and evolve with the release of gravitational potential energy and with progressive turbulent entrainment (Morton et al., 1956). The statistically steady flows of jets and plumes also have opposite end-members, respectively instantaneous, point-releases of momentum (i.e. "puffs", Richards, 1965) and buoyancy (i.e. a "thermal", Morton et al., 1956; Turner & Taylor, 1957; Turner, 1986), as shown in Figure 1.

How best to identify the behavior regimes in which time-averaging is appropriate in order to enable an analysis with steady-state column models is not straightforward, and unsteady source conditions span a continuum of behaviours. Over time scales of seconds to days, eruptions can evolve from approximately steady momentum-driven jets or buoyant plumes to discrete pulses or rising puffs and thermals (Anilkumar, 1993; Clarke, Voight, et al., 2002; Clarke, Neri, et al., 2002; Patrick et al., 2007; Patrick, 2007; Scase, 2009; Webb et al., 2014; Chojnicki et al., 2014, 2015a, 2015b; Dürig et al., 2015; Woodhouse et al., 2016; Tournigand, Taddeucci, et al., 2017). Evolution between regimes of steady and unsteady behavior occurs as conditions in the conduit evolve from the initial opening of the vent, progressive fragmentation, modification of vent geometry, varying access to external water, and depletion of available magma and volatile mass (Gonnermann & Manga, 2007; Carey et al., 2009; Hreinsdóttir et al., 2014; Houghton et al., 2015). Unsteady behavior is, for example, inherent in transient events (i.e. short-lived relative to the column rise time) such as Strombolian bursts (Patrick, 2007) and Vulcanian explosions (Clarke, Voight, et al., 2002; Clarke et al., 2009), but is also very common during sustained eruptions (Scase, 2009; Dürig et al., 2015). Discrete Vulcanian explosions characteristically produce thermals as well as predominantly momentum-driven starting jets (Turner, 1962) characterized by a rapid initial peak in vent mass and momentum fluxes, followed by periods of sustained flow or rapid decay (Clarke, Voight, et al., 2002; Patrick, 2007; Scase, 2009; Chojnicki et al., 2014). Such evolving source fluxes drive evolutions between convective columns and collapsing pyroclastic density currents (Clarke, Neri, et al., 2002). Eruptive phases may be unsteady in time and also vary spatially: Clarke,

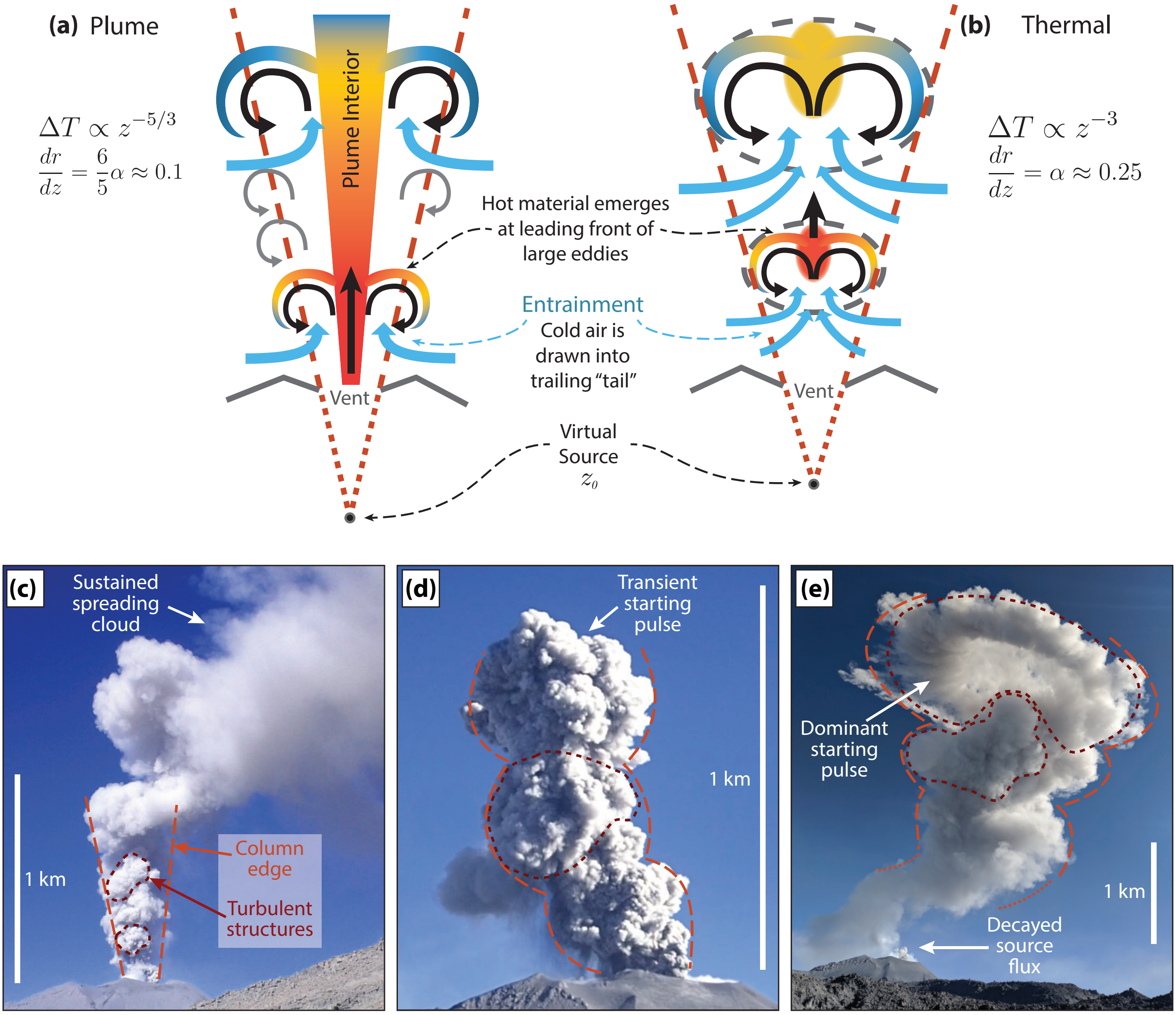

Figure 1. Example images of eruptive events at Sabancaya Volcano. Varying degrees of unsteady or transient source behavior lead to complex evolutions of column governing dynamics and morphology. (a-b) Theoretical geometry and theoretical temperature power law evolution with height, in an unstratified ambient environment, above a virtual source for plumes (a) and thermals (b). Dashed orange lines show the evolution of an effective column radius with height. (c) A sustained plume characterized by low-amplitude fluctuations in mass flux about a well-defined mean flow (May 25, 2018; Event 1 , this study). (d) A complex explosion fed by multiple discrete pulses from the vent (May 27, 2018; not used in this study). (e) A highly transient, Vulcanian-type explosion, characterized by a single dominant starting pulse which evolved into a discrete vortex ring, followed by a small number of rapidly decaying secondary pulses (May 25, 2018, about 5 minutes after onset; Event 3, this study). In panels (c) to (e), orange dashed lines highlight the overall column shape, and black dashed lines highlight coherent turbulent structures that govern the largest scales of column motion and evolution.

Voight, et al. (2002) noted the presence of multiple jet-like sources contributing to the total flux of Vulcanian eruptions at Soufrierre Hills volcano, and the spatial location of jet sources is frequently observed to vary in time (Webb et al., 2014). Unsteady or pulsating source conditions are also characteristic of many hydrovolcanic eruptions, for example as a result of episodic explosions driven by molten-fuel-coolant interactions or drying of volcanic vents (Brand & Clarke, 2009; Carey et al., 2009; Houghton et al., 2015; Zimanowski et al., 2015). Theoretical integral models of unsteady plumes have seen promising developments in recent years (Scase et al., 2006; Scase, 2009; Craske & van Reeuwijk, 2016; Woodhouse et al., 2016; Craske, 2017), but remain to be applied to the case of dense, particle laden flows typical of unsteady volcanic eruptions, which may involve mass flow rates that vary over orders of magnitude within seconds to minutes (Dürig et al., 2015; Tournigand, Taddeucci, et al., 2017).

Entrainment of ambient atmosphere into turbulent columns is a consequence of lateral pressure variations and shear instability along the flow margins (Tritton, 1988). The largest overturning eddies engulf ambient air and turbulent motions at progressively smaller scales ultimately mix entrained air mechanically and thermally into the column interior as shown schematically in Figure 1 (Morton et al., 1956; Turner, 1986; Tritton, 1988). For jets, plumes, or thermals with self-similar cross-sectional profiles, the entrainment hypothesis relates the entrainment velocity of ambient air as linearly proportional to the mean axial rise speed v by an entrainment coefficient α (Figure 1a,b) (Morton et al., 1956; Turner, 1986). An alternative entrainment parameterization relates turbulent shear stresses to the square of axial column velocity, and has recently been employed in unsteady column models in particular (Priestley & Ball, 1955; Morton, 1971; Craske & van Reeuwijk, 2016; van Reeuwijk et al., 2016). Measured and simulated entrainment rates are generally higher for plumes than for jets, and higher for pulsatory and instantaneous sources than those for both steady jets and plumes (Turner, 1962, 1986; Clarke, 2013; Chojnicki et al., 2015a). The coefficient α further varies depending on the assumed form of the axial velocity and density profiles (Turner, 1962). Typical values for momentum-driven jets are $0.06 \leq \alpha \leq 0.08$, and for buoyant plumes $0.09 \leq \alpha \leq 0.16$ (Morton et al., 1956; Turner, 1973; Linden, 2000; Kaminski et al., 2005; Carazzo et al., 2006). By contrast, entrainment into discrete thermals is dominated by the overturn of a single, large vortex ring and $\alpha \approx 0.25$ (Turner, 1969).

More generally, both observational and experimental studies show that variations in entrainment rates of ambient air into unsteady jets and plumes are governed by local balances of momentum and buoyancy among individual large, coherent vortices, the characteristics of which depend strongly on the time and spatial evolution of the vent source (Turner & Taylor, 1957; Turner, 1962; Kaminski et al., 2005; Carazzo et al., 2008a; Chojnicki et al., 2014, 2015b; Tournigand, Taddeucci, et al., 2017). The dependence of α on local conditions means that unsteadiness in source velocity and gas content can be expected to directly impact the entrainment, mixing, and thermal evolution of ash columns. Furthermore, the self-similarity of radial velocity and density profiles on which integral column models rely is known to develop only at some distance downstream of the source (Carazzo et al., 2006; Jessop et al., 2016), and is further perturbed by unsteady fluctuations in source conditions (Craske & van Reeuwijk, 2016). Many commonly applied column models do not capture this complexity and are therefore not appropriately applied for conditions immediately above the vent elevation, which is significant given the importance of near-source dynamics in governing behaviors such as column collapse. There is a need for both observational and modelling approaches that account for the complex and unsteady evolution of volcanic flows near the source. Though routinely observed in explosive volcanism, a self-consistent description of unsteadiness and its consequences for entrainment in eruption columns remains elusive.

Studies of explosive volcanism using ground-based infrared imagery frequently focus on tracking the shape and height evolution of columns and relating these quantities to theoretical predictions (Patrick et al., 2007; Harris, 2013; Valade et al., 2014; Webb et al., 2014; Bombrun et al., 2018; Tournigand et al., 2019). Here rather than directly attempting to measure entrainment via column morphology, we explore the use of a broadband infrared camera to compare the temperature evolution of unsteady volcanic columns against theoretical predictions. The theoretical evolution with height of temperature and velocity profiles of thermals and steady plumes can be described solely as a function of distance from a virtual source height z_0: a theoretical point at which a column has zero volume but finite buoyancy (see Figure 1). The evolution of buoyancy may be related to the column excess temperature ΔT through the reduced gravity:

$$g\beta\Delta T(z) = g\frac{\rho_a(z) - \rho_p(z)}{\rho_0}, \tag{1}$$

where g is gravitational acceleration, β is the volumetric coefficient of thermal expansion and ρ_a and ρ_p are densities of the ambient air and column, and ρ_0 is a reference density. The local excess $\Delta T(z)$ is defined as the temperature above the background atmospheric profile $T_a(z)$:

$$\Delta T(z) = T_p(z) - T_a(z), \tag{2}$$

where T_p is the column absolute temperature. Note that the linear relation between temperature and density in Equation 1 applies for buoyant plumes where the ash mass fraction in the column is less than about a few tens of percent, which is generally the case for columns that are positively buoyant. These equations further assume that the ash contribution to bulk density is not changing very rapidly due to sedimentation, compared to rates of entrainment and gravitational potential energy release. On dimensional grounds, and assuming a steady and self-similar evolution, ΔT will evolve as a power law function of altitude above the virtual source. The power law exponent B differs for plumes and thermals (Turner, 1969):

$$\Delta T_{plume}(z) \quad \propto F_p^{2/3}(z - z_0)^{-5/3}, \tag{3}$$
$$\Delta T_{thermal}(z) \qquad \propto F_t(z - z_0)^{-3}, \tag{4}$$

where F_p is the source buoyancy flux for a plume (units of m^4/s^3) and is the F_t total source buoyancy for thermals (units of m^4/s^2). The extent to which unsteady source conditions modify the thermal evolution of natural plumes to be between the steady-state plume and thermal limits is unexplored. An important consideration is that the form of Equations 3 and 4 strictly applies for plumes and thermals in unstratified ambient conditions. We apply our quantitative analysis below using Equations 3 and 4 over sufficiently limited altitude windows and assuming straight-sided solutions to the plume equations, such that we expect the unstratified solutions to provide a reasonable approximation (Caulfield & Woods, 1998; Kaye & Scase, 2011; Bhamidipati & Woods, 2017). However, we revisit this assumption in greater detail in Sections 3.7 and 5.1. We also neglect the effects of wind-driven stirring and entrainment, which are evident at altitudes above our analysis windows where thermal contrasts are small or unresolved. We note that for much taller columns than Events 1-3 or larger magnitude Plinian events, effects of stratification and wind should be included in this type of analysis.

To track the time-varying evolution of velocity and temperature profiles, or characterize evolving or complex column morphologies as shown in Figure 1, we identify and track the turbulent structures associated with individual pulses from the source vent in thermal imagery. Our problem requires separating the largest turbulent motions arising from individual column pulses from the complex and moving background of the column exterior. The advent of advanced video segmentation (feature identification and classification) algorithms including Recurrent Convolutional Neural Networks (R-CNN's) and Long Short-Term Memory Networks (LSTM-CNN's) provides a promising way forward for rapid and automated quantitative analyses of video and thermal imagery (e.g. Witsil & Johnson, 2020; Wilkes et al., 2022). However, such supervised machine learning techniques require extensive training with well-curated data sets from field and laboratory studies or simulations spanning the full range of spatio-temporal dynamics involved in the evolutions shown in Figure 1 and that we characterize in detail below. Such data currently do not exist. Consequently, we use a novel but time-intensive algorithm that combines spectral clustering, an unsupervised machine learning technique (von Luxburg, 2007; Jia et al., 2014), with physics-informed constraints to automatically identify and track coherent and evolving column structures.

We apply our structure tracking algorithm to track the rise of turbulent structures in thermal imagery from Sabancaya Volcano. We present analyses of 3 events: Event 1 was a long-lived (about 4 hours total duration) sustained plume with quasi-periodic pulses at 20-30 s intervals; Event 2 was an "emergent explosion" (about 2-3 minutes duration) with an initial discrete vortex ring followed by quasi-periodic emissions at 12-20 s intervals; and Event 3 was a transient Vulcanian explosion dominated by a single initial pulse and followed by a decay period consisting of multiple subsequent pulses, and with broadly decreasing peak temperature over a period of about 30 s. We have three overarching goals:

1. Track, characterize and understand quantitatively the evolution of entrainment and thermal mixing driven by fluctuating vent source conditions, laying key practical groundwork for near-real-time computer-vision and machine-learning based characterization of unsteady eruption column dynamics.
2. Demonstrate how to use ground-based, broad-band infrared imagery to constrain the entrainment and mixing properties for unsteady eruptive phases and to identify whether 1D models with parameterized average values for the entrainment coefficient α might be applied to the three eruptive phases.
3. Outline a broad framework to quantitatively define eruption source unsteadiness and its effect on column dynamics and column rise.

This manuscript is organised as follows. In Section 2 we provide an overview of the field campaign and summarize the observed character of our three studied events. In Section 3 we overview pre-processing steps performed to maximize tracking algorithm performance, summarize the tracking results, and explain the data analysis approach used to understand how the tracking algorithm can reveal unsteady dynamics. In Sections 3.1-3.2 we first perform image pre-processing that includes projection into physical coordinates, image segmentation of columns edges from background using the plumeTracker algorithm of Bombrun et al. (2018), and fitting to an atmospheric temperature profile to correct for both error in absolute temperature measurement and atmospheric stratification. In Section 3.4, we outline our method to obtain time averaged thermal images, which we will later compare with the results of structure tracking to understand differences in insights and interpretation obtained from evaluating unsteadiness versus time averaging approaches. In Section 3.5 we then summarize our algorithm based on spectral clustering to automatically track individual column pulses or coherent turbulent structures, further details of which are outlined in Appendix B. In Sections 3.6 and 3.7, we outline an approach to understand information obtained from structure tracking in terms of the dynamical behavior of rising eruption columns. In particular, we apply a curve-fitting analysis to derive the power law exponent B for each tracked structure, comparing against results from time-averaged images and from theoretical predictions for steady plumes and thermals from Equations 3 and 4. Section 4 compares inferred unsteady source evolution against the results of structure tracking and curve fitting, for both time-averaged images and for a total of 26 tracked column "structures" across the three events. In Section 5 we then build a broad view of various measures for defining source unsteadiness in volcanic columns, and propose one quantitative metric for source unsteadiness as it relates to power law decay and entrainment behavior. Following from the above description, readers may focus on the following sections according to interest: Sections 3.1-3.2 and 3.5 contain detailed information on thermal imagery data processing and structure tracking, whereas data analysis related to column behavior and unsteadiness measurements are primarily contained in Sections 3.3-3.4, 3.6-3.7, and the Results and Discussion sections.

2 Observations and Data

2.1 Field Deployment and Data Set Overview

Sabancaya is a stratovolcano of andesitic to dacitic composition, and is a secondary edifice of the larger Ampato-Sabancaya Volcanic Complex in the Southern Volcanic Zone of the Peruvian Andes (Gerbe & Thouret, 2004; Samaniego et al., 2016). The most recent eruptive episode began in November 2016 with a sequence of Vulcanian explosions, following a 4 year period of precursory seismicity and gradually increasing heat flux and sulfur dioxide outgassing (Global Volcanism Program, 2013; Coppola et al., 2022). The ongoing (as of this writing) eruptive sequence has been characterized by episodic lava dome growth, recurrent (up to several 10s per day) Vulcanian explosions, and highly variable rates of degassing (Coppola et al., 2022). Coppola et al. (2022) noted a distinct excess of outgassing volume relative to erupted magma volume, indicating relatively open system degassing fed by a shallow magma reservoir. The data we present here were recorded during Phase 3 of the eruption as identified by Coppola et al. (2022), lasting from January 2018 to March 2019 and marked by a lack of growth in the summit lava dome and a relatively stable rate of about 20 explosions per day.

During May 18 - 26, 2018, we recorded high-resolution, ground-based broadband thermal imagery of eruptive activity at Sabancaya. Eruptive activity during our observation period was highly varied, ranging from emergent to impulsive explosions, transient to pulsatory to approximately continuous, and involving emissions that were frequently ash-poor and gas-rich, though with significant variation within and between events. Though ash fall was present and recorded in the field by ash collectors and an optical disdrometer (Gilchrist, 2021), it was relatively minor across all events, consistent with previous interpretations of excess degassing during this eruptive phase (Ilanko et al., 2019; Coppola et al., 2022), and we do not report further on these data here. Some individual eruptive phases transitioned continuously among these regimes in response to vent source conditions that varied in space and time, behavior that is qualitatively similar to events described in previous studies (e.g. Clarke, Voight, et al., 2002; Patrick, 2007; Webb et al., 2014) and consistent with activity at Sabancaya throughout the most recent eruptive sequence (Global Volcanism Program, 2013; Coppola et al., 2022). Emissions were often observed simultaneously from multiple source regions within the crater. Despite fluctuations in vent source conditions, of particular and striking note was the regular recurrence interval of approximately 4.5 hours for the largest explosive events. These events were typically impulsive, relatively more abundant in ash and bombs, reaching heights between 1-4 km above the vent (about 6-9 km a.s.l.), with higher eruption velocities and temperatures frequently saturating the thermal camera at about 140°C. They were also often preceded by an obvious decay in emissions of water vapor and ash over a timescale of minutes to tens of minutes, and followed by sustained emission or periodic smaller explosions for periods of minutes to hours. We exploit the time-varying nature of the observed events to explore the effects of unsteady source emission on the dynamics and evolution with height of the resulting eruption columns.

Figure 2 shows a shaded digital elevation map (DEM) of the field area around Sabancaya. The DEM data were retrieved from the ALOS PALSAR data set via the Alaska Satellite Facility (ASF-DAAC, 2015, accessed 2018-09-17), and have a horizontal resolution of 12.5 meters. Thermal imagery was captured from observation sites 1 and 2 (slant distances to the vent location of 5.92 and 4.93 km, respectively), marked with yellow triangles. Thermal imagery was recorded using an Infratek VarioCam HD handheld thermal camera, with an average frame rate of 10 Hz (varying as a result of the internal operation of the camera). The thermal camera has a resolution of 768 by 1024 pixels, and

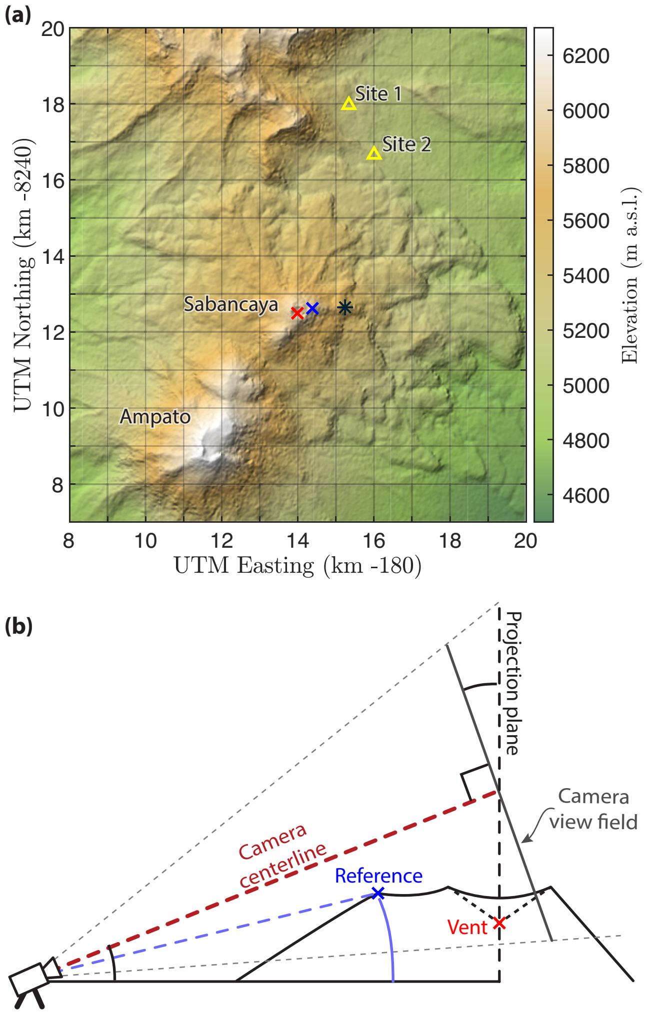

Figure 2. (a) Digital elevation map of the field area around Sabancaya Volcano. The vent location is marked with a red "X", and the blue "X" marks the location of the "reference" feature used for image projection into physical coordinates. Field observation sites are marked with yellow triangles. The black star gives the pixel center for the MODIS atmospheric profile used in analysis (see Section 3.2) for Events 1 and 3 (May 25, 2018, 12:34pm local time). The pixel center of the AIRS atmospheric profile used for Event 2 (May 24, 11:27am local time) is outside the map bounds to the East. (b) Cartoon of camera field geometry (not to scale), showing the edifice and projection plane used to convert image pixel coordinates into spatial coordinates (see Section 3.1 and Supplementary Information).

a broadband frequency range of 7.5 to 14 μm, and the data were recorded as brightness temperatures T_b.

The amplitude of recorded brightness temperatures can be affected by frequency-dependent scattering and absorption effects related to the lapse rate and water vapor content of the atmospheric volume between the camera and the erupting material, as well as the presence of water droplet clouds and aerosol particles along the optical path length. To correct for the lapse rate trend and retrieve the excess temperature according to Equations 1-4, we remove atmospheric temperature profiles $T_a(z)$ retrieved from the MODIS/Terra (Moderate Resolution Imaging Spectroradiometer, spatial resolution 5 km, Borbas (2015)) and AIRS/Aqua (Atmospheric Infrared Sounder, spatial resolution 50 km, Teixeira (2013)) satellite data sets for this location and time period. The atmospheric profiles are used to obtain the excess temperature $\Delta T(z)$. Casting the thermal imagery in the form of ΔT rather than absolute temperature or brightness temperature not only facilitates a qualitative analysis of the evolution of physical and thermal properties of a column with height and time, particularly in terms of the character and timescales of mixing with ambient atmosphere, but also allows quantitative analysis of the power law thermal evolution, as we will show below (see Section 3.2).

Table 1: Table of variables.

Variable	Description	Units
A	Structure area	m^2 or pixels
A^*	Normalized amplitude of source fluctuation	-
B	Power law exponent of temperature evolution with height	
C_{95}	Courant number using 95th percentile velocity	-
C_{mode}	Courant number using velocity mode	-
c_p	Pyroclast heat capacity	J kg^{-1} K^{-1}
dt	Time step between video frames	s
dx	Projected horizontal pixel dimension	m
dz	Projected vertical pixel dimension	m
E	Column vertical power delivery	J s^{-1}
E'	Normalized magnitude of power fluctuation	-
$\bar{E}$	Mean rate of power delivered at the column source	J s^{-1}
F_p	Column source buoyancy flux	$m^4 s^{-3}$
F_t	Thermal total source buoyancy	$m^4 s^{-2}$
i	Vertical (row) pixel coordinate	-
j	Horizontal (column) pixel coordinate	-
k	Frame (time) coordinate	-
L	Radial length scale of the largest entraining eddies	m
M	Objective function data fit term	-
n_c	Number of clusters	-
n_{c0}	Calculated optimum number of clusters	-
n_P	Number of frames used in structure tracking memory	-
n_{px}	Number of pixels in a cluster	-
N	Brunt-Väisälä frequency	s^{-1}
P	Objective function memory fit term	-
P_T	Objective function: temperature memory term	-
P_V	Objective function: velocity memory term	-
P_A	Objective function: area memory term	-
P_D	Objective function: distance memory term	-
Pu_μ	Mean State Pulsation Number	-
Pu_0	Fluid Overturn Pulsation Number	-
R	Column radius	m
R_0	Vent radius or initial eddy radius	m

Continuation of Table 1

Variable	Description	Units
T_a	Atmospheric background temperature	K
T_b	Brightness temperature	K
T_p	Column absolute temperature	K
$\bar{T}_i$	Cluster average pixel temperature	K
ΔT	Excess temperature (after atmospheric profile removal)	K
ΔT_{mode}	Mode scalar difference between T_b and T_a	K
ΔT_{95}	Subscript denotes percentile of distribution (95th percentile here)	K
ΔT_{src}	Excess temperature in a fixed image window immediately above crater rim	K
$\overline{\Delta T}_{src}$	Low-pass filtered ΔT_{src}, a proxy for mean heat flow	K
$\Delta T'_{src}$	Normalized magnitude of fluctuation about the mean $\overline{\Delta T}_{src}$	-
t	Time	s
u	Horizontal velocity	m s^{-1}
$\vec{u}$	Vector velocity field (u, v)	m s^{-1}
$\bar{V}_i$	Cluster averaged vertical pixel velocity	m s^{-1}
v	Vertical velocity	m s^{-1}
W	Scalar parameter weight	-
x	Horizontal position (perpendicular to camera view)	m
z	Height above volcanic vent level	m a.v.l.
z_0	Height of column virtual source	m a.v.l.
z_{mix}	Column mixing height or length scale	m
ϵ	Velocity tolerance scale for structure tracking	-
ε	Thermal infrared (broadband) column emissivity	-
ξ	Thermal infrared (broadband) atmospheric transmissivity	-
λ	Objective function regularization parameter	-
ρ	Column bulk density	kg m^{-3}
τ_{mix}	Time scale for column source fluctuations to become well-mixed in mean flow	s
τ_{ot}	Overturn time scale of large eddies	s
τ_{rise}	Characteristic column rise time to the neutral buoyancy level	s
Ω	Objective function for optimization	-

2.2 Thermal Imagery of Unsteady Eruption Processes

Here we analyze three recorded events spanning the range of unsteady character we observed (Figure 3, ordered from the most steady (Event 1) to the most transient (Event 3)). Events 1 and 2 were recorded from observation site 1, Event 3 was recorded from observation site 2 (see Figure 2a). The visual character and temporal evolution of the three events are summarized in Figure 3. To obtain a proxy of column source evolution with time for each event, we define a narrow windowed region of the images at a fixed height immediately above the crater rim as the "source window" (highlighted in blue in the image frames of Figure 3(a-c)). We use the statistics of excess temperature ΔT_{src} within this region as a useful proxy for the time-evolution of mass and energy flux from the volcanic vent, following Patrick et al. (2007). The source window therefore provides a picture of the character of time dependence or unsteadiness at the column source (Figure 3(d-f)).

Event 1 was a sustained ash plume lasting for a period of about 4 hours from about 05:50 to about 10:00 on May 25 (we use local time, UTC -05:00, throughout), with typical rise velocities of about 5-10 m/s. Though less dominated by distinct pulses at the source than Events 2 and 3, Event 1 had quasi-periodic fluctuations in source temperature at intervals of 10-30 seconds (dominantly about 15-18 s). Event 2, on May 24 at

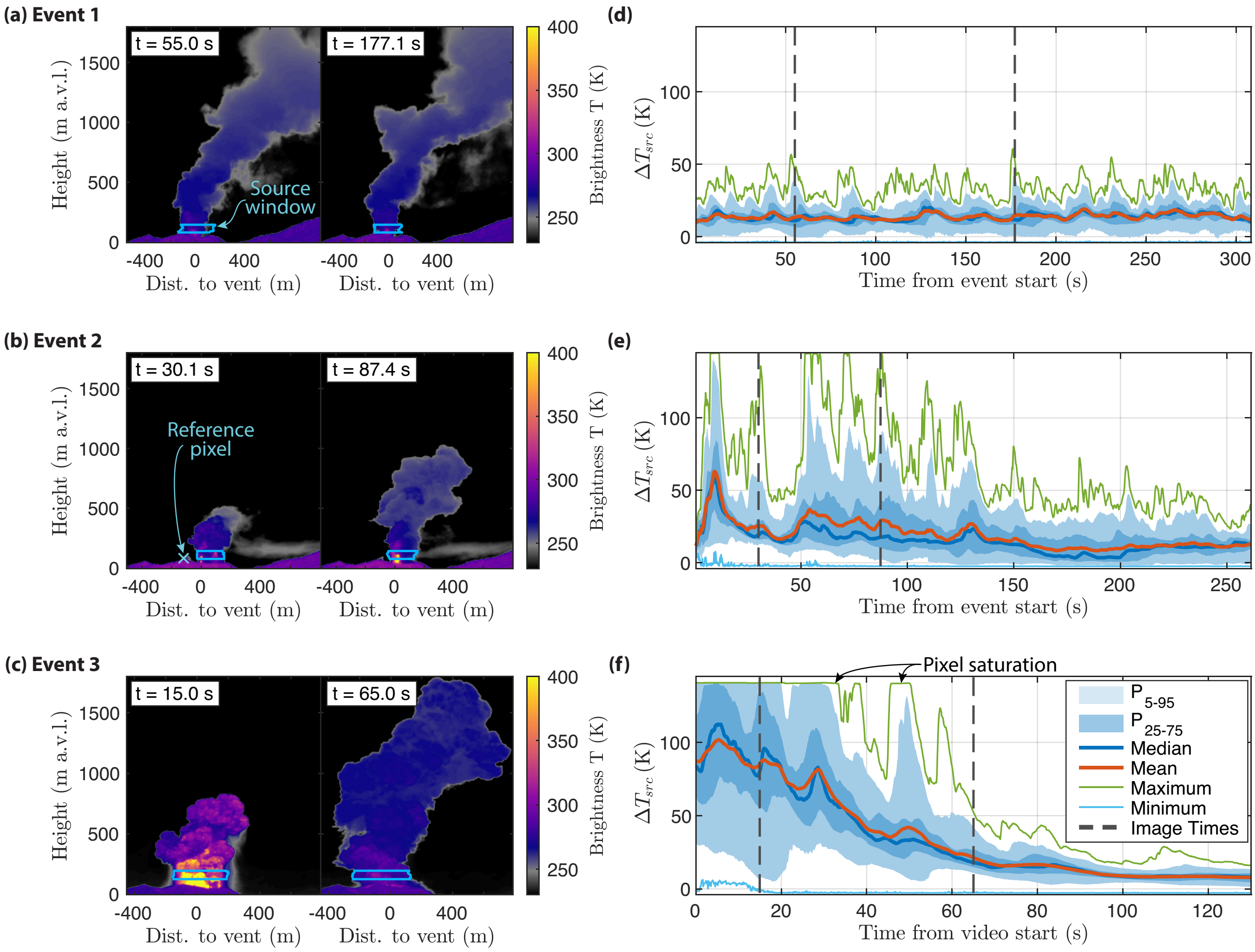

Figure 3. Three eruption events with varying character, duration, and degree of unsteady source behavior. The left column of panels - (a) through (c) - shows two example thermal images from each event, and the right column of panels - (d) through (f) - shows the corresponding time-evolution of "source" excess temperature ΔT_{src} within a thin "source window" (highlighted in blue in the thermal images). Vertical grey bars in the right column highlight the times corresponding to images in the left column. All times are given from the event start, except for Event 1, which shows video time for the data shown because the event was very long-lived. Dark blue and orange lines show the median and mean ΔT, respectively, of pixels in the source window, and the dark and light blue shaded regions give the 25-75 and 5-95 percentile ranges. The light blue line at the bottom, and the green line at the top each give the respective minimum and maximum ΔT. Note the flattened peaks of the hottest pixels for Events 2 and 3, indicating saturation of the thermal camera. See Section 3.3 for details on how the column source data are retrieved.

10:30, was an emergent starting plume, with a main duration of about 120 seconds and rise velocities of about 10 m/s, followed by continued low-intensity ash and gas emissions for a period of about 10 minutes with rise velocities of 5 m/s, eventually transitioning to continuous steam-dominated emission. As shown in Figure 3e, the main phase during the first 120 seconds was characterized by quasi-periodic pulses of hot material at intervals of about 10-20 seconds (dominant 10-15 s). Event 3 occurred on May 25 at 15:10 , and was highly impulsive and short-lived (peak mass flux occurred within the first 15 to 20 seconds, and emission largely ceased within about 60 to 90 seconds), and was broadly characteristic of a Vulcanian-type explosion (Clarke et al., 2015). Minimum velocities in the starting jet were estimated at 40 m/s, and the event was accompanied by the fallout of blocks and bombs following ballistic trajectories. Three to four distinct pulses of hot material followed the initial pulse, at intervals of approximately 7-12 seconds and with rise velocities typically 15-20 m/s, superposed on a continuous decay in mean source temperatures, as shown in Figure 3f.

Importantly, for all of the studied events the distinctive peaks in heat content in the source window are apparent in the visible column as coherent vortices, which rise and cool as they mix turbulently with entrained atmosphere. Based on the observed evolution of rise height and spreading rates (Patrick, 2007; Webb et al., 2014), Event 3 is the only event with an obvious momentum-driven gas-thrust phase, though it was only captured in time lapse thermal imagery (frame rate of about 0.25 Hz) rather than full video (see Section 4.1). No momentum-driven phase is apparent for either of Events 1 and 2, which together with relatively minor ash-fall is suggestive that the activity was driven by relatively gas rich and ash-poor eruptive phases. Because of the lack of obvious momentum-phases in the three studied events, we will chiefly focus on theory for buoyancy-driven flows (plumes and thermals) herein. We note however that the effect of momentum-driven phases would need to be accounted for in applying our methods to volcanic events more broadly.

3 Methods

In this section we summarize steps used in the structure tracking workflow and quantitative data analysis. In Sections 3.1 to 3.4 we outline the thermal imagery data preparation steps that facilitate our later quantitative analysis. An overview of the tracking algorithm is given in Section 3.5, and additional details of the internal function and design are in Appendix B. Quantitative results and implications for column dynamics are described in Section 3.6 and beyond.

3.1 Workflow Overview

The goal of the methods workflow is to track the location in time of coherent turbulent structures in the column and assess quantitatively their thermal evolution and mixing properties as a function of time and height above the vent. Accordingly, the primary output data products of the workflow are:

1. Excess temperature and 2D velocity fields $(\Delta T, u, v) = f(x, z, t)$.
2. Column source (near-vent) time history of velocity and temperature information (e.g. Figure 3d-f).
3. Location in physical coordinates (x, z, t), as well as velocity and temperature statistics of tracked column structures.
4. Evolution of radius or area and temperature with height for each tracked structure and for the time-averaged column.

To obtain the above outputs, the data processing and analysis workflow is summarized in Figure A1, and includes the following main steps:

1. Data preparation, including conversion to MATLAB format, image stabilization, and obtaining binary image masks separating column pixels from background/foreground using the **plumeTracker** code (Bombrun et al., 2018). Details of these steps can be found in Supplementary Information Section 1.1 and 1.2.
2. Projection and interpolation of image pixels into regularly sampled spatial coordinates (x, z, t) on a vertical plane relative to the volcanic vent (Figure 2b and Supplementary Information Section 1.3).
3. Estimate 2D velocity flow field using Optical Flow Analysis (Sun et al., 2014) (Supplementary Information Section 2).
4. Fit and remove satellite-derived atmospheric temperature profiles from the thermal imagery (Section 3.2 and Supplementary Information 3).
5. Retrieve temperature and velocity statistics with time for the column source (Section 3.3).
6. Generate time-averaged thermal images to compare tracking results with a steady-plume approximation (Section 3.4).
7. Run structure tracking algorithm to track coherent column structures (Section 3.5 and Appendix B).
8. Statistical analysis and curve fitting of temperature and velocity data for tracked structures (Sections 3.6 and 3.7).

Here, we briefly summarize the initial data pre-processing steps (1)-(4), and give a broad overview of the structure tracking algorithm used in step 7. After initial conversion to MATLAB data format, image registration correction was performed as necessary when windy field conditions or user operation caused shaking of the camera. To retrieve the dimensions and velocities of column structures, we project images in vertical and horizontal pixel coordinates (i, j) onto respective spatial coordinates (z, x) in a vertical plane centered above the volcanic vent as shown in Figure 2b. We use the location of a recognizable reference point on the volcanic edifice (shown in Figures 2, 3a, and Figure S2) to calculate the tilt and azimuth of the camera field of view, then calculate (z, x) for individual pixels in the thermal imagery using geometrical relationships (Harris, 2013) (See Supplementary Information Section 1.3 for a complete description of the projection equations). We numerically propagate uncertainty in the positions of the vent and reference feature to estimate uncertainty in pixel dimensions and absolute position. The projection process results in resolutions of about 3.4±0.06and 2.7±0.06 m per pixel from Observation Sites 1 and 2, respectively, and absolute positional errors of less than 60 m for ash column elements. Absolute positional errors result primarily from uncertainty in the absolute positions of the reference feature and vent, and are important only for matching satellite-derived atmospheric profiles to the data. For tracking of column structures and assessing their evolution with height, relative positional error is of greater importance and is primarily influenced by the distance between column elements and the assumed projection plane above the vent. In Section 3.2 and Supplementary Information Section 3.1 we discuss estimates of relative positional error in cases where column features lie outside of the projection plane.

We use the plume tracking and segmentation algorithm of Bombrun et al. (2018) to obtain binary masks of eruption columns for all video frames, which we use to isolate column elements for later analysis. Then, to enable quantitative analysis of image data, particularly filtering of optical flow velocity fields, we interpolate each frame onto a regular grid in spatiotemporal coordinates (x, z, t). In particular, we linearly interpolate spatial coordinates (x, z) onto a regular grid in the projection plane. We then resample the resulting gridded images in time using a piecewise cubic Hermite interpolation (Carlson & Fritsch, 1985), since the raw image frames are recorded with slightly variable time-steps. The result is a 3D array of brightness temperature data T_b with dimensions $(i, j, k) \rightarrow (z, x, t)$. Next, we estimate the 2D velocity field $\vec{u} = (u, v)$, since our structure tracking algorithm uses combined velocity and temperature information to detect and track the pixel groups corresponding to coherent turbulent structures. We use an Optical Flow Analysis toolbox (Sun et al., 2014; Tournigand, Taddeucci, et al., 2017; Smith et al., 2021), which produces a displacement vector between subsequent frames for all pixels in units of pixels/frame. Displacements are converted to velocities in m/s using the projection mapping described above (See Supplementary Information Section 2 for complete details).

3.2 Atmospheric Profile Removal

To obtain ΔT and enable a quantitative analysis based on Equations 1 and 2, we remove the atmospheric temperature profile $T_a(z)$ from the raw brightness temperature data T_b, while also applying a correction for the difference between T_b and the absolute column temperature T_p. Figure 4 gives an overview of the approach and results for this atmospheric profile fit and removal step, and further details of the methods are outlined in Supplementary Information Section 3. Figure 4a shows a schematic representation of the expected evolution with height of $T_p(z)$ in purple. The processes governing turbulent entrainment and column rise will thermally mix ambient atmosphere with the erupting column such that ΔT asymptotically approaches 0 at large height above the vent. Therefore a region exists where the excess temperature ΔT is sufficiently small that it lies within the range of column temperatures as recorded by the thermal camera. In this region, bracketed by horizontal, purple dashed lines in Figure 4a-d, the column is sufficiently well-mixed that the brightness temperature trend dT_b/dz is effectively indistinguishable from dT_a/dz, provided that the following assumptions hold:

1. the column remains thermally opaque such that no background radiation is included in column pixels;
2. the height estimates of column elements following image projection are accurate to within about 150-300 m (corresponding to a temperature change of $\sim$1 to 2 K following the lapse rate);
3. combined emmissivity and transmissivity ($\varepsilon\xi$) in the camera waveband is relatively constant with height above the vent.

Note that this does not require that the column is at thermal equilibrium with the atmosphere, as positive values of ΔT of a few K are still sufficient to drive buoyant rise. For the transient events, however, as the mass flux from the vent decays, column rise slows as $T_p(z)$ approaches thermal equilibrium with the atmosphere such that as $t \to \infty$, $\Delta T \to 0$ at all heights. The atmospheric profile fit is determined using the subset of pixels sufficiently "well-mixed" to estimate a correction factor ΔT_{mode}, which we describe below. For comparison to the theoretical picture of panel (a), panels (b)-(d) in Figure 4 show probability density functions (PDFs) of $T_b(z)$ for pixels within the ash columns of Events 1 to 3, respectively, compared against the satellite-derived temperature profiles. The atmospheric profiles are interpolated from the raw satellite vertical resolution (about 1.2 to 1.4 km) onto the z coordinate of the image projection plane.

Due to radiative losses in the camera waveband from column grey-body emissivity ε and atmospheric transmissivity ξ , we expect that T_b underestimates the value of T_p, as shown by the blue line in Figure 4a. T_b is related to T_p by the Stefan-Boltzmann Law:

$$T_b^4 = (\varepsilon\xi)T_p^4. \tag{5}$$

Here, because the values of ε and ξ are unknown for an ash-laden column, we estimate ΔT using a linear approximation for absolute temperature to recast Equation 2 as

$$\Delta T \approx T_b - \Delta T_{mode} - T_a, \tag{6}$$

where ΔT_{mode} is assumed constant (Figure 4a). Note that the approximation in Equation 6 follows from assumption (3) above *provided* that the range of ΔT is relatively small,

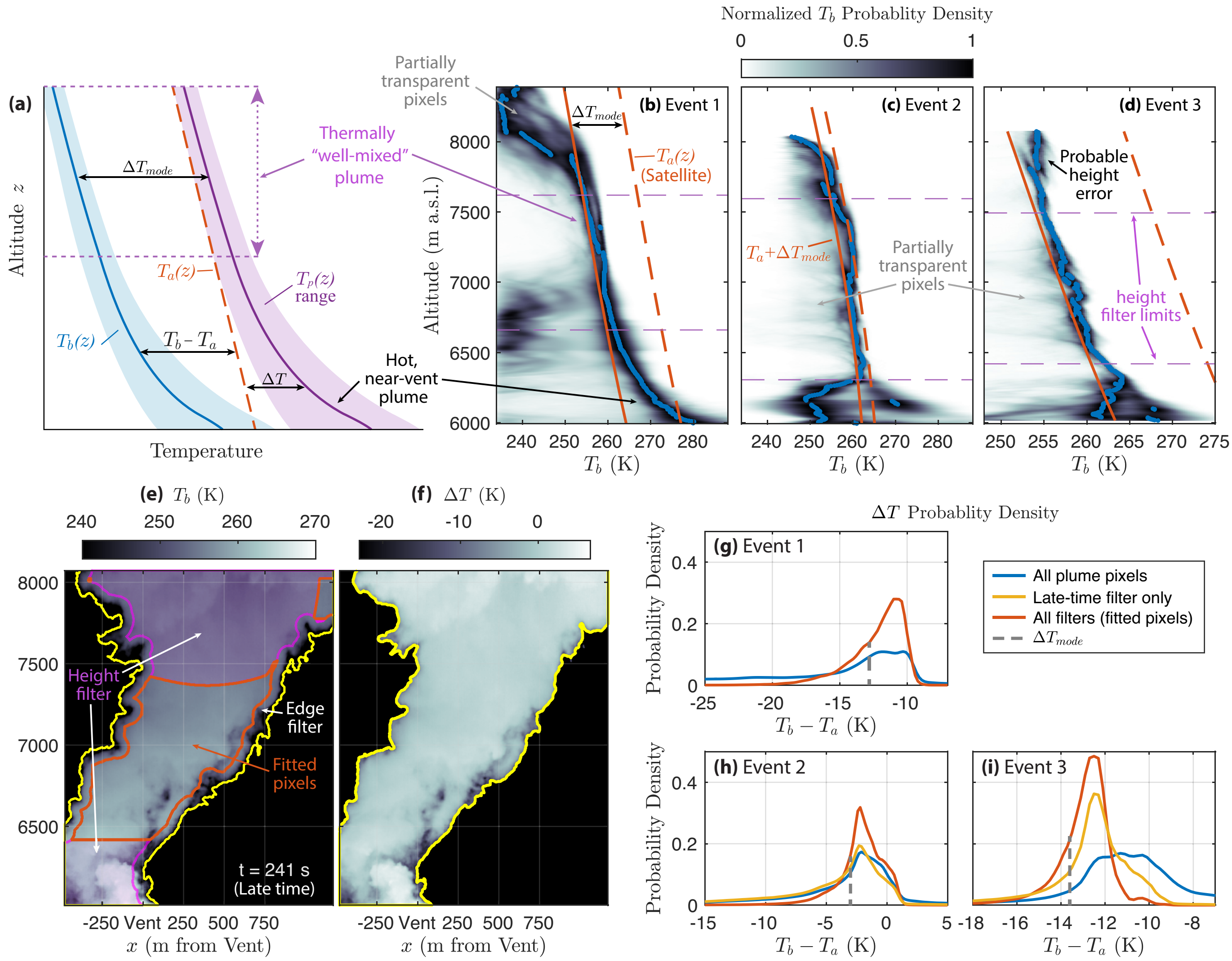

Figure 4. Atmospheric profile removal. (a) Schematic evolution with height for absolute column temperatures $T_p(z)$ (purple line gives the mean, shaded field gives the approximate range) relative to the atmospheric stratification (dashed orange line) for a steady plume. An equivalent brightness temperature trend $T_b(z)$ as recorded by a thermal camera is shown in blue. (b)-(d) Probability density function (PDF) profiles of $T_b(z)$ for Events 1-3, respectively, where each PDF is derived from column pixels at a fixed height for all image frames. (c),(d) shows late-time filtered pixels for Events 2 and 3. Interpolated satellite atmospheric profiles are shown in orange before (dashed line) and after (solid line) addition of ΔT_{mode}. The blue points show the mode of T_b at each altitude. (e) Example T_b for a single frame at $t = 240$ s after the onset of Event 3, highlighting portions of the frame that are filtered to obtain an estimate of ΔT_{mode}. (f) ΔT as obtained from Equation 6, for the same frame as in (e). (g) PDF's of $T_b - T_a$ for Event 1: all column pixels (blue), and fitted pixels with all filters applied (orange). Vertical dashed grey line give the estimate of ΔT_{mode} based on the filtered peak half-maximum. (h) As in (g) for Event 2. The yellow line gives the PDF for all column pixels after $t = 164$ s (a "late-time" filter only). (i) As in (g) for Event 3. The yellow line gives the PDF for all column pixels after $t = 200$ s.

say less than 100 to 200 K, because the effects on radiative heat transfer of broadband emissivity and transmissivity scale as $T_b^{1/4}$. This approximation is therefore not valid for magmatic temperatures in general, but is reasonable in our case since the highest temperatures we record are about 400 K (the upper limit of the thermal camera gain setting we employed). For example, assuming that the satellite atmospheric profile gives the true temperature (about 267 to 275 K between 6500 and 7500 m a.s.l.), then for the largest estimated magnitude of $\Delta T_{mode} = -12.4$ K (Event 3, Figure 4d), Equation 5 implies a combined emission and transmission loss $(\varepsilon\xi) \approx 0.83$. In this case, the maximum error introduced to our ΔT approximation for the hottest (unsaturated) pixels is about 7 K, and typically less than about 2 K. In Supplementary Information Section 3.4 we further demonstrate that this approximation has a negligible impact on our quantitative results for power law temperature decay.

To calculate ΔT for each event, we perform careful data filtering steps to obtain the subset of column pixels within the "well-mixed" region, and use these data as a reference to fit the atmospheric profile and obtain the correction ΔT_{mode}. In particular, we apply data filters to remove pixels that are:

1. near to the visible edge of the ash column and which are likely to be highly oblique and partially transparent. A distance of 20 pixels, or about 10 to 25% of the column radius in the fitting region, is sufficient in practice.
2. still at elevated temperature above background following emission from the vent. We manually choose a height for each event below which pixels are removed, and this is shown by the bottom dashed purple line in Figure 4(b)-(d).
3. have large uncertainty in height above the vent. Height uncertainty is calculated automatically for each event, as described in Supplementary Information Section 3.1. The approximate cutoff height, which may vary in x, t, is shown by the top dashed purple line in panels (b)-(d).
4. at early time when column temperatures are highest, for the transient Events 2 and 3 only, since those pixels are most dissimilar to the background atmosphere. We choose frames greater than 164 s and 200 s after the start of Events 2 and 3, respectively (c.f. Figure 3). This step minimizes ΔT values and maximizes the height window obtained from steps 2 and 3 above.

Figure 4e shows typical results of the pixel filtering for a single example frame of Event 3. The manual filter of near-vent pixels and the automatic filter of pixels with large height uncertainty are shaded in purple, and the filter to remove transparent pixels is shown near the column edge. The remaining pixels outlined in red in the column middle region are those that can reliably be used to match the atmospheric profile trend dT_a/dz. Subtracting $T_a(z)$ from these data therefore removes the stratification trend and produces a population of pixels for which ΔT is close to 0. The difference $T_b - T_a$ is plotted as probability density functions for each event in Figure 4, panels (g)-(i) for different subsets of pixels. Pixels with all filters applied PDFs show a single peak at -10.8 K, -2.2 K, and -12.4 K for Events 1, 2, and 3, respectively. From the description above and as shown in panel (a), we expect the filtered pixels will retain some positive ΔT, i.e. elevated above temperatures corresponding to T_a. For simplicity, we choose the more negative half-maxima of the filtered peaks (i.e. the value of $T_b - T_a$ at which the PDF peak reaches half of its maximum probability) as the estimate of ΔT_{mode} for each event. These values correspond to -12.8 K, -3.0 K, and -13.6 K, for Events 1, 2, and 3, respectively, and are shown with dashed grey lines in panels (g)-(i). In Supplementary Information Section 3.3, we give further rationale for this choice of ΔT_{mode} by showing that column temperatures at any given height tend statistically towards local minima that coincide approximately with this choice of the peak half-maxima. The ΔT_{mode} correction provides a readily-identified and adjustable threshold ΔT value below which pixels are likely to be partially transparent, capturing background atmospheric emission and therefore not representative of the plume thermal mixing process. This choice also facilitates the power-law fitting process outlined in Section 3.7.

3.3 Column Source Time-series Retrieval

To investigate time-evolving column source behavior as shown in Figure 3, we choose an image window that is as close as possible to the vent but excludes all edifice pixels, and has a height approximately equivalent to the dimension of the largest entraining eddies which we will track. Typically for a single vent source this corresponds to the radius of the column. For Event 3, which has a complex source consisting of multiple vents and consequently eddy structures that are often much smaller than the apparent column radius, we use a correspondingly smaller window height as shown in Figure 3c. The left and right limits of the source window are dictated by the boundaries of the column mask for a given frame, and thus vary with time. Once the exact window position as a function of time is defined, we retrieve statistical information of the temperature and velocity fields within the window for all frames. These outputs include the mean, median, minimum, maximum, variance, and the 25-75 and 5-95 percentile ranges as shown in Figure 3d-f. This procedure captures variations in source temperature and velocity on time scales most relevant for resolving entrainment processes and, furthermore, sets the preferred initial dimensions of a moving window used for structure tracking, since the coherent column structures of interest are approximately of this length scale. The resulting temperature time-series at the source $\Delta T_{src}(t)$ is used, in turn, to detect the initiation and duration of the largest pulses of hot material from the vent.

A goal of this analysis is to estimate the thermal evolution of bulk (or interior) column temperature with time and height, which varies with fluctuations in source mass and buoyancy fluxes. Since the camera records temperatures at the outer edges of eddies, the hottest temperatures visible in an apparent structure at any time are representative of material emerging from the hot interior of the ash column as a result of the overturning motions of eddies at various scales during turbulent mixing. Consequently, variations in peak temperature are proxies for relative variations in mass or buoyancy flux (Patrick et al., 2007; Gaudin et al., 2017). As shown in Figure 3d-f, the maximum values of ΔT (shown in green lines) are overprinted with relatively low amplitude, high frequency variability (periods of less than about 2 to 5 seconds) that arise from fluctuations in the velocity field related to turbulence and accelerations over scales much smaller than the largest eddies. By contrast, we find that the smoothed time series given by the 75th and 95th percentiles are more effective for capturing variability related to the largest vent source pulses, jets and plume/thermal motions. Consequently in the analyses below, we will make use of these percentiles of ΔT to constrain the hottest column interior temperature variations related explicitly to entrainment and thermal mixing by the largest turbulent motions as erupted material rises. For automating pulse detection, we employ a simple short-term-average/long-term-average (STA/LTA) detection method similar to that used in seismic event detection (Sharma et al., 2010), using the time series of temperature variance in the source window. Since the number of events and structures we track is relatively small, in many cases we manually refine the choice of the first frame of the detected pulse for which to initiate the structure tracking algorithm. Automation of the detection step is, in principal, relatively straightforward and any number of detection algorithms could be employed for larger data sets.

3.4 Time-averaged Images

Studies of volcanic column dynamics routinely use long-time-averaged measurements of flow properties as an effective means of "removing" the effect of turbulent fluctuations and enabling direct comparison to predictions from steady plume theory, and this approach has also been applied to ground-based thermal imagery of volcanic columns (e.g. Patrick et al., 2007; Cerminara et al., 2015). Time-averaging is, in principle, a useful technique that is easily applied to field observations and experimental data. However, time-averaging is not a straightforward exercise for unsteady eruptive regimes where variations about notional mean properties are non-stationary, can exceed the mean itself, and where the column vertical temperature profile at any one time is the integrated result of a continuously evolving source condition. How best to choose the time intervals over which to carry out time-averaging such that essential thermal mixing properties of the three basic flow regimes in Figure 3 are readily identified and distinguished is, for example, unclear.

To explore the extent to which time-averaging of thermal data captures the essential characteristics of plume/thermal flow regimes with varying unsteady character, we produce time-averaged images of the three studied events for comparison with the results of our time-dependent tracking algorithm, which we discuss next. Specifically, we will compare reconstructed thermal evolutions with height produced by both methods. We construct time-averaged images for each event by first selecting an appropriate averaging interval. For the approximately steady Event 1, the mean-flow is easily defined and we use the full 5-minute span of data shown in Figure 3d. For Event 2, we select the period following the starting pulse that is dominated by highly pulsatory flow (i.e. large fluctuations about the mean, 47 to 150 seconds in Figure 3e) as an intermediate flow regime between the approximately steady flow of Event 1 and the strongly transient flow of Event 3. For Event 3, which is characterized by both pulsatory and rapidly decaying vent source conditions, we average over the first 54 seconds, which excludes the early development of the starting pulse that was not captured with full resolution video, but includes the rest of the starting pulse rise and the subsequent 4-5 large pulses (Figure 3f, see also Results section). After filtering out pixels with large height uncertainty and background temperature values according to Section 3.2, we take a time-average of both the temperature and velocity fields for all pixels that lie within column masks, averaging all quantities over the full duration of the time windows described above. We further discuss the resulting time-averaged images and their quantitative analysis in Section 4.2.

3.5 Structure Tracking of Turbulent Structures

The primary output of the structure tracking algorithm is the "segmentation" (labeling) of pixel groups belonging to individual, coherent, turbulent structures rising from the vent. Once structures have been identified and tracked, their temperature and velocity statistics with height and time are retrieved for further analysis. The result is a measure of the structure evolution from the point in time at which it was emitted from the vent. Even assuming highly accurate optical flow velocity retrieval, 2D velocity fields derived from optical flow analysis cannot be used alone for structure tracking because transient turbulent accelerations and instabilities related to mechanical effects of both entrainment and thermal mixing involve significant flow components normal to the imaging plane and rotational motions that have strong downwards components (see below). To track the motions of the dominant overturning structures that govern entrainment, we therefore use a combined spectral clustering and optimization technique to identify and isolate, on a frame-by-frame basis, groupings of pixels with similar velocity and temperature characteristics that move as coherent structures. Here we give an overview of the guiding principles in the tracking algorithm development and briefly describe the essential steps of the algorithm workflow, which are outlined in Figure 5. We describe the internal function of the algorithm in greater detail in Appendix B.

Spectral clustering is an "unsupervised" machine learning technique for classifying unlabeled data, and is similar to other clustering approaches in that it finds groupings with 'similar' properties. The choice of a metric for 'similarity' is a key element of all clustering algorithms. Here, we use spectral clustering to identify coherent structures in thermal imagery by the similarity of pixels, without relying on the absolute accuracy of pixel temperatures or velocities. Clustering alone, however, does not robustly capture coherent eddies in their entirety because the complex internal motions and temperature fields in such structures are inherently heterogeneous. In particular, maximum temperatures and vertical velocities occur at the upper leading edge of eddies and result from flow emerging from within the eddy interior, whereas rotating motions arising from eddy overturn and air entrainment give strong horizontal and downward velocities, as well as colder temperatures along eddy margins and trailing edges. As a result, large variances in both velocity magnitude and direction, and bi-modal temperature distributions are basic features of these large eddies as a whole, and clustering alone tends to divide eddies between the relatively hot, rising leading edges and the relatively cold and downturning trailing regions (see for example, Figure 5b,c). We navigate this image analysis challenge by introducing an optimization step in our clustering algorithm that adds physical constraints related to the heat transfer properties of eddy structures of interest. Finally, because the column flow is continuous and differences between frames are small, using the "memory" of cluster location, temperature, and velocity field from preceding frames during the optimization step enables the tracking algorithm to capture the evolution of the entire structure. Accordingly, the "tracked structure" for any given time step, or image frame, is the combination of both the selected (optimized) cluster and pixel locations of the tracked structure from previous time steps.

The heat transfer properties of turbulent structures depend on their location, size, excess temperature and rise speed. Accordingly, we cluster our image data using the 5-variable space $(i, j, \Delta T, u, v)$, where each variable is normalized to its standard deviation. We establish similarity with a 'Similarity Graph' that defines relationships among data points in a local neighbourhood, and which consists of a set of nodes (data points in our 5-variable space) and edges (weighted connections among similar data points) (von Luxburg, 2007; Saxena et al., 2017). We use the Matlab implementation of spectral clustering, which includes the following components: (1) The initial similarity graph is constructed using a *k-nearest-neighbours* (Cover & Hart, 1967) approach to assign edges, and assigns the edge weights of each connection, or similarity, according to the Euclidean distance between data points. (2) A normalized, random-walk graph Laplacian matrix is constructed from the initial similarity graph (Shi & Malik, 2000), which serves to reduce data dimensionality and enhance the contrast between data clusters (von Luxburg, 2007; Saxena et al., 2017). (3) Finally, a clustering step using the k-Means method (MacQueen, 1967; Saxena et al., 2017) is performed, using the eigenvectors of the Laplacian matrix as input variables. A major advantage of spectral clustering over other clustering methods is that no strong assumptions are made on the form of data clusters (von Luxburg, 2007). As a consequence, for the complex and frequently non-convex shapes of structures in our data space, we found that for capturing the shape of column structures in their entirety, spectral clustering generally outperformed other clustering methods that were tested during development (see Appendix B for further details on algorithm development). However, the Matlab implementation of spectral clustering is computationally expensive to perform for data sets of greater than about 10,000 points, and we consequently employ a frame-by-frame approach for the clustering step rather than incorporating time information.

Spectral clustering forms the core of our tracking algorithm. However, the novel aspects of its implementation arise from careful selection of the data input and cluster output using physics-based constraints. Specifically, the goal is to track the largest, hottest, and fastest moving turbulent structures in the visible column. Physically, such structures will carry most of the heat (and driving buoyancy) flux and deliver a vertical heat flow E:

$$E = \pi L^2 \rho v c_p \Delta T. \tag{7}$$

Here ρ is the bulk density of the erupting gas-particle mixture, c_p is its bulk specific heat capacity (approximately that of the pyroclasts), and L is the characteristic radius or length scale of the largest turbulent eddies. We take the characteristic scale length for L to be 1/2 the diameter of a plume or thermal, consistent with expectations from the entrain-

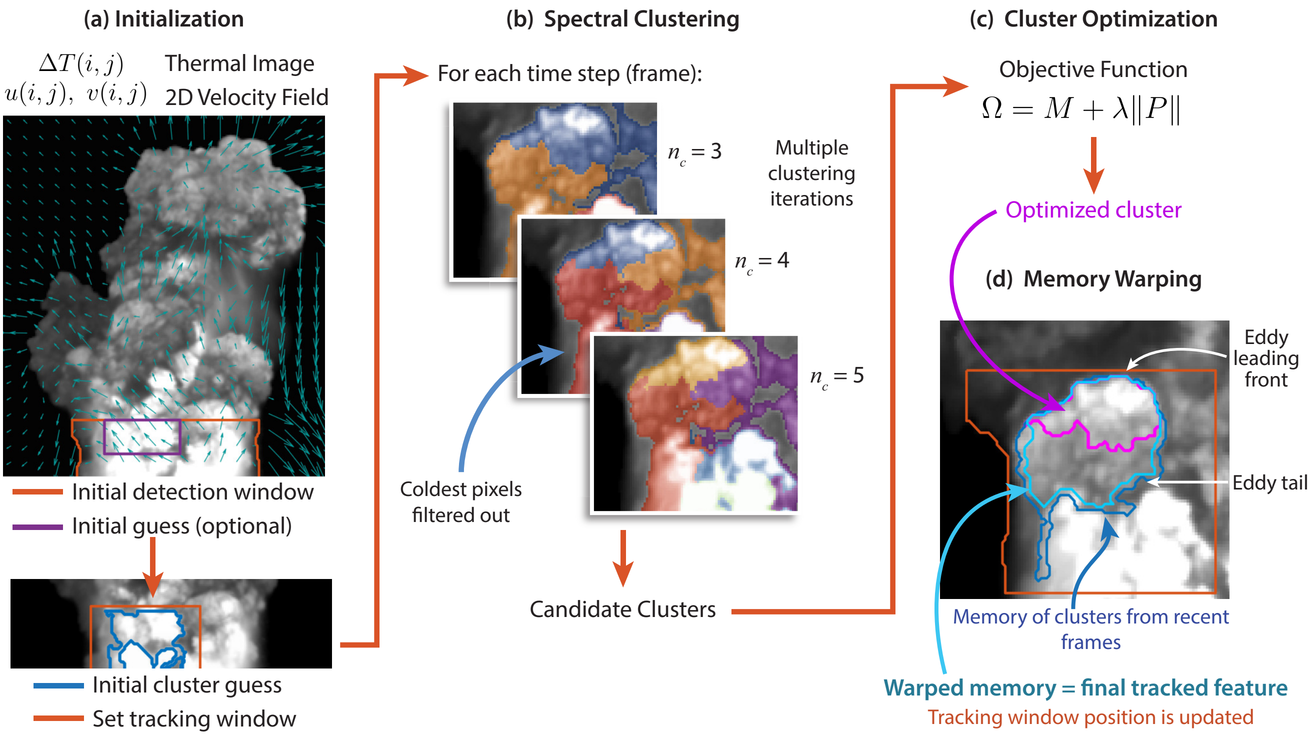

Figure 5. Structure tracking algorithm overview (see text for detailed description). (a) Tracking initialization includes identifying a starting frame and initial detection window, and performing an initial clustering step to identify the structure of interest. (b) For each subsequent frame, the coldest pixels (the 30th percentile by default) are first filtered out, then the algorithm performs spectral clustering of remaining pixels within the tracking window using different choices for the number of clusters n_c. (c) An optimization of candidate clusters identifies which output cluster maximizes the apparent energy flux (equation 7) and also matches the structure memory from previous frames. (d) In the final step, the structure memory from previous frames (dark blue line) is "warped" towards the optimized cluster (magenta line) by comparing their relative positions and allowing the memory boundaries to move within a physically realistic maximum velocity (as determined statistically from the data set velocity fields). The resulting "warped memory" (light blue line) is taken as the tracked structure.

ment assumption (Turner, 1986). The thermal evolution of such rising structures with atmospheric entrainment and mixing governs the overall evolution of eruption columns: the excess temperature ΔT, velocity field $\vec{u}$, and 2D area of structures $A \sim L^2$ as visible in the thermal imagery are consequently the most important variables for clustering and tracking.

For each tracked structure, the tracking algorithm proceeds in 4 main steps and produces a single "track", or record of the structure position in time and space. The steps are summarized here and described in greater detail in Appendix B. Step 1, initialization, is performed once for the first frame of each track, while steps 2-4 occur for all subsequent frames. Steps 2-4 proceed until a stopping criteria is reached.

1. **Initialization (Figure 5a)**. Select a detection window (generally a visible region of the column immediately above the volcanic vent - i.e. the "source win-

dow" shown in Figure 3), and perform an initial clustering step to identify a structure of interest at track time $t_k = 0$. Estimate the optimum number of clusters n_{c0}, and initialize a tracking window: a moving sub-region of the frame derived from the detection window, centered on the tracked structure and which defines the subset of data to use in clustering steps.

2. **Spectral clustering (Figure 5b)**. First filter cold pixels or non-column pixels from the tracking window; pixels below the 30th percentile of values within the tracking window are initially filtered by default, but this value is adjusted automatically as the target structure cools, to ensure that pixels in the target structure are not removed. Perform clustering of the remaining data as described above, repeating over a range of values of n_c (typically $n_{c0} - 1$ to $n_{c0} + 1$).
3. **Optimization (Figure 5c)**. Among all identified candidate clusters, choose the cluster that both maximizes the apparent vertical energy flux and best matches the characteristics of the tracked structure in previous time steps (referred to hereafter as the "tracking memory"). This step is accomplished using the objective function
$$\Omega = M + \lambda||P||, \tag{8}$$
where M is a "data" term that optimizes for maximum heat flow, P is the "prior" term which evaluates similarity with the tracked cluster from previous time steps, and λ is a scalar regularization parameter which tunes the relative importance of the two terms. The algorithm tracks the cluster that minimizes the cost function Ω. We describe each of the terms of Ω and its implementation in detail in Appendix B.
4. **Memory Warping (Figure 5d)**. Define the "tracked structure" for this time step as pixels that match both the selected cluster and tracking memory (i.e. the structure as identified in previous time steps) to within a position tolerance defined by the Optical Flow velocities. This step effectively prevents the boundaries of the structure from evolving at a nonphysical rate. Physically and practically, the clustering and optimization steps identify the hot "leading front" of the target structure, while the memory warping step retains information on the colder trailing edge. The combined components of clustering/optimization and memory warping therefore comprise the entire turbulent structure of interest. Finally, update or "warp" the tracking memory locations using Optical Flow velocity fields, and similarly move and resize the tracking window as needed to continue following the tracked structure.

To stop tracking a particular structure, it is appropriate to employ multiple stopping conditions including the when the structure tracks outside of the frame, or when data thresholds such as a maximum height uncertainty or minimum excess temperature are exceeded. Here we employ all of these, and also in some cases manually truncate individual tracks as necessary, for example when the tracked structure becomes obviously occluded or engulfed by another part of the column. The clustering and optimization steps make use of scalar weights (for clustering variables and the prior term P, respectively, see Appendix B for details). The choice of these weights, the regularization parameter λ, and selection of data for curve fitting (see Section 3.7 below) require careful user oversight and are reasons our workflow remains user-intensive.

3.6 Eddy Temperature and Size Retrieval

Once a complete track has been obtained, the next step is to retrieve its size and temperature evolution as a function of height. Figure 6 shows an example single track from Event 1 to outline the process of obtaining $R(z)$ and $\Delta T(z)$. To obtain $R(z)$, for each frame we take the pixel area of the tracked object and calculate the radius of an equivalent area circle, converting this value to a length in meters using the pixel dimensions. The corresponding height for each radius measurement is taken as the centroid of the tracked object. To obtain $\Delta T(z)$, we take a statistical distribution (i.e. the mean and 5th, 25th, 75th, and 95th percentiles, as for the source window in Section 3.3) of all tracked pixels for all frames at a fixed height. Practically, taking temperature distributions for a tracked structure along a fixed height is computationally similar to creating the time-averaged thermal images. Both operations sample the 3D array of ΔT along the (x, t) dimensions, but only labeled pixels are sampled in the case of the tracked structure, whereas all column pixels are sampled when creating time-averaged images. This sampling method allows a direct comparison of height evolution for a tracked structure, which is associated with the onset of a single pulse at the vent source, with estimates obtained from time-averaged images, which contain information for all source times within the averaging window. In Figure 6 and subsequent figures below and in the Supplementary Information, plots of the time evolution of ΔT show the data distributions in terms of mean (dark line), percentiles (5-95 and 25-75 in light and dark gray shaded areas, respectively). We highlight the 95th percentile in blue since we use these values for the subsequent curve fitting and power law exponent retrievals.

3.7 Virtual Source Estimation and Power Law Fitting

The structure tracking algorithm retrieves information on the evolution of large turbulent structures with high time resolution comparable to eddy overturn times, and a central challenge is to understand the extent to which evolving behavior is influenced by source unsteadiness or is consistent with turbulent fluctuations inherent to statistically steady turbulent plumes. Here we outline a first order method to distinguish unsteadiness contributions, in which we obtain estimates of the power law exponent B governing the evolution of ΔT with height both in individually tracked structures and in time-averaged images. We first note that in tracking turbulent structures and applying spreading rate and temperature decay fits as described above, we implicitly make the hypothesis that the individual structures behave in a manner that is self-similar and reflects the bulk flow properties, at least in an ensemble averaged sense. The extent to which virtual source locations and power-law fits agree between tracked structures and time-averaged images may variously indicate (a) whether the above hypothesis is correct and the flow is broadly self-similar in its evolution, or (b) whether the effects of source unsteadiness are significant and preclude accurate characterization of the flow using time-averaging approaches. We return to these assumptions in interpreting our results in Section 5.

The steps to obtain power law fits are broadly: (1) apply a linear regression fit to the measured radius to obtain both spreading rate estimates and location of the virtual source z_0, and (2) apply a power law fit of the form

$$\Delta T_{95} = c_1 (z - z_0)^B + c_2. \tag{9}$$

As described in Section 1, plumes and thermals are predicted to evolve as a power law with distance downstream from a non-physical virtual source and assuming the effects of stratification are relatively small. Kaye and Scase (2011) show that for conditions in which the straight-sided solutions to the plume rise equations exist (i.e. radius growth is linear with height), the power law relation in Equation 3 is valid for purely buoyancy driven flows. In practice, this assumption generally requires that the altitude range over which we apply power law fits is less than both the scale height of atmospheric stratification and the maximum rise height of a plume or thermal (Caulfield & Woods, 1998; Bhamidipati & Woods, 2017). As we show below, the process of virtual source estimation below explicitly relies on column conditions for which rise is effectively straight-sided and the power law relations are reasonable approximations. We further discuss these assumptions as a potential source of error in Section 5.1. Finally, we note that in applying Equations 1 and 9, we make the common pseudo-gas assumption in which fine ash particles (typically less than mm scale) are carried by the flow and contribute to the effective bulk density of the column (e.g. Jaupart & Tait, 1990; Woods, 1995). Simple calculations show that we may safely assume changes to bulk density and temperature are

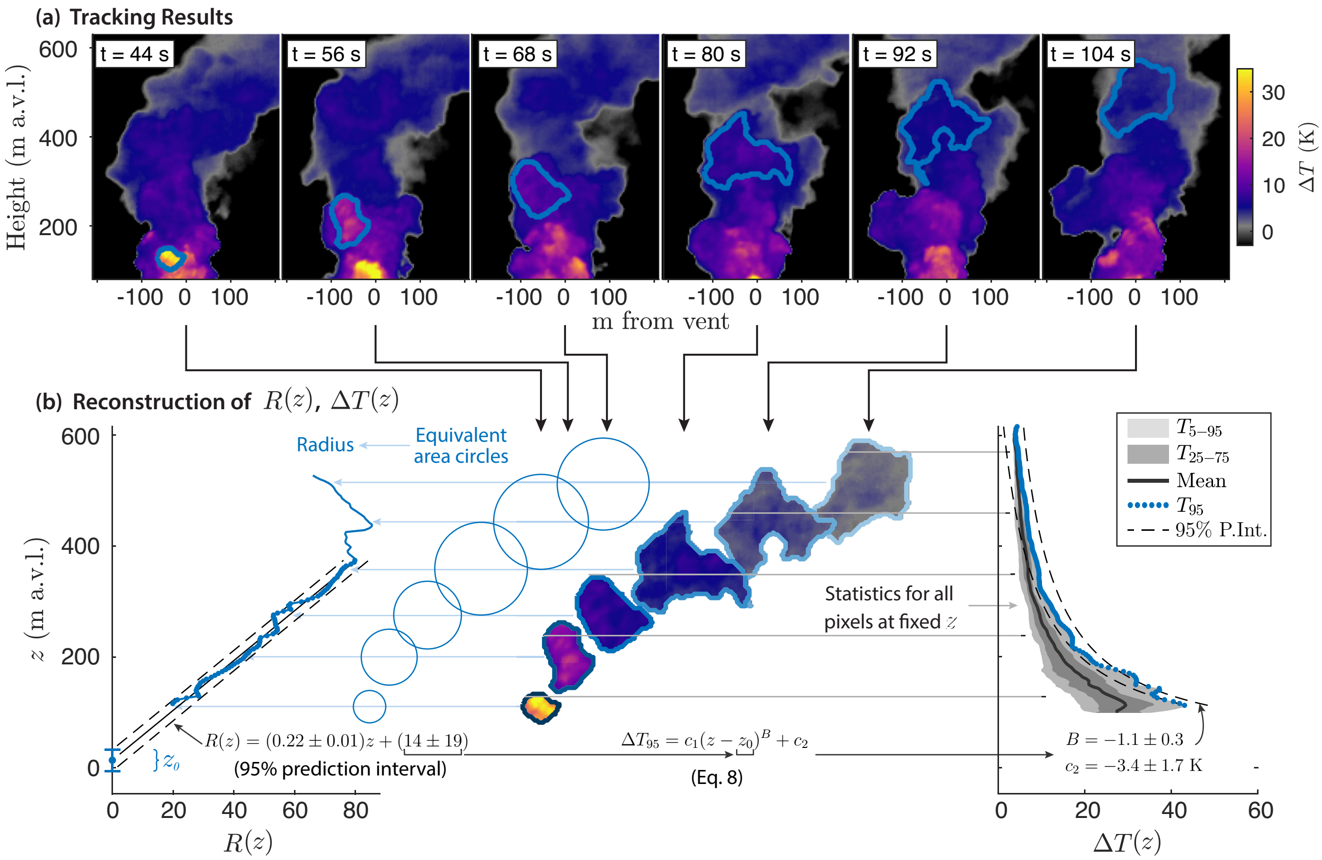

Figure 6. Example tracking results for a single track of Event 1. (a) 6 example frames outlining the tracked structure. (b) Overview of radius and temperature reconstruction for the track as a function of height. The radius is determined for each frame by calculating the radius of a circle of equivalent area to the track outline, and a corresponding height is taken from the outline centroid. The subset of data plotted as points are those used to find the virtual source using a linear regression. The excess temperature is reconstructed by taking the statistical distribution (mean and percentiles) for all pixels at a fixed height (i.e. a given height contains information for all frames that contain track pixels at that height).

dominated by entrainment and gravitational potential energy release, so long as the loss of particles due to sedimentation is not much more than order 10% of the total mass load of fine particles over the first few hundred meters of column rise. This assumption is consistent with the observed minor ash fall and inferred excess gas content at Sabancaya and with expectations from simple integral models (e.g. Girault et al., 2014).

Estimation of the virtual source location is critical to accurate estimation of the power law exponent B. A variety of methods are available to estimate the virtual source location in experimental and theoretical plume studies (Hunt & Kaye, 2001; Ciriello & Hunt, 2020), however the majority of these rely on *a priori* knowledge of the source buoyancy, mass, or momentum fluxes. These quantities are not easily characterized in field settings because of the particularly large uncertainties in column axial velocities and particle volume fractions (Patrick et al., 2007; Aubry et al., 2021). Consequently, we use the simplest approach, which is to extrapolate a linear fit to the column radius, taking the virtual source as the location at which the radius $R(z) = 0$ (e.g. Figure 1). The measure of the column radius itself, however, may be defined in multiple ways. For instance, the well-posed unsteady integral model of Woodhouse et al. (2016) uses Gaussian widths to define boundaries, whereas the unsteady model of Craske and van Reeuwijk (2016) uses top-hat widths defined from integral fluxes. In the case of our observed columns in the field, we can measure column radius as the Gaussian half-width of horizontal velocity or temperature profiles, or as the half-width of the visible column boundaries. All of these measure should yield a similar virtual source location, given two assumptions: (1) the column radial profiles of velocity and temperature evolve in a manner that is approximately self-similar with height, and (2) the velocity and temperature profiles are of similar characteristic length scale (Kaminski et al., 2005; van Reeuwijk et al., 2016; Ciriello & Hunt, 2020). The first assumption is necessary for the theoretical power-law solutions which we seek to be valid (Morton et al., 1956). We take the second assumption since we do not have information on the internal profiles of the column, and can only approximate Gaussian profiles using imagery of the outer regions of the column that we observe.

For all heights in the time-averaged images, we take the visible column radius as the half-width of the column masks, and we fit Gaussian curves to the image horizontal temperature and vertical velocity profiles. Though these Gaussian profiles are matched to the column exterior rather than the true interior profiles, they in general yield radius values that are quite close to the expected value of about 50-60% of the visible radius derived from the width of the column masks (Turner, 1962; Patrick, 2007). We now have in total three different estimates of $R(z)$, though the uncertainty in these measures is difficult to quantify and likely varies considerably within and across different events. For example, the mask width measure obtained from column boundary tracking (Bombrun et al., 2018) may be influenced by complex shapes arising from local wind shear, transient eddies, or other cloud structures separated from the main vertical flow. Such effects frequently result in radius estimates that are not consistently linearly increasing with height (see for example the time-averaged results for Events 2 and 3 in Section 4.2). Similarly, the quality of the Gaussian profile fits depends on the extent to which visible of elements at the column exterior correspond (on average) to internal flow profiles, and on the accuracy of the Optical Flow algorithm in determining the velocity field (see for example the complex, multi-vent source region of Event 3). These complexities are the reason we seek multiple radius measures, and since we have no *a priori* reason to have higher confidence in any one measure, we average the three radius estimates to obtain a result for $R(z)$ that reduces the impact of outliers in any one measure. For comparison, we also report results obtained from each of the different radius measures (see Section 4.2). For the individually tracked column structures, as described above we find that both the simplest and most successful radius measure is simply to take the radius of the circle with area equal to the outlined area of the tracked structure (the exceptions are the starting pulses of Events 1 and 2, for which the mask-width approach described above is also applicable).

To obtain z_0 for both tracked structures and time-averaged images, we apply a linear regression fit to the radius measures described above. For each case, however, it is necessary to choose manually the subset of R and ΔT data for which to apply linear and power law fits, respectively. Here we describe the rationale and results for manual selection of track data, and for additional details we refer to the manuscript Supplementary Information. In particular, Supplementary Videos 1-3 show detailed tracking results of our three events, and data selection and fitting for all tracks are shown in Supplementary Information Figures S8-S14. As highlighted by blue points plotted over the radius data of Figure 6b, the tracking results of column structures typically include sections in which the eddy structure displays a clear linear trend in growth, as is expected for self-similar flow and entrainment in both plumes and thermals. These subsets of data showing linear growth are used to perform linear regression to determine the virtual source location.

The radius trend in the example of Figure 6b clearly deviates from linear growth above about 375 m. This break from a measure of linear growth is common across all tracks and occurs for a variety of reasons, most of which are associated with the complex 3-dimensional turbulent flow and include: occlusion, engulfment, or coalescence with other column eddies, large uncertainty in the height position, strong distortion by wind (typically above 500 to 1000 m above the vent in our field data, see Figures 3 and 9), or poor accuracy of the tracking algorithm (e.g. excluding part of the eddy structure or deviating to another one). Curves for ΔT also contain sections of poor data quality or high noise, most frequently due to saturation of pixels at high temperatures and due to local turbulent fluctuations of thermally heterogeneous eddies in the column. Occlusion, engulfment, or poor tracking quality also in many cases affect ΔT curves, though the effect is less significant than for $R(z)$ since retrieval of the temperature data does not require accurately capturing the shape of the target structure. As a result of these complications, it is necessary to manually select segments R and ΔT data of a given track for the purposes of our curve fitting. It is worth emphasizing that deviations from linear trends in R are most commonly associated with tracking performance or features of turbulence, rather than any obvious change in column dynamical behavior. Consequently deviations from linearity in the radius measures do not provide unambiguous information on the validity of the straight-sided plume equations, and temperature curves are furthermore reliable over larger height ranges in general. To ensure quality power law fits in B, we therefore use separate manually chosen height limits for fitting R and ΔT (see Table S2 for fit height limits for each track, and Figures S8 - S14 for fit results.)

Fortunately, it is generally straight-forward to identify results of good quality tracking in video of the tracked structures, minimizing user subjectivity in the selection of high-quality data for curve fitting. Linear trends in the growth of radii measurements consistently correlate with periods where the tracking algorithm obviously follows the visible boundary of a well-defined turbulent eddy structure, and it is generally easy to identify in the video imagery when the target structure is occluded, engulfed, or strongly wind-distorted, or when the algorithm fails to adequately track its visible shape. For both R and ΔT curves, we also automatically exclude data points for which more than 90% of pixels at that height exceed the height uncertainty thresholds described in Section 3.2. Additionally in the case of temperature curves, we automatically exclude points for which more than 10% of pixels are saturated to ensure that the statistical distributions of pixel temperatures are not to severely biased. In the case of all three events, there is a height above which wind effects begin to dominate the flow behavior, which is readily apparent from examining the time-averaged images shown in Figure 9. This occurs at about 600, 400, and 600 m above vent level for Events 1, 2, and 3, respectively. Above these heights, radius measures are generally unreliable and largely excluded (in fact the individually tracked structures frequently distort or break up at these heights to the point that the tracked outlines are no longer usable, as can be seen in Figures S8-S14 and in Supplementary Videos 1-3). Temperature values in most cases remain of good quality over larger height ranges than radius measures. For temperature curves, the manual selection process is more straight forward and usually only requires identifying the height at which decay resembling power law behavior clearly begins, which often occurs somewhat above the initial track detection either due to saturation of the hottest pixels near the vent, or because power law behavior is established only after the first one or two eddy overturns.

Once manual data selection is finalized, we proceed with the final curve fitting procedure to obtain z_0 and B. From the linear regression fit for $R(z)$, we set z_0 as the point at which $R(z) = 0$. The confidence interval is determined as the values of z for which the upper and lower 95% prediction intervals for $R(z)$ are each equal to zero. To obtain B, we then apply the power law fit using the MATLAB Curve Fitting Toolbox. Uncertainty in z_0 has the largest control on the resulting B estimate, so we perform the power law fit for each of the upper, central, and lower estimates of z_0. The result is three separate estimates for B, each with their own confidence intervals. We take our best estimate for B as the central value derived from the best estimate z_0, and the confidence interval for B is defined by the minimum and maximum of the 95% confidence intervals across all three power law fits.

4 Results

4.1 Overview of Three Events and Structure Tracking Results

In this section, we summarize the results of both structure tracking and source window analysis for each of the three eruptive events. We then discuss in detail the results of curve-fitting and power law retrieval for the time-averaged thermal images. Finally, we summarize the results of virtual source estimation and power law exponent retrieval for the set of 26 individually tracked structures across the three events to examine their time-evolving character. The time-averaged image results facilitate a comparison of the steady or time-independent picture of plume dynamics against the results for time-evolving tracked structures. In particular, if the power law exponent is indicative of entrainment behavior as either thermal-like or steady plume-like, then comparison of B exponents between the time-averaged images and the time-evolving results of tracked structures will shed light on the importance of time-dependence in the evolving column sources. In doing so, our goal is to highlight the extent to which one or the other entrainment regime dominates the behavior, and/or the extent to which time averaging produces results that are representative of the governing dynamics. In this section we highlight the quantitative results from structure tracking and time-averaging, and revisit their comparison and interpretation in the discussion section.

Figure 7 shows a summary of the essential characteristics of Event 1, including its source emission time-series ΔT_{src} and the timing and height of tracked turbulent structures. The same data for Events 2 and 3 are shown in Figure 8. In general, the algorithm successfully outlines relatively hot column structures that are expected to dominate the energy flux. The tracked structures tend towards rounded or circular on average, but frequently take on complex and rapidly evolving shapes. Panel (b) shows the position of the top or leading front of each tracked structure overlaid on a “rise diagram” (the maximum row-wise ΔT for each frame as a function of time and height above the vent, following Gaudin et al. (2017); Tournigand, Taddeucci, et al. (2017); Smith et al. (2021)). For a detailed view of the tracking algorithm performance, see Supplementary Videos 1, 2, and 3, which correspond to each of the studied events. By Equation 7, the source time-series data in panel (c) are useful as a proxy for the power E delivered from the vent. Viewed this way, the effect of fluctuations in heat and velocity (source signals for the mo-

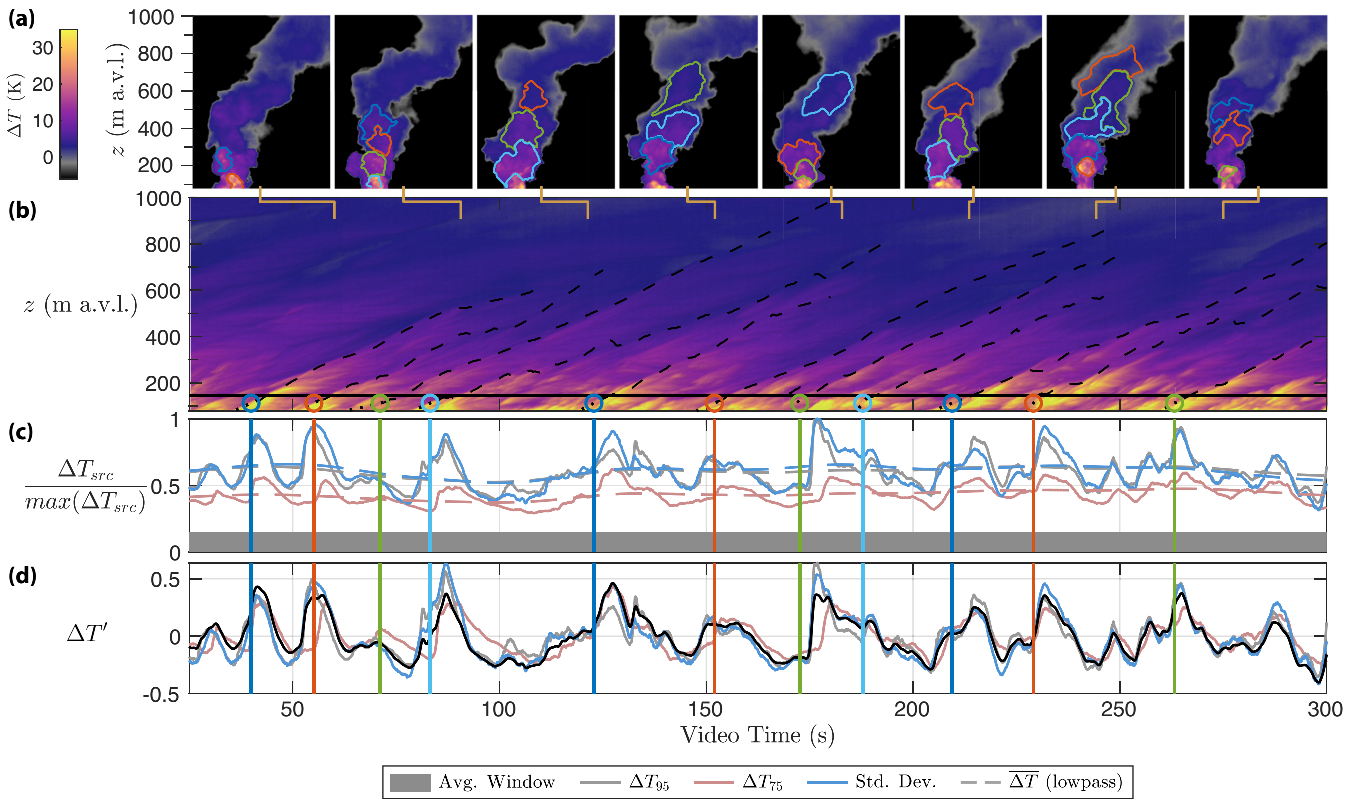

Figure 7. Summary of tracking results and source history for Event 1. (a) Sample thermal images with overlaid outlines of tracked structures. Lines at the bottom of each frame highlight the corresponding frame time in panel (b). (b) "Rise diagram" for Event 1, which shows the maximum column ΔT along a horizontal profile at each height and time. Black dashed lines show the top height of tracked structures. Colored circles show the time at which the tracked structure is centered in the source window (dotted black lines are also plotted that connect the first tracked frame to the time of the structure's first appearance, to highlight cases where the source window and initial tracking window do not coincide, which occurs for some tracks in Events 2 and 3), and the source window limits are shown with a black horizontal line. (c) Normalized temperature profiles in the source window, showing 95th (grey) and 75th (red) percentiles, and standard deviation (blue). The dashed lines show low-pass filtered curves to approximate the mean excess temperature trend $\overline{\Delta T}_{src}$. Vertical colored lines correspond to tracked structure start times in panel (b), and match the color of outlined structures in panel (a) frames. The gray shaded bar at the bottom of the panel shows the time span of averaging for generating the corresponding time-averaged image for this event. (d) The same curves as in (c), with the mean (low-pass filtered) curves removed to give the relative magnitude of fluctuation about the mean $\Delta T'_{src}$. The black curve shows the average of the three normalized curves.

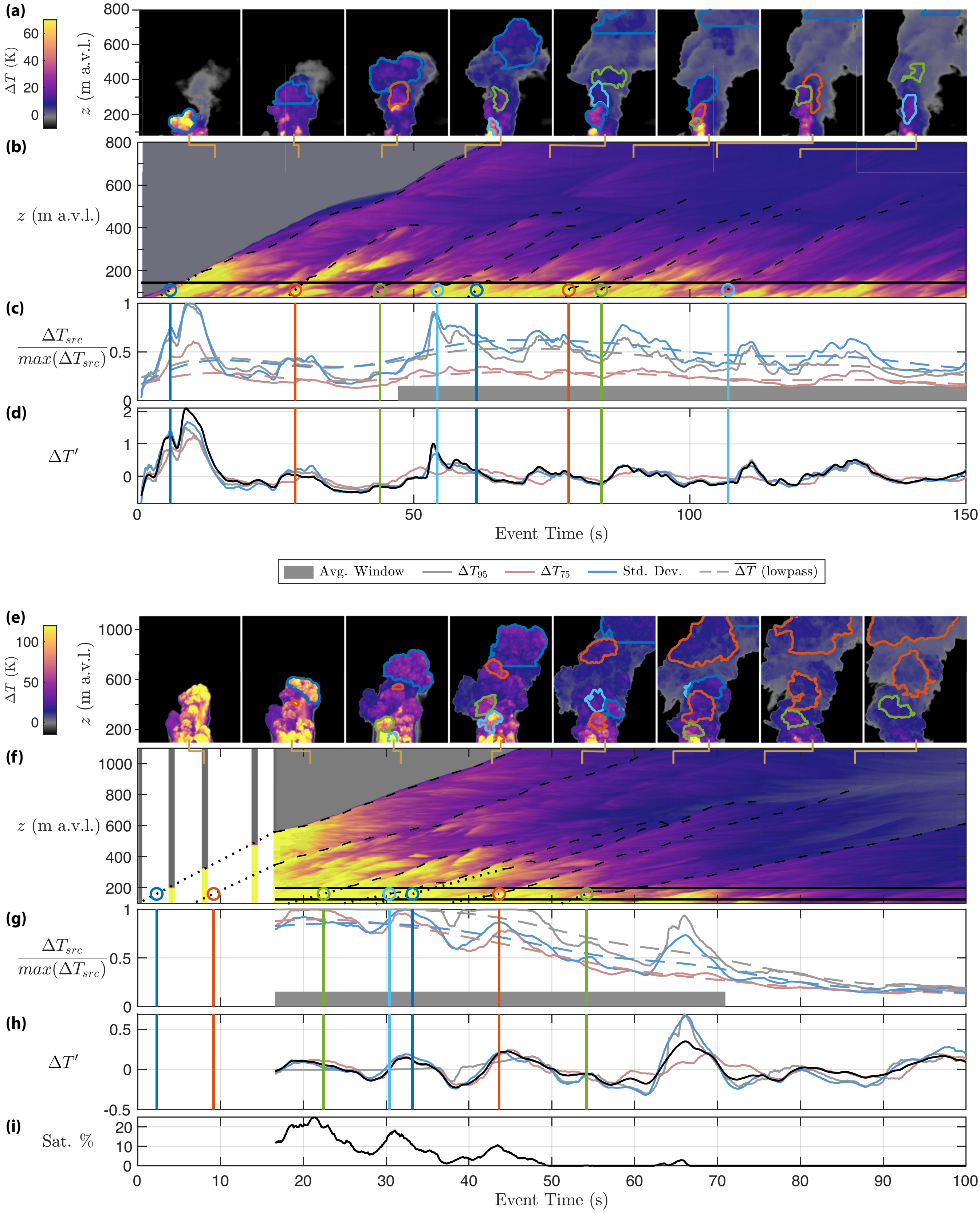

Figure 8. Summary of tracking results and source history for Events 2 and 3. (a-d) As for Figure 7 for Event 2. (e-h) As for Figure 7 for Event 3. The data gap at early time for Event 3 represents a time frame in which the thermal camera was capturing only time lapse frames about every 4 seconds. (i) Percentage of saturated pixels in the Event 3 source window as a function of time.

mentum and buoyancy fluxes) delivered at the vent source can be observed in the rise history of individual turbulent structures. To characterize and understand relationships between fluctuations in the source signals and the thermal evolution of tracked structures with entrainment during their rise, it is instructive to consider the magnitude of temperature fluctuations about an effective mean. To this end, we apply a zero phase, low pass filter to each source time series, using a cutoff period equal to 2 times the average overturn time of the largest eddies, or about 75, 55, and 40 s for Events 1, 2, and 3, respectively. The resulting proxy for a "mean" heat flux carried by tracked structures $\overline{\Delta T}_{src}$ is shown for each time series with a dashed line.

Finally, in panel (d) we introduce a semi-quantitative measure for the relative magnitude of thermal fluctuations about this mean:

$$\Delta T'_{src} = \frac{\Delta T_{src} - \overline{\Delta T}_{src}}{\overline{\Delta T}_{src}}. \tag{10}$$

To produce a representative $\Delta T'_{src}$ that captures the relative timing and magnitude of fluctuations at the column source, we average together the three normalized $\Delta T'_{src}$ measures, shown by the black line. This averaging scheme is an attempt to account for our limited, exterior view of the column by preserving the long period oscillations, which are assumed to be associated with bulk plume diameter-scale changes and emerge best in the standard deviation measure, while emphasizing the importance of the high temperature percentile modes which are most representative of the column interior. For the largest pulses of Event 1 that give rise to our tracked structures, a typical amplitude from peak to trough over the averaging window for $\Delta T'_{src}$ is 0.3 to 0.7.

For Events 2 and 3 in Figure 8, the tracking results and source time series show significantly more variation in time, beginning with the onset of an initial large pulse. For Event 3, the initial onset was captured only with time-lapse imagery at approximately 4 second intervals, as shown with in vertical bars in the first seconds of panel (f). The first two tracks (we will often refer to tracked structures as simply "tracks" from here on) for this event therefore begin with the first full-resolution video frames at about 16.5 seconds after the event onset, and the timing of emergence for the first two tracks are inferred to within about 2 seconds as shown with the black dotted lines. The data for Event 3 also suffer from significant pixel saturation at early times as the eruptive temperatures were much hotter for this Event than the previous two, as shown by the percentage of saturated pixels in the source window in panel (i). As a consequence, the amplitudes of the three earliest peaks captured are notably suppressed in panel (h), and we can only infer the amplitude of $\Delta T'_{src}$ for the starting pulse, which we will address further in the discussion section. From the change in pixel saturation alone, however, it is easy to conclude that the amplitude of this temperature peak is greater than the starting pulse of Event 2, which never saturates more than about 1 to 2% of pixels.

As initially described in Section 2.2, for Events 2 and 3 in Figure 8, the starting pulse structure is significantly larger and of higher temperature and velocity than subsequent pulses. They evolve within the first 400 to 600 meters above the vent into large vortex rings through strong overturning motions and a correspondingly rapid areal expansion. Pulsatory emissions follow the initial starting pulses. For Event 2 (Figure 8a-e), the radius and rise velocity of the initial front are about 2 and 1.5 times higher than the average for following pulses, respectively, and we estimate a fluctuation amplitude $\Delta T'_{src}$ of the starting peak of 2.4. Tracked structures for Event 2 following the starting pulse have generally consistent rise velocities of about 7 to 10 m/s. In the period following the initial onset, the ΔT_{src} time series shows a period of sustained, pulsatory behavior over about 120 to 150 seconds, though with a mean value that is more variable than for Event 1 (Figure 8c). $\Delta T'_{src}$ amplitudes range between about 0.3 to 1, somewhat higher and with greater variation than for Event 1 (Figure 8d). For Event 3 (Figure 8e-i), the mean source temperature ΔT_{src} decays rapidly to near zero within about 80 to 90 seconds of the event onset (panel (g)), and the rate of this decay is likely underrepresented due to pixel saturation. The effects of the decaying source are also apparent in the velocity of tracked structures. Though individually they rise with approximately constant velocity, each subsequent pulse in Event 3 is slower than the previous, decreasing from initial velocities of 16 to 18 m/s down to about 7 m/s for the last tracked structure. Finally, we note that for Event 2, the time-averaging window is from about 45 to 150 seconds, focusing on the character of the pulsatory emissions following the starting pulse, whereas for Event 3 the time-averaging is done from the start of the video at 16 s after onset to about 72 s, and therefore captures in whole or in part the evolution of the dominant pulses. In the following subsection, we highlight the essential features of the time averaged images, including the results of virtual source estimation and power law curve fits for $\Delta T(z)$.

4.2 Power Law analysis: Thermal Evolution of Time-Averaged Images

Figure 9 shows the time averaged thermal images and velocity fields for all three events in the left-most column, together with curve fits for column radius and excess temperature decay (second and third columns, respectively). The final column on the right shows the results of virtual source location and power law exponent estimation. We will first describe the essential features of the images and radius and temperature profiles for all three events, and will then discuss the curve fit results. The excess temperature fields show a spatially-varying and monotonic cooling with eruption height. The comparatively unsteady Events 2 and 3 show vertical evolutions in the temperature, velocity fields, and radius that are more complex than in the case of the relatively steady Event 1. This is a result of both shorter averaging times and more complex flow fields in these events. In particular, Events 2 and 3 have, on average, larger fluctuation magnitudes arising from individual pulses which produce additional noise in time-averaging. In addition, the Event 1 time-averaged image is averaged over 308 s, approximately 3 and 6 times the averaging length of Events 2 and 3, respectively, which yields vertical trends that are more smooth as apparent in the trend of ΔT_{95} for this event. The source region of the Event 3 averaged thermal image is also characterized by 3 spatially distinct temperature peaks immediately above the vent, representative of the multiple source jets that contributed to the ash column. The effects of wind are apparent in the time-averaged velocity field vectors overlaid in blue on the averaged thermal images, becoming increasingly significant typically above about 400 to 600 meters above vent level (a.v.l.). Above this region in all three events (with the exception of the Event 2 and 3 starting pulses), the combination of wind-driven and buoyancy-driven turbulent mixing cause most individually tracked structures to become thermally indistinguishable from the bulk column, and most tracks are stopped by around 600 m a.v.l. For Event 1, wind causes bending of the column immediately above the vent, an effect which increases in magnitude above about 500 m. This effect is also apparent in the estimates of radius with altitude, which are approximately linear below this height.

In the case of the steady Event 1, the long time-span of averaging and relatively smaller fluctuation magnitudes in the decay curve are reflected in the narrow width of the confidence interval for the power law fit (Figure 9a, third column). Though less well constrained than for Event 1, the curve fits are of good quality for Events 2 and 3. In the right most column for each time-averaged image are the estimated values of z_0 (top) and B (bottom). Recalling from Section 3.7 that we apply multiple measures of radius to obtain the most robust z_0 estimates possible, here we show each of the measures for column radius in the second column, and the corresponding z_0 estimates for each in the right-most column. The virtual source for Events 1 and 2 are relatively more shallow and each lie at about 200 m below the vent, reflecting the similar size of these two columns (each about 200 meters across immediately above the vent). In contrast, for Event 3, the multi-jet source of which is about 300 meters across, the estimated virtual source is about 600 m below vent level. The radii measured in the time-averaged image are largely defined by the combined (i.e. averaged) width of multiple, complex sources that feed a sin-

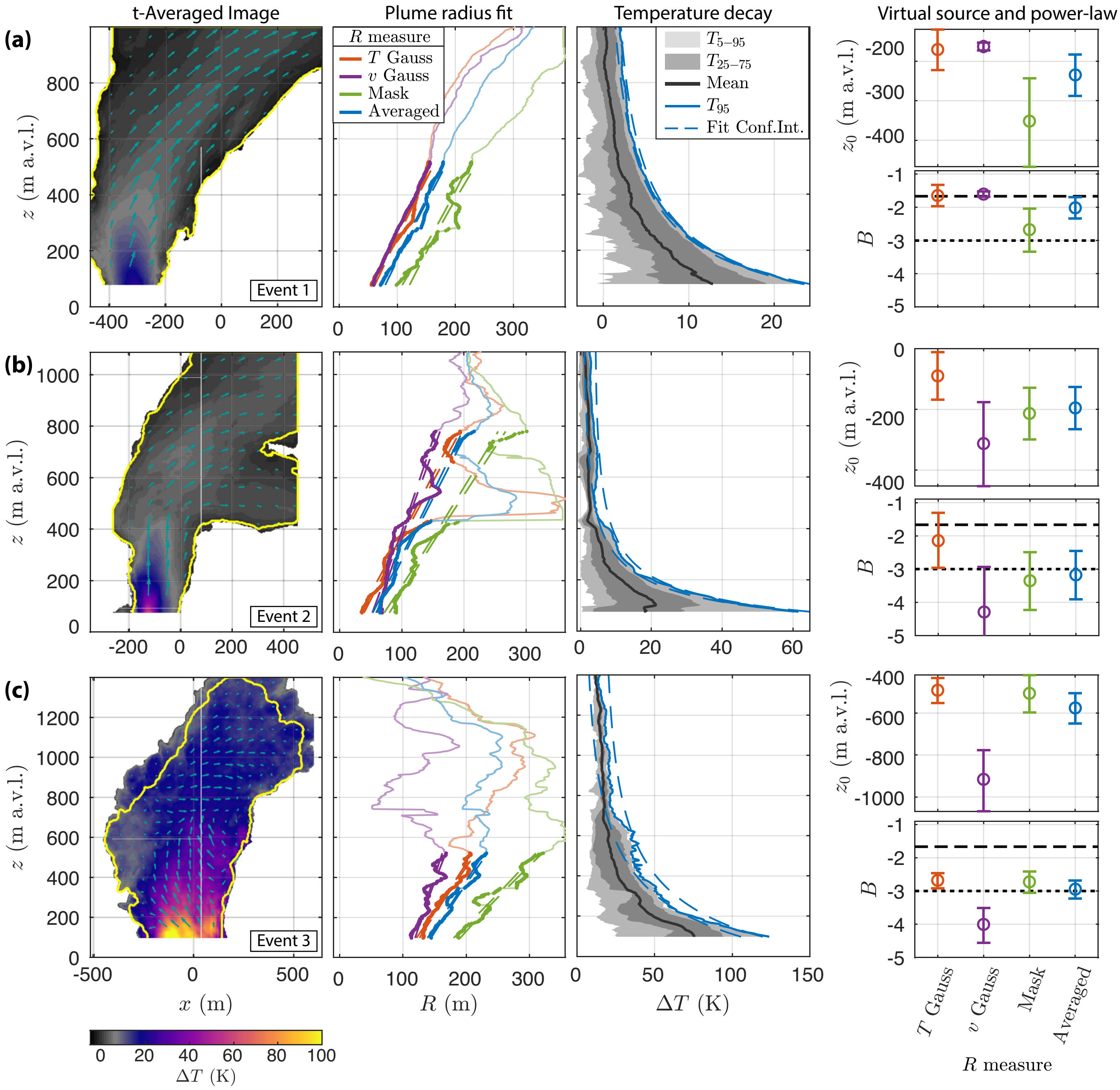

Figure 9. Time-averaged image results for (a) Event 1, (b) Event 2, and (c) Event 3. For each event from left to right, the first column shows time-averaged ΔT (colors) and $\vec{u}$ (vectors overlain in light blue), and the second shows four different measures of column radius versus height above vent z, with linear fit confidence interval as dashed lines. The plotted points (may appear as thicker lines) show the subset of data used for the linear fit. The third column shows the distribution of $\Delta T(z)$ in gray with power law fit confidence interval for ΔT_{95} in blue. Note that these represent confidence intervals for a single fit (recall that three fits are performed over the estimated range of z_0), but the intervals themselves do not vary significantly for differing values of z_0 and resulting B estimates. Finally, the right-most column shows estimates of the time-averaged virtual source position z_0 and power law exponent B, using the four measures of column radius. The values of z_0 correspond to the 95% prediction interval for each of the linear fits to radius in the second column. In each of the plots for B, the theoretical values for power law exponents are given by the dashed line for plumes ($B = -5/3$) and dotted line for thermals ($B = -3$).

gle dominant ring vortex. As we will show below, this feature of the method has significant consequences for the prediction of the time-averaged z_0 relative to z_0 for the individual pulses of material which make up this event.

The best estimate B exponents resulting from the average radius measure (blue colors in middle column of Figure 9) for each of the three time-averaged events lie on or very close to either the thermal or plume predictions from theory. In particular, the value we obtain for Event 1 is -2.0±0.3, comparable to the expected steady plume value of -1.67. The unsteady Events 2 and 3 give time-averaged B exponents that overlie values predicted for pure thermals: -3.2±0.7 and -2.9±0.3, respectively. The results for time-averaged images therefore appear broadly in line with predictions of Morton et al. (1956) for the steady plume of Event 1 and the highly transient Event 3. For Event 2, we chose the time averaging window to capture the period of pulsatory flow after the starting pulse to test for plume-like entrainment dynamics (Turner, 1962). We note, in addition, that across all of the different methods for measuring column radius, the resulting estimates of B are correlated with the estimated z_0 (deeper virtual source location yields a more negative B), emphasizing the leverage that the column virtual source estimation exerts on the power law results. We address this control on our results and their interpretation in Section 5.1. As we will show in the next section, the time-evolving dynamics that give rise to the averaged behavior are more complex than is apparent here.

4.3 Power Law analysis: Thermal Evolution of Tracked Structures

We now show the virtual source and power law fit results for the 26 tracked structures, comparing them with the time-averaged results shown in the previous section. Figure 10 shows the combined results of quantitative analyses for all three studied events, for both time-averaged images and individually tracked structures. To obtain the average z_0, dR/dz, and B for tracked structures, we apply a weighted mean, in which the weights are inversely proportional to the magnitude of the root mean square error for the corresponding track curve fit (shown by the color of each data point for tracked structures). We take the standard deviation of individual results as the average uncertainty. We highlight with gray circles cases where the tracking algorithm has a known poor performance. For z_0 and dR/dz, this occurs when the shape or location of the structure is poorly tracked. In contrast, poor tracking affecting estimates of B occurs, for example, when other hot column structures are falsely identified as being part of the target structure, or when a tracked structure is engulfed or occluded by another. In these cases, the ΔT decay curves show large fluctuations and power law fits are generally poor.

The virtual source of the time-averaged image for Event 1 is somewhat deeper (-234 m) than for individual tracks (panel (b)), which average at -109 m. The spreading rate dR/dz for both the averaged image and tracked structures agree well at around 0.24, which is notably higher than values predicted for pure plumes of 0.11 to 0.15 (Turner, 1962; Patrick, 2007). For B exponents, the individual tracks of Event 1 range between about -1 and -3, and the average track result is -1.7±0.7, in a very close match to the expected plume value of -5/3, though with significant scatter. The source time series for Event 2 highlights its more unsteady and pulsatory nature relative to Event 1, characterized by a dominant initial pulse followed by a series of about 6 to 7 large pulses and subsequent decay of source temperatures and/or mass flux (see also Figure 3b,e).

For Event 2, the range of virtual source estimates are very similar to those for Event 1 for both time-averaged images and individual tracks, and the apparent spreading angles are also in excellent agreement between the time-averaged result and individual tracks. The spreading rate for the starting pulse structure is 0.25±0.02 and the average for all tracks is 0.22±0.02. Despite similar virtual source depths to Event 1, the B exponents of individual tracks differ substantially from the time-averaged result. In particular, the starting pulse track of Event 2 has a B exponent of -3.1±0.5, which is similar to the B

result for the time-averaged image, whereas all subsequent tracks except Track 5 are similar to (within error) or greater than the expected value for plumes of $B = -5/3$.

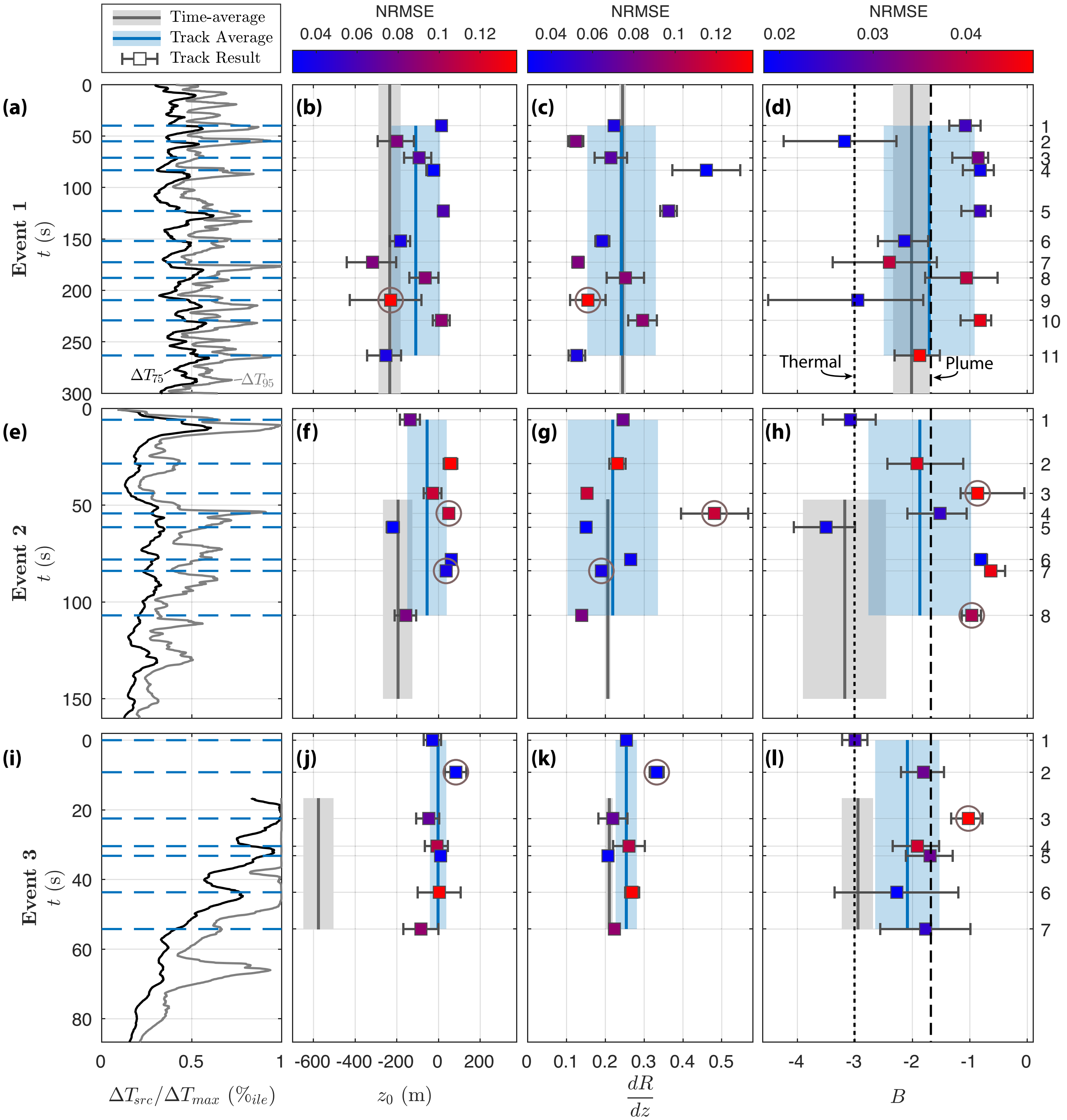
Time-average
Track Average
Track Result
NRMSE
0.04 0.06 0.08 0.1 0.12
NRMSE
0.04 0.06 0.08 0.1 0.12
NRMSE
0.02 0.03 0.04
(a)
(b)
(c)
(d)
(e)
(f)
(g)
(h)
(i)
(j)
(k)
(l)
Event 1
Event 2
Event 3
t (s)
ΔT75
ΔT95
Thermal
Plume
ΔTsrc/ΔTmax (%ile)
z0 (m)
dR/dz
B

Figure 10. Tracking and power law fit results as a function of time for (a-d) Event 1, (e-h) Event 2, and (i-l) Event 3. Note time on the vertical axis for all panels. The first column on the left shows event source time series with ΔT_{75} (black) and ΔT_{95} (grey) percentiles, normalized to the maximum value of ΔT_{95}. Blue dashed lines give the start times of individually tracked structures. The second, third, and fourth columns give, respectively, the virtual source height z_0, spreading rate dR/dz, and power law exponent B for all tracked structures and time-averaged images. Tracked structures are numbered in order on the right-hand axes. In all panels the 95% confidence bounds and averaging time span for time averaged image results are shown by the gray shaded regions, with central estimate as the dark gray line. The blue shaded regions give the average of all individually tracked structures. Results for each tracked structure are given by data points with error bars. Data points for tracked structures are coloured by the root mean square error of the curve fit (the linear model fit of $R(z)$ for the cases of z_0 and dR/dz, and the power law model fit for the case of B), normalized to the mean value. Finally, gray circles outline data points for which we manually identified poor quality of tracking and/or data fitting (see also Supplementary Figures S8-S14 for manual quality checks). Manual labels are used as a guide only, but otherwise are not applied to quantitative analysis.

Event 3 is the most transient in terms of a rapid evolution of the mean temperature field, and is dominated by a large initial explosion followed by rapid and continuous decay of source flux (Figure 10). Notably, the time-averaged virtual source of Event 3 is substantially deeper than the results derived from tracked structures (panel (j)). This result is partly related to the small sizes of individual tracked structures, which are correlated with the size of the multiple vent sources. Indeed, the virtual source locations for all tracked structures are particularly shallow, consistent, and centered directly at the vent elevation. The spreading rate for the starting pulse track of Event 3 is 0.25±0.01, and the B exponent is -3.0±0.2, which is in excellent agreement with the expected value for pure thermals as well the result for the time-averaged image of Event 3. As is the case for Event 2, the time-evolving trend for Event 3 is that of an initial dominant pulse followed by pulses with apparently more plume-like behavior, as inferred from B values. The weighted average B for all Event 3 tracks is -2.1±0.6, but with the starting pulse removed is -1.9±0.4. As is the case for Event 2, the B estimate for the starting pulse track of Event 3 matches the result of the time-averaged image, whereas the subsequent tracked structures give values more in line with expectations for steady plumes.

5 Discussion

In this section we briefly review the essential results of the virtual source estimation and power law fits for tracked structures and time-averaged images, and discuss the key sources of uncertainty in retrieving the power law behavior of the eruption columns, highlighting key steps to mitigate uncertainty. We then interpret our quantitative virtual source location and power law results in terms of the column dynamics governing unsteady behavior. In the rest of the section that follows, we outline measures for defining column source unsteadiness, and propose a quantitative definition that is most relevant to turbulent entrainment dynamics. We make preliminary comparisons of our unsteadiness measure against our observational results, and in this context we compare and interpret the results of structure tracking and time-averaging while laying out key implications and future lines of inquiry in directly linking column evolution to unsteady source behavior. We discuss implications of unsteady behavior for numerical plume models that use entrainment parameterizations, and conclude by discussing the merits, drawbacks, and future directions for our structure tracking algorithm with general applications for volcanic plume monitoring using machine-learning.

5.1 Virtual Source Estimation Dominates B Uncertainty

Our interpretation of thermal or steady plume entrainment mechanics rests on accurate B values, and we identify four possible sources of error in our power law estimation:

1. Radiative effects including gray-body column emission, atmospheric transmission loss, or background emission.
2. Enhancement of entrainment by wind.
3. Virtual source location.
4. Effects of atmospheric stratification.

For radiative effects, we described previously in Section 3.2 (see also Supplementary Information Section 3.4) that for likely ranges of combined emission and transmission loss ($\epsilon\xi$), our power law results are negligibly affected. Wind and wind shear are potentially significant drivers of altered entrainment mechanics, since wind effects can enhance turbulent motions and drive additional entrainment (Hewett et al., 1971; Bursik, 2001; Contini & Robins, 2004; Devenish et al., 2010; Degruyter & Bonadonna, 2012, 2013; Woodhouse et al., 2013; Aubry et al., 2017). Although modest winds with mean speeds comparable to or less than the column rise speed do not alter B (Aubry et al., 2017), Hewett et al. (1971) show that the column excess temperature $\Delta T \propto z^{-2}$ in the special case of very strong winds that are of order ten times the column rise speed. Since for curve fitting we specifically selected altitude ranges below heights at which the wind velocity dominates column rise, this condition is not met in our power law estimation, even for the slowest rise speeds in the steady plume. Furthermore, the expected magnitude of change to B for steady plumes of about -0.3 is for most cases similar to our measurement error and cannot explain B variations on the scale of the difference between steady plume and thermal regimes.

Rapid shape changes of turbulent structures (e.g. the structure is engulfed or occluded by another), or erroneous tracking (e.g. the structure is not accurately outlined) contribute much greater noise to radius estimates than the above considerations of wind and radiative effects, and we must choose our radius fits with care (see Sections 3.6 and 3.7, and Figures S8-S14). The magnitude of reported uncertainty in B exponents is consequently a combined result of both uncertainty in z_0 and the quality of the power law fit. Figure 11 shows our estimates of B for all tracked structures as functions of z_0 (normalized to the estimated vent radius R_0). For perfect estimation of the virtual source location, we expect that B should have no functional dependence on z_0. Indeed for a fixed vent radius, we might expect that the wider spreading angle for a thermal corresponds to a shallower virtual source location (see Figure 1), though we do not expect to see such a trend in our data from Sabancaya since the vent size and location was observed to vary between and during eruptive events. Though there is considerable scatter, an apparent linear trend in B as a function of z_0 for Events 1 and 2 is suggestive that the range in our B estimates are strongly influenced by scatter in virtual source location estimates.

To highlight the sensitivity of B to the virtual source location, Figure 11b shows B estimates for 2 example tracks from each of Event 1 and 2, using a range of assumed z_0 values. Significantly, the average B result for tracks of both events (shown with diamond symbols) lies on the expected value for steady plumes and matches the general trend in z_0. This observation suggests that virtual sources may be best represented by an ensemble average of track results, rather than by the estimates for individual tracks. The need for some degree of averaging is not surprising, since ensemble or time averaging is implicit in theoretical studies of plumes, including entrainment formulations (Morton et al., 1956; Turner, 1986). In this case, the number of tracks (or equivalently time span) to use for averaging is a critical consideration, since we must capture both the essential parameters of the flow as well as time-variations induced by source unsteadiness. For the

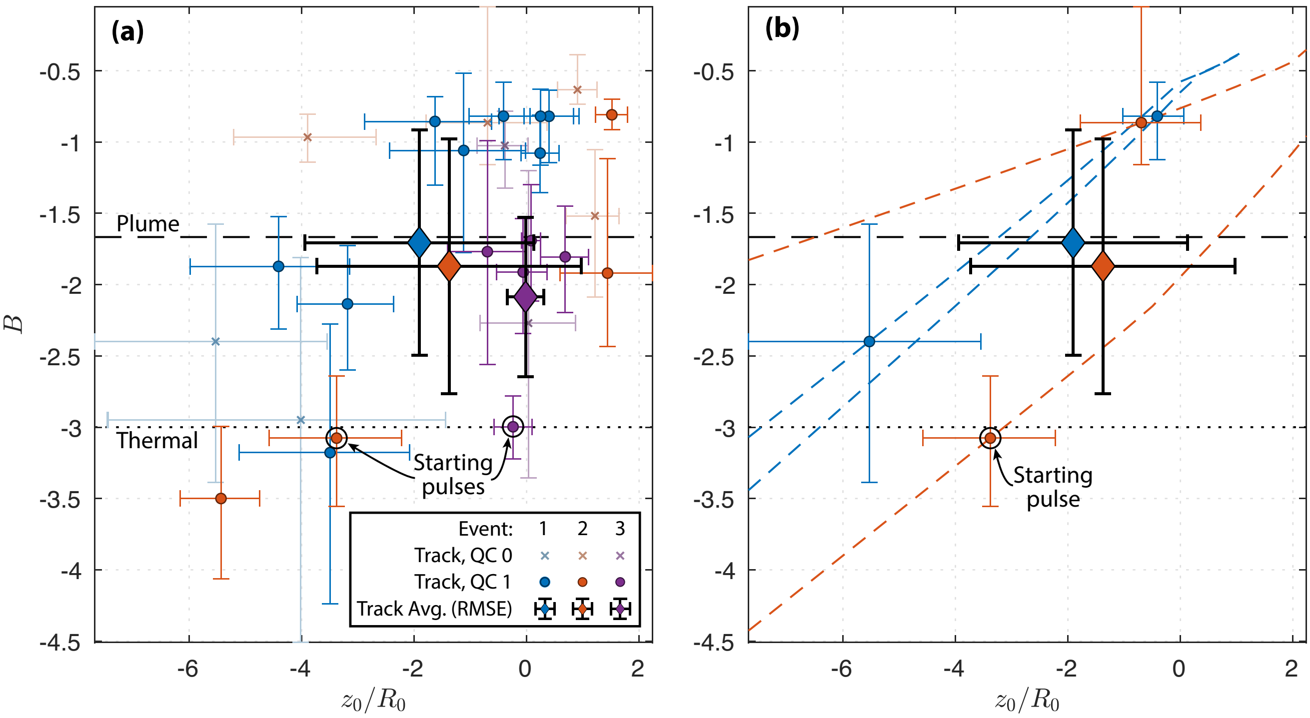

Figure 11. Normalized virtual source height z_0/R_0 versus power law exponent B. (a) B versus z_0 for all tracked structures, including the track averages (shown with diamond symbols, corresponding to blue fields in Figure 10). The track average results for both z_0 and B are weighted according to the RMS error as described in Section 4.3. Symbols are colored by both Event number and the track quality check value. A QC value of 0 (faded symbols) results from any of (1) poor $R(z)$ tracking or poor ΔT fit (see gray circled symbols in Figure 10), (2) a B result with uncertainty that spans both plume and thermal regimes. Theoretical B values for steady plumes and thermals are marked with black dashed and dotted lines, respectively, and the starting pulses of Events 2 and 3 are highlighted with black circles. (b) Sensitivity analysis of B for different choices of z_0, using four example tracks. Symbols reproduce the same results from panel (a) for each of Event 1, tracks 4 and 7, and Event 2, tracks 1 and 3, which are B values obtained while using the best estimate of z_0 for each track. The diamond symbols are the corresponding track averages for Events 1 and 2, as for panel (a). Solid lines show how the estimated B value changes for each track for varying values of z_0.

starting pulses of Events 2 and 3, however, the increase in buoyancy or momentum flux is effectively infinite, such that no track average is representative. We return to this discussion of virtual sources and appropriate use of averaging below in Section 5.2.

As outlined in Sections 1 and 3.7, in applying our power law fits we have assumed that straight-sided solutions to the equations exist for which the power laws are valid in the presence of stratification. For the power laws to be valid approximations, the height range over which we apply power law fits must be much less than both the characteristic scale height over which stratification parameter N varies (Caulfield & Woods, 1998; Kaye & Scase, 2011) and the total rise height of the column (Bhamidipati & Woods, 2017). As discussed previously, most curve fits are limited to less than about 600 m above the vent, the principle exceptions being the starting pulses of Events 2 and 3, which continue until about 1500 and 2000 m a.v.l., respectively. From the fastest local rate of change with height in dN/dz for the satellite atmospheric profiles within our analysis windows, the shortest possible scale height for any atmospheric profile is about 4 km, which is significantly greater than even the largest analysis window and we do not expect a strong influence from varying strength of stratification.

The maximum column heights are roughly 2 km for Events 1 and 2, and 3-3.5 km for Event 3 (see images of Events 1 and 3 in Figure 1), though the heights are notably influenced by wind. Therefore, our analysis windows are typically about 1/4 to 1/2 the total rise height. Over these height ranges we cannot fully rule out the influence of stratification on column rise, however again we expect that where linear fits in radius are valid, the effects of stratification are sufficiently small that the power laws provide a reasonable approximation. The sole exception in which the range of the power law fit approaches the total column height is for the starting pulse of Event 2, and as we discuss below, the interpretation of the power law fit for that track is indeed somewhat ambiguous. In Figure 11, the track average B values are consistent with expectations for plumes and thermals in unstratified media, though a possible bias is present for the cluster of tracks for which $B \sim -1$, particularly for the steady Event 1. For strong influence from stratification, we might expect a more rapid fall off in the column density deficit with height (g' in Equation 1) and therefore more negative B values. A more positive B value is in principle possible where, say, the main effect of stratification is to reduce the efficiency of atmospheric entrainment. However in following from our discussion above, we cannot separate such an effect from uncertainty in the virtual source location, and a complete analysis of the effects of stratification in this analysis must be left to future work.

5.2 Times Scales and Magnitudes of Unsteadiness

A precise definition of unsteadiness is challenging. Various treatments and definitions of unsteadiness have been employed which depend on the application of interest. In the context of monitoring or analysing the behavior of eruption columns, a critical open question remains: over which time scales and magnitudes of unsteadiness are models based on steady dynamics insufficient to capture the essential column behavior in terms of, say, column stability or height of rise, cloud spreading, or ash dispersal? The rate and magnitude of unsteady source variations for consideration ranges from those comparable to the fluctuations inherent in statistically steady turbulence (e.g., Anilkumar, 1993; Woitischek, Edmonds, & Woods, 2021) to approximately infinite for the onset of a starting plume or discrete thermal (Turner, 1962; Delichatsios, 1979; Bhamidipati & Woods, 2017), a span of regimes which to our knowledge is not covered by existing unsteady integral models (e.g. Scase, 2009; Woodhouse et al., 2016; Craske & van Reeuwijk, 2016). In this section and the section that follows, we discuss various timescales of unsteadiness as observed in our thermal imagery and their relevance for understanding column behavior, and propose one quantitative measure of unsteadiness as it relates to the behavior of our observed events at Sabancaya volcano. The chief goal is to build towards a broad and unified view of key concepts and knowledge gaps in unraveling unsteady column behavior, and thereby motivate directions for future experimental and numerical studies.

Figure 12, modified from Gilchrist (2021, Figures 5.1 and 5.3), shows schematically the key time scales governing the eruptive behaviors for Events 1-3 and potential metrics for unsteadiness involving source variability in both time and amplitude. For a schematic source time series we use the power delivered by the vent E (Equation 7) by way of demonstration, which is a measure of total thermal buoyancy flux, but similar principles apply for momentum flux in jets and both properties are readily combined for buoyant jets (Gilchrist, 2021, Chapter 5). Formally, the steady plume model of Morton et al. (1956) implies that the characteristic time scales of variation in the mean flow are longer than both

1. the characteristic turnover time of the largest turbulent eddies τ_{ot} that govern atmospheric entrainment,
2. the time $\tau_{rise} \leq 1/N$ required for the column to reach its level of neutral buoyancy, where N is the stratification Brunt-Väisälä frequency (Woods, 2010).

Consistent with assumed Gaussian radial profiles of velocity and density, source fluctuations on time scales much shorter than τ_{ot} will be indistinguishable from the natural fluctuations of the turbulent flow field and will not significantly alter the radially-averaged column dynamics or related consequences including column height oscillations. The second condition based on τ_{rise} is required to associate the properties of the spreading umbrella cloud (e.g. height, volume flux) with the instantaneous conditions at the vent (Scase, 2009).

A third flow time scale potentially important for understanding the control of the source unsteadiness on conditions in the rising column is the time τ_{mix} for thermal variations imparted at the source to travel vertically at a speed v_0 and become stirred and mixed radially or axially through progressive effects of merging, entrainment and turbulent diffusion over a "mixing length" z_{mix}. Recent unsteady integral plume models have shown that source pulses will both propagate and expand in size at a rate proportional to $t^{3/4}$ (Scase, 2009; Craske & van Reeuwijk, 2016). Therefore depending on the time scale of fluctuations at the source, pulses may be expected to interact as they expand and propagate downstream. For example, for a column with unsteady source fluctuations about an approximately stationary mean, the action of axial merging of structures combined with turbulent diffusive processes suggests the hypothesis that for time scales $\gg \tau_{mix}$ and heights $\gg z_{mix}$, unsteady fluctuations may become indistinguishable from an effective mean flow. We observe at least visually and qualitatively that several of our tracked structures merge and become thermally indistinguishable. The differing virtual source regions we obtain for tracked structures and time-averaged image of Event 3, for instance (Figure 10j), suggest that initially separate pulses from the multiple source vents merge higher in the column. However this merging is further influenced by wind-driven mixing at altitude and we cannot determine from our data alone whether the pulses remain internally distinct in terms of integral buoyancy or momentum flux fluctuations in the rising column. A scale for τ_{mix} depends on the mechanism for momentum and heat exchange, and how best to define it on the basis of our thermal data is unclear. In the special case where radial and axial mixing of a propagating axisymmetric perturbation with radius R is, for example, reliably captured through an isotropic turbulent diffusivity κ_t, an upper bound on the mixing time $\tau_{mix} \sim R^2/\kappa_t$ and $z_{mix} \sim R^2/\kappa_t v_0$. Alternatively, where the turbulent cascade underlying κ_t is incompletely-developed or where incomplete or highly anisotropic thermal mixing is a basic property of the unsteady rise of tracked structures, from the kinematics of mixing a lower bound on τ_{mix} is the time corresponding to where the rates of stretching, thinning and diffusive smoothing of temperature variations are highest (Ottino, 1989). For approximately spherical thermals of size $\sim R$ rising over a distance $\sim R$ at speed v_0, pure shear strain rates are concentrated where flow divergence occurs at the tops of tracked structures. The normal strain rate $\partial v_z/\partial z \sim v_0/R$ implies an e-fold time R/v_0 that is comparable to the eddy turnover time τ_{ot}. More generally and whatever its definition, it is unknown whether τ_{mix} must be much shorter than timescales of source fluctuations or column rise to ensure thorough mixing such that source unsteadiness does not contribute significantly to natural variations in, say, the maximum column heights. This important topic is the focus of future experiments and numerical studies and we do not discuss it further here.

Recognizing the characteristic flow time scales defined in Figure 12, we can compare three possible metrics for unsteadiness. We define the mean source power $\bar{E}$ as the magnitude averaged over a time scale that is long compared to the eddy overturn time. We note that $\bar{E}$ can be usefully cast as an enthalpy flux if thermal buoyancy and momentum fluxes are included as separate contributions. Where $\bar{E}$ varies smoothly over the duration of eruptive phase a time scale of unsteadiness is the characteristic rate of change of $\bar{E}$:

$$\tau_\mu \approx \bar{E}\left|\frac{d\bar{E}}{dt}\right|^{-1}. \tag{11}$$

To capture effects of an oscillating source flux during statistically stationary (or approximately stationary) periods within eruptive phase, we define the time scale for fluctuation about the mean τ_{pulse} to be the peak to peak pulsation interval. As τ_{pulse} becomes much smaller than τ_{ot}, subsequent pulses increasingly interact with one another and the flow becomes approximately a steady plume with corresponding entrainment rates. By contrast, as τ_{pulse} becomes much larger than τ_{ot} pulses become increasingly distinct (e.g. Woitischek, Edmonds, & Woods, 2021). Finally, from Figures 7 and 8 the magnitude of fluctuations in E' can be much larger than plausible $\bar{E}$, and in many volcanic events may span multiple orders of magnitude (e.g. Tournigand, Taddeucci, et al., 2017). It is, thus, important to consider also the magnitude of fluctuation about the mean $A^* = E'/\bar{E}$. Fluctuations in temperature and velocity that are very small compared to $\bar{E}$ will tend to be indistinguishable from turbulence at the scales of tracked structures or the column radius. Where large magnitude pulses are both widely separated in time and $E' \gg \bar{E}$, they can evolve to rise as discrete thermals (Gilchrist, 2021).

5.3 Observational Insights On Time Averaging and Column Unsteady Evolution

The characteristic time scales and unsteadiness parameters we have outlined above give us a means to evaluate the appropriateness of our time-averaging of thermal images to obtain power law fits. The definition of unsteadiness employed by (Scase, 2009) considers source evolutions that are long compared with τ_{ot} but short compared with τ_{rise}, and which propagate through the column as pulses of momentum or buoyancy. This definition implies that the column conditions at their maximum height do not represent the instantaneous source condition, and leads us to working criteria for when time-averaged images should be expected to deliver results that are representative of the governing dynamics. Rigorously, the image averaging time must be

1. $\gg \tau_{ot}$ to remove the effect of turbulent fluctuation;
2. $\gg \tau_{rise}$ as defined from the base to the top of the view field;
3. $\ll \tau_\mu$, such that averaging does not combine information from different source regimes.

If the above three criteria are met, then time-averaging is likely both appropriate and easier than tracking of individual column structures. By contrast, time-dependent tracking methods are likely required to capture the governing dynamics for events with short durations, including Vulcanian type explosions, or large magnitude source pulsations such those typical of phreatomagmatic eruptions. In the case of our time-averaged images, these conditions are easily met for Event 1, but only partially met for Events 2 and 3.

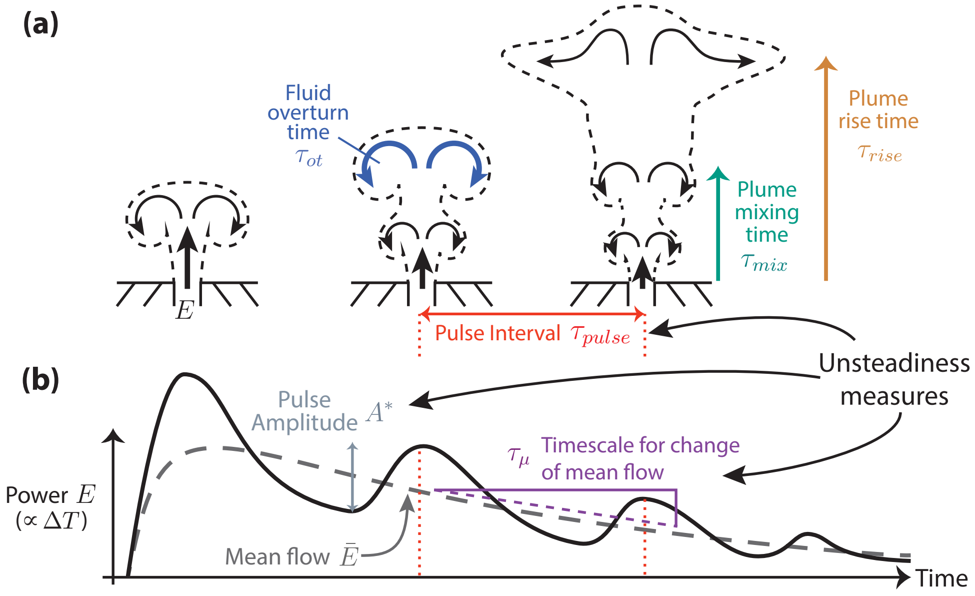

(c)

	Variable	Definition	Description
Flow Time Scales	Column rise time	$\tau_{rise} \approx \frac{1}{N}$	Time for flow to rise from vent to neutral buoyancy spreading altitude
	Fluid overturn time	$\tau_{ot} \approx \frac{2\pi R}{v_0}$	Time for flow exiting vent to complete first full overturn to initiate entrainment
	Plume mixing time	$\tau_{mix} \approx \frac{\Delta T}{v_0}\left\|\frac{\Delta T}{dz}\right\|^{-1}$	Time scale for complete radial or axial turbulent diffusive mixing
Unsteadiness Measures	Pulse amplitude	$A^* = \frac{E'}{\bar{E}}$	Amplitude of flow fluctuations normalized to mean flow
	Pulse Interval	$\tau_{pulse} = \frac{1}{f_{pulse}}$	Time interval between source pulses, inverse of a source pulsation freqeuncy
	Change of mean flow	$\tau_\mu \approx \bar{E}\left\|\frac{d\bar{E}}{dt}\right\|^{-1}$	Time scale for change in the mean, or non-fluctuating, flow

Figure 12. Characteristic flow time scales and measures of unsteadiness. (a) Illustration of column shape characteristics and flow time scales in an evolving unsteady eruption, similar to a Vulcanian explosion such as Event 3. An initial pulse exits the vent and overturns in a time τ_{ot} set by the exit velocity and vent diameter. A second pulse exits the vent and the two pulses may interact depending on the pulse interval τ_{pulse}. The time scale for pulse interaction may be approximated as τ_{mix}, and pulses propagate to the maximum column height over time τ_{rise}. (b) Schematic of the source time series for total heat energy flux at the vent, highlighting different measures of fluctuation or time variance in the source conditions. These which include the amplitude of fluctuation A^*, fluctuation time scale τ_{pulse}, and the time scale for variation of the non-fluctuating component τ_μ. All parameters may vary over the course of an the eruption, and the distinction between fluctuating and non-fluctuating components is determined by the averaging length. (c) Summary of flow time scales and unsteadiness measures as shown here and discussed in the text. Modified from Figures 5.1 and 5.3 of Gilchrist (2021).

The rise times for the 3 events within the corresponding view field of the time averaged images (about 900 to 1200 m, Figure 9) are about 160, 90, and 80 s, respectively. Using the estimated mean source time series $\overline{\Delta T}_{src}$ for these events, estimates of τ_μ for the three events are respectively about 600, 150, and 80 s. Finally, recall the averaging times are respectively 308, 103, and 54 s. From these simple estimates, the averaging time spans for Events 2 and 3 do not meet the second criterion for rise time, and are of the same order of magnitude as the mean flow evolution time. The rise diagram and source history comparisons in Figure 8 indicate that for these events variations in the source conditions are included in the time averaging, while information from the initial starting pulses still dominates the top of the view field. In short, the condition of Scase (2009) that the characteristics of the upper cloud are associated with those of the source region is not met for Events 2 and 3, and time averaging is likely not a reliable means of capturing the thermal evolution.

Comparing virtual sources, B values, and heat flow of tracks versus time-averaged images additionally highlights the dominance of the starting pulses in influencing time-averaged results and unsteady behavior. Following a similar line of reasoning to Equation 7, if we assume that the thermal energy contained in each turbulent structure is proportional to its volume, i.e. $E_{pulse} \propto \Delta T R^3$, then we estimate that the starting pulses of Events 2 and 3 carry roughly 2 to 12 and 4 to 12 times, respectively, the average heat of subsequent pulses. We note that this is a minimum estimate for the saturated pulses of Event 3 due to the uncertain magnitude of the initial temperatures. Accordingly, the column morphology recorded in the time averaged images will be largely determined by the history of the starting pulses. This dominance of the starting pulse heat flux may explain why B for the time averaged images of these events match the tracking result for each of the starting pulses rather than the average tracking result (e.g. Figure 10). It is worth noting, however, that whereas the virtual source, spreading rate, and B value all agree for the time-averaged image and starting pulse of Event 2, the time-averaged virtual source of Event 3 is substantially different than that inferred for all tracks including the starting pulse, and we return to this observation below.

For Event 2, the starting pulse virtual source is deeper ($z_0/R_0 \approx -3.4$) than the ensemble average for all tracks ($z_0/R_0 \approx -1.4$). From Figure 11b, we can infer that if the track ensemble average virtual source is adopted, the resulting exponent estimate for the starting pulse of Event 2 would be $B \approx -2.5$. Both radius and temperature fits for this track are of high quality, however, and the larger radius of the starting pulse (about double that of subsequent pulses for both Events 2 and 3) suggests that a deeper virtual source is expected, given the similar spreading rate to other tracks for Event 2 (Figure 10g). Either choice of virtual source location may therefore be appropriate for the Event 2 starting pulse. Event 2 is qualitatively similar in behavior to that of a “starting plume” with sustained emission following initial onset (Turner, 1962; Patrick, 2007), which is characterized by an initial leading vortex that is continuously fed by steady flow from below. Because of this additional supply of heat, the power law behavior for the front of starting plumes is predicted to follow a similar trend to steady plumes (Turner, 1962), assuming constant flux following the onset. For Event 2, the ΔT_{src} and rise history data (Figure 8, panels (b) and (c)) indicate that the starting pulse is followed approximately 25 seconds later by a second pulse, which eventually intercepts the starting pulse at a height of about 400 to 600 m a.v.l. From these considerations and available data, as well as the potential effects of stratification discusses above, the extent to which the turbulent evolution of the starting front of Event 2 is dominated by an initial discrete pulse or by subsequent, sustained emissions is ambiguous, and it is reasonable to interpret the starting pulse of Event 2 as either in the thermal regime or an intermediate regime approaching that of a starting plume.

In contrast for Event 3, the rapid decay of emissions following the starting pulse suggests that subsequent flow pulses are, in general, both slower and of much smaller magnitude than the starting pulse, such that the thermal-like entrainment mechanics of the starting pulse dominate its cooling. Like Event 2, the starting pulse of Event 3 has a similar spreading rate but much larger dimension relative to subsequent pulses. However, unlike Event 2, this property does not correspond to a lower virtual source location. As noted above, the large disparity between virtual source locations of tracked structures versus time-averaged image for this event is insightful, since it suggests that unlike Event 2 the time-averaged image result does not simply reflect the dominance of the starting pulse. From both our quantitative results and careful inspection of the thermal videos (see Supplementary Videos 1-3), we interpret these features of Event 3 as arising for two reasons: (1) The high virtual source of the starting pulse may be the only obvious signature of a momentum-thrust region among any of the three events, because the transition to buoyant flow, with larger corresponding spreading rates, occurs some distance above the vent; and (2) the multiple vent sources and rapid evolution apparent in the source time-series contribute to a complex source and bulk flow that is highly unsteady in both space and time and is likely not self-similar (see our hypothesis for tracking structures in Section 3.7). Caution is therefore warranted in applying models based on assumptions of self-similarity to such an event and even short time or track ensemble averages may be misleading, particularly near the source where the flow is rapidly developing. These observations are one reason why we pose the mixing time scale τ_{mix} as potentially important, since it suggests that there may be a finite height above which comparatively simple integral models for plumes or thermals can be reasonably applied.

5.4 Towards a Quantitative Metric For Unsteadiness

As we have highlighted above, various definitions of unsteadiness may arise from considering multiple differing time scales and characteristic flow parameters. Through our tracking and quantitative analysis of coherent turbulent structures, the question remains which regime of source unsteadiness governs the transition of entrainment behavior from steady plume to thermal. Since our aim is to capture entrainment mechanics of unsteady plumes from their thermal evolution, here we propose an unsteadiness parameter that incorporates essential source variations on time scales related to column entrainment and thermal mixing behavior. In particular, the starting pulses of Events 2 and 3 must be unsteady by definition, but have somewhat different time evolutions after their onset. Event 2 emissions are relatively sustained according to τ_μ, but with large fluctuation amplitudes. Event 3 also has large amplitude fluctuations, but with a more obvious decay in the mean temperature. Accordingly, we define a “Mean State Pulsation Number” Pu_μ that compares the pulsation interval and mean flow time scales, modulated by the magnitude of the enthalpy flux carried by the fluctuations:

$$Pu_\mu = \frac{\tau_{pulse}}{\tau_\mu} A^*. \tag{12}$$

In proposing this quantitative measure of unsteadiness, our choice of flow and averaging time scales depends on the problem to be solved. The resilience of the mean flow temperature and velocity fields to enthalpy fluctuations particularly in this limit depend not just on the time scale over which they are imparted, but also their magnitude, which governs the available thermal and mechanical energy. Thus, we apply $\tau_{pulse} A^*$ to form the numerator of Equation 12. For the denominator, if capturing variation in the column spreading height related to a monotonic shift in $\bar{E}$ is the goal, then τ_μ is potentially insightful, and $Pu_\mu \to 0$ implies the mean heat flow rate $\bar{E}$ is increasingly statistically steady, or that the time interval and/or magnitude of fluctuations are small. Where $\tau_{pulse} \to \tau_\mu$, there are strong interactions between the fluctuating and ‘mean’ flows. Usefully, Equation 12 as written predicts that for $Pu_\mu \to 1$, the time interval and magnitude of pulses increases such that flow behavior approaches that of discrete thermals, and for $Pu_\mu \to 0$ approaches a sustained plume. On the other hand, where variations in column spreading height are related to oscillations about a statistically stationary $\bar{E}$, $\tau_\mu \to \infty$ and has little meaning. In this case, fluctuations with periods close to the eddy overturn time

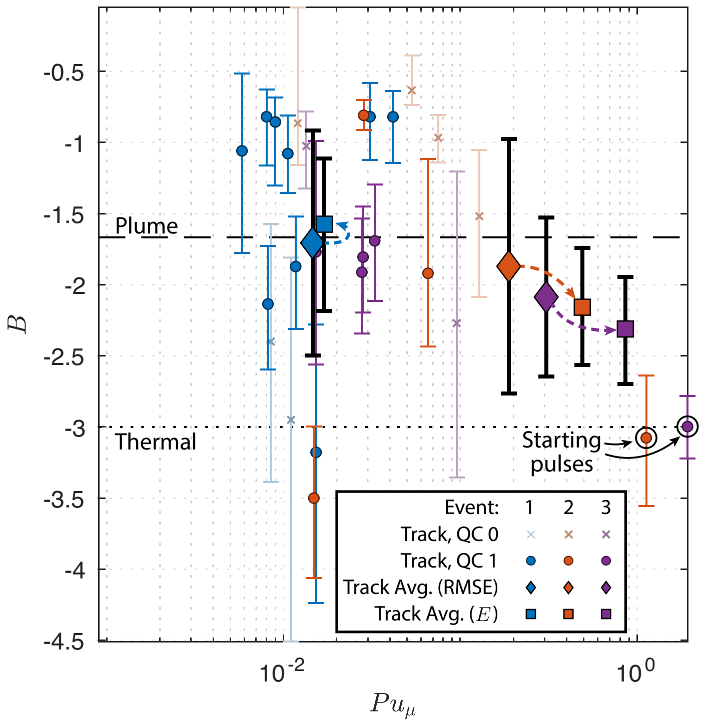

Figure 13. Power Law exponents as a function of the Mean State Pulsation Number Pu_μ. Color scheme as in Figure 11: symbols are colored by both Event number and the track quality check value. A QC value of 0 (faded symbols) results from any of (1) poor $R(z)$ tracking or poor ΔT fit (see gray circled symbols in Figure 10), or (2) a B result with uncertainty that spans both plume and thermal regimes. Diamonds show the track averages, weighted according to the fit RMS error as in Section 4.3 and Figure 11, and square symbols show the track averages when weighted by multiplying with A^* (normalized to its maximum value). Arrows highlight the shift in average result between the two average weights.

may be of greater utility than for understanding local entrainment rates and gravitational stability immediately above the vent. An alternative Pulsation Number based on source fluctuations using τ_{ot} may be chosen instead (Gilchrist, 2021),

$$Pu_0 = \frac{\tau_{pulse}}{\tau_{ot}} A^*. \tag{13}$$

This alternative definition is the subject of investigations by Gilchrist (2021, Chapter 5), and we do not discuss it further here.

In considering Pu_μ, the definition of $\bar{E}$, and consequently both τ_μ and A^*, depends critically on a choice of averaging time, which is distinct from the averaging time span used to obtain the time-averaged thermal images. As an example, suppose that the momentum or buoyancy flux as function of time for a single discrete thermal is defined by a Gaussian pulse (or in the extreme limit, a delta function). The mean magnitude of the flux function is not well defined and depends on the length of averaging time. That is, the average magnitude of a unit Gaussian pulse over ± 3 standard deviations is 0.42, and over ± 5 standard deviations is 0.25. Within this ambiguity, however, there is an opportunity to encode additional information via a flexible choice of averaging time scale. To capture critical local variations in turbulent mixing and entrainment, here we use the low pass filter cutoff period employed in Section 4.1 of $\sim 2\tau_{ot}$. Averaging instead over the column mixing time τ_{mix} may highlight fluctuations that influence, for example, the transition from momentum to buoyancy driven column rise, and averaging over the column rise time τ_{rise} captures unsteadiness that influences dynamics in the spreading cloud. For our tracked structures, we estimate A^* as the fluctuation in vertical power according to:

$$A^* = \Delta T'_{src} \frac{v_0 R_0^2}{\bar{v}_0 \bar{R}_0^2}, \tag{14}$$

where for $\Delta T'_{src}$ we take the peak value associated with each pulse, and R_0 and v_0 are the initial radius and maximum rise velocity of each tracked structure. The rise velocity $\bar{v}_0$ is the ensemble average v_0 across all tracks in a single event, and a representative value for $\bar{R}_0$ is obtained from the time averaged images.

We calculate Pu_μ for all tracked structures, using $\Delta T'_{src}$ and $\overline{\Delta T}_{src}$ as proxies for E' and $\bar{E}$ to obtain the relevant time scales. For each tracked pulse, we estimate τ_{pulse} as the average time interval to the preceding and following pulses. For the starting pulses of Events 2 and 3, which do not have a preceding pulse but are unsteady by definition, we approximate the preceding pulse interval as 2 times the rise time of ΔT_{src} to its initial peak value. Figure 13 shows our calculated B for all tracked structures, as well as the average of tracks for each event, as a function of Pu_μ. As Pu_μ approaches order 1, the weighted pulsation interval $\tau_{pulse}A^*$ approaches a similar magnitude to the time scale of change for the mean flow τ_μ, which implies that the flow is dominated by an individual pulse. For the track results shown here, τ_μ has the greatest influence on the value of Pu_μ (see Figure S15 for the value of each variable in Equation 12 for all tracks).

For our tracked structures in Figure 13, the two starting pulses of Events 2 and 3 have B values corresponding to a those of a thermal and $Pu_\mu \sim 1$, consistent with starting pulses which are unsteady by definition. Pu_μ is a potential metric for unsteadiness, however, our interpretation of the data hinges on the data points associated with the two starting pulses of Events 2 and 3. As a consequence, although Pu_μ is a promising metric, from these data alone, we cannot demonstrate with confidence that Pu_μ is the most appropriate generalized definition of source unsteadiness. Nevertheless, our result and discussion of various available unsteadiness metrics motivates further experimental and numerical studies to understand the evolution of entrainment regimes as a function of unsteadiness measures described in Figure 12.

5.5 Implications for Modeling Column Behavior

Both the analysis presented here, as well as previous observational and experimental work (e.g. Patrick, 2007; Chojnicki et al., 2015a, 2015b; Tournigand, Peña Fernandez, et al., 2017) highlight that evolutions between thermal- or plume-like states during unsteady eruptions can occur rapidly, over a number of time scales, and result in large variations in the local rate of entrainment into volcanic columns. Furthermore, rapid variations in both density and velocity on time scales comparable to the overturn time τ_{ot} may be characteristic of multi-phase flows (Anilkumar, 1993). Our estimates of the power law decay of ΔT in unsteady columns, together with the above discussion on definitions of unsteadiness support the hypothesis that volcanic columns evolve among the regimes of steady plumes, unsteady plumes, or discrete thermals, depending on the magnitude and timing of fluctuations in source momentum or buoyancy flux. Unsteadiness on times scales comparable to τ_{ot} may be of critical importance in determining the early evolution of volcanic eruption columns, impacting entrainment and local heterogeneity in velocity and particle volume fraction. These column properties influence, in turn, column gravitational stability and the formation of pyroclastic density currents, rise height, and ash dispersal (Gilchrist, 2021).

The unsteady integral plume models of Scase (2009) and Woodhouse et al. (2016) carefully consider the downstream propagation of changes in source conditions on timescales much longer than the eddy overturn time. Woodhouse et al. (2016) suggest that for pure plumes driven by buoyancy forces, the entrainment schemes of Morton et al. (1956) remain appropriate, while for momentum driven jets the evolution of self-similarity profiles is accounted for by a non-constant entrainment coefficient (Bloomfield & Kerr, 2000; Kaminski et al., 2005). Recent theoretical advances in generalizing turbulent entrainment parameterizations highlight the local and evolving nature of entrainment rates (Kaminski et al., 2005; Carazzo et al., 2008b; van Reeuwijk & Craske, 2015; Craske & van Reeuwijk, 2016; van Reeuwijk et al., 2021). A key knowledge gap for future studies is to test the functional dependence of local entrainment rates on quantified and time-dependent source unsteadiness history which spans the full range of unsteady character which occurs in volcanic events. Establishing a functional relationship between entrainment rates and Pu_{μ} or a related unsteadiness metric via laboratory experiments or direct numerical simulations (e.g. Gilchrist, 2021) would, in turn, enable more robust field-based characterization of unsteady volcanic activity, and facilitate the development and implementation of unsteady integral models which account for the order of magnitude variations in source mass flux typical of volcanic eruption columns.

5.6 On The Uses of Spectral Clustering for Automated Structure Tracking in Volcanic Columns

Our algorithm for tracking coherent turbulent structures has enabled for the first time a quantitative study of the power law behavior of temperature decay in rising volcanic columns. This application offers a path towards real-time characterization of volcanic column dynamics under rapidly evolving conditions in both space and time. The power law analysis for plumes and thermals we apply here is an initial attempt to resolve the effects of unsteadiness on rising column dynamics, but the structure tracking algorithm may be more usefully applied to compare the propagation of unsteady pulses with more complete unsteadiness theory (e.g. Craske & van Reeuwijk, 2016), estimate local, time-dependent entrainment rates directly (Tournigand, Taddeucci, et al., 2017), or relate instantaneous source mass fluxes to evolving plume heights (e.g. Hreinsdóttir et al., 2014; Dürig et al., 2015, 2018). In its current prototype state, obtaining accurate segmentation and tracking of target structures coupled with application of robust quantitative analysis is in practice user intensive. For example, care is required in the choice of weighting parameters for the tracking optimization (Section B3) and in quality checks of the retrieved radius and temperature profiles (Section 3.7) prior to and during curve-fitting analysis. The uncertainty and effort cost in these steps, however, could be eliminated with a combination of further development of the tracking algorithm, using sophisticated data inversion techniques (e.g. Cerminara et al., 2015) or, for example, ensemble averaging multiple tracks over appropriately chosen time scales. A trained neural network, furthermore, would likely be both more accurate and more efficient than our spectral clustering algorithm, but requires training using an appropriately labeled and sufficiently extensive data set. Therefore perhaps the most effective use of our tracking algorithm is in the creation of labeled and curated tracking data sets that could be used to train supervised machine learning algorithms such as R-CNNs or LSTM-CNNs. Most other steps in our workflow, such as spatial projection, atmospheric profile removal, and curve analysis are then in principle straight forward to fully automate. Moreover, the same principles for capturing time-dependent eruption dynamics apply for other monitoring techniques for which relationships between measured source properties and column dynamic states can be established, such as Doppler radar (e.g. Bonadonna et al., 2011; Donnadieu, 2012; Freret-Lorgeril et al., 2020), video or UV imagery (e.g. Woitischek, Mingotti, et al., 2021; Woitischek, Edmonds, & Woods, 2021), or acoustic monitoring (e.g. De Angelis et al., 2019; Watson et al., 2021). We underscore the conclusions of other recent studies and emphasize the value of multi-instrument, community data sets to create rapid-analysis AI tools for real time monitoring of volcanic columns (Cigna et al., 2020; Dye & Morra, 2020; Witsil & Johnson, 2020; Korolev et al., 2021; Guerrero Tello et al., 2022; Wilkes et al., 2022).

6 Conclusions

We have used ground-based, thermal infrared imagery to quantitatively link volcanic eruption column temperature decay to the power law predictions of canonical theories for steady plumes and discrete thermals (Morton et al., 1956; Turner, 1962), and have furthermore linked the spatiotemporal evolution of thermal buoyancy to unsteady temporal fluctuations in the vent heat flux. To do so, we have developed a novel structure tracking algorithm based on spectral clustering, which tracks the evolution in height and time of individual coherent, turbulent vortices. We have focused our analysis on three events of varying unsteady character at Sabancaya Volcano, Peru, including a steady plume, a quasi-pulsatory starting plume, and a transient Vulcanian explosion. Our efforts support the following key results and conclusions:

1. The sustained plume can be reasonably described by an appropriate average power law behavior corresponding to predictions from steady plume theory ($\Delta T \propto z^{-5/3}$), despite significant fluctuation at the source vent.
2. The two relatively more unsteady or transient events are characterized by thermal evolutions broadly consistent with an initial thermal-like pulse ($\Delta T \propto z^{-3}$) followed by a transition towards steady plume-like behavior during sustained or decaying phases, though neither event obviously follows expected behavior for a starting plume.
3. Power law analysis of column evolutions with height and time requires careful, independent estimation of the column virtual source location, which may be achieved with greater accuracy with e.g. ensemble or time averaging over time scales much shorter than the time scale for evolution of the mean flow τ_μ.
4. Quantitative analysis of time-averaged images is appropriate specifically when the averaging time is long compared to the column rise time (τ_{rise}; which may correspond either to the column buoyancy level or height of the camera view field), but short compared to the time scale for evolution in source conditions (τ_μ). Where these criteria are not met, the time-averaged image properties (e.g. column radius, apparent virtual source location, temperature decay) will be dominated by the largest and most energetic source pulses, and will not capture complex evolutions in source conditions for events that are unsteady in space and time.

5. Unsupervised machine learning techniques are an effective tool for quantitative and high-temporal-resolution analysis of unsteady column dynamics. They are also useful for generating labeled training data sets which facilitate the development of fast, effective neural networks for real-time monitoring and analysis.

From the above conclusions, we highlight the following key implications:

1. Both the relative magnitude and timing of variations in source mass, momentum, and buoyancy fluxes drive evolutions between steady-plume, unsteady plume, or discrete thermal rise regimes, with corresponding variations in entrainment rate and buoyancy evolution.
2. Quantitative measures of source unsteadiness must therefore be developed that predict variations in entrainment and which account for both the magnitude and timing of source fluctuations. Here we have proposed the Mean State Pulsation Number Pu_μ, which incorporates information on fluctuations on time scales comparable to the overturn time of the largest turbulent eddies, as well as evolutions in the mean source fluxes (i.e. over timescales significantly longer than the eddy overturn time). In our definition, we argue that volcanic columns with $Pu_\mu \ll 1$ will have entrainment rates that match those of steady plumes, whereas for $Pu_\mu \rightarrow 1$, variations in vent source fluxes are of sufficient magnitude that pulses of erupted material will rise and entrain air in a manner similar to that of discrete thermals, with corresponding modifications to gravitational stability and rise height.
3. Laboratory experiments and numerical modeling of unsteady columns can provide critical insight on systematic variations in entrainment as a function of Pu_μ, or similar unsteadiness metrics. An essential goal in such efforts is to link unsteady entrainment parameterizations in integral models to both local balances of momentum and buoyancy and the history of source unsteadiness.

Open Research

Satellite atmospheric profile products from the MODIS/Terra and AIRS/Aqua satellites were obtained from NASA at https://www.earthdata.nasa.gov (Teixeira, 2013; Borbas, 2015) Digitial Elevation Model data used in Figure 2 were obtained from the Alaska Satellite Facility (ASF-DAAC, 2015). Thermal data (brightness temperatures, optical flow velocity fields, and atmospheric profiles) and results of analysis (e.g. structure tracking positions, retrieved temperature and radius profiles, curve fitting results, and calculated source unsteadiness metrics) are available at figshare under Creative Commons Licence (CC BY 4.0) at:

https://doi.org/10.6084/m9.figshare.21936582.

A code package containing the core functions of the workflow is licensed under the GNU General Public License v3.0, and published on Github: https://github.com/colinrr/locust.git (Rowell, 2023)

Appendix A Methods Workflow

In Figure A1 we show a graphical overview of the methods workflow, highlighting the manuscript sections containing details on each.

Appendix B Tracking of Coherent Turbulent Structures

Here we provide additional details on the key steps in the feature tracking algorithm as summarized in Figure 5. Further documentation and code can be found in the code repository listed in the Open Research Section.

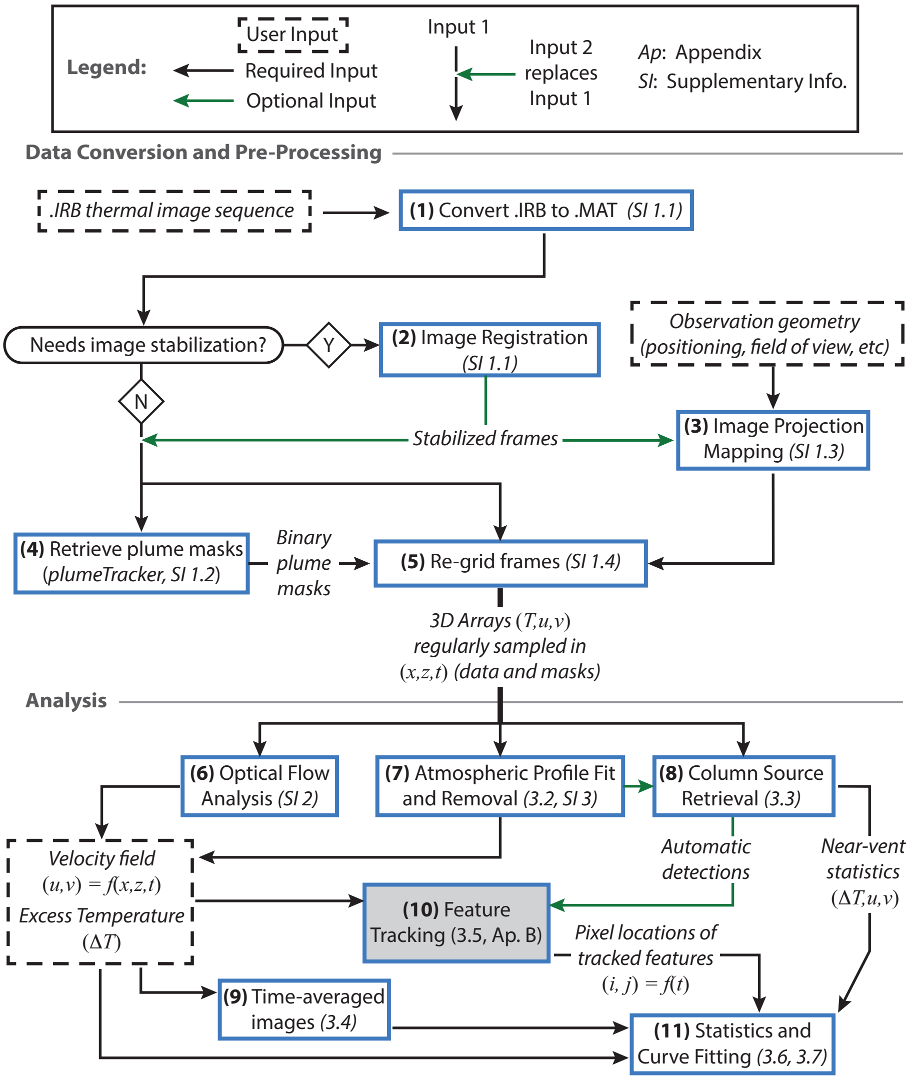

Figure A1. Overview of data processing and analysis workflow. See text and Supplementary Information for details.

B1 Structure Tracking: Initialization

Initiating structure tracking requires selection of a starting frame and tracking window (sub-region of the frame containing a structure of interest), as shown in Figure 5a. These may be automatically chosen using the source detection method of Section 3.3 (a pulse detection identifies the starting frame, and the source detection window defines the initial region of interest). In practice, for the relatively small subset of events presented here, we initially detect sources of interest using this method, and where needed refine the choice of exact start frame and detection window location manually to ensure a testing data set for the tracking algorithm with structures that are both clearly detected and relatively long-lived and continuous in terms of visibility at the column exterior. Optionally, it is also possible to define an initial guess (shown by the purple outline in Figure 5a) to target a specific structure. This initial guess is used as a surrogate "tracking memory" for the starting frame optimization (see below for a full explanation of optimization and tracking memory). The code performs initial clustering and optimization on the data values contained in the detection window (see Sections B2 and B3 below). An important step here is to estimate the preferred number of clusters n_{c0}, which can be determined from the approximate size of the structures of interest. For example, for a circular eddy of radius L, column radius R, and an initial detection window covering the full width of the visible column (i.e. window length $l \approx 2R$), then the ratio of the eddy area to that of the rectangular detection window in the thermal image is

$$\frac{1}{n_{c0}} = \frac{\pi L^2}{4aR^2}, \tag{B1}$$

where $a = h/l$ is the aspect ratio of the detection window. For $L = R/2$ (typical for the largest eddies) and window aspect ratios of 0.5 to 1, this gives an optimal number of clusters $2.5 \lesssim n_{c0} \lesssim 5$. Similar logic holds for a detection window of arbitrary size, and in practice the best tracking results were indeed obtained for $2 \leq n_c \leq 5$.

B2 Structure Tracking: Spectral Clustering

Consistent with Equation 7 we use five variables to guide a physically-based spectral clustering step: horizontal and vertical position (x, z), excess temperature ΔT, and horizontal and vertical velocity (u, v). For each frame, these values are retrieved for all pixels within the tracking window. We filter out the coldest pixels (30% by default), which usually correspond to column edges or colder, lower velocity column elements outside the large vortices of interest. Next, remaining variables are normalized by their standard deviation across all pixels. We then apply weights to each variable to emphasize their relative importance for choosing clusters. Excess temperature and vertical velocity are the most important properties for characterizing the heat flux carried by rising structures. The spatial position variables, while necessary to ensure coherent (i.e. not fragmented) clusters, are the least important in distinguishing and tracking coherent rising structures. Accordingly, default weights for the cluster variables are $W(x, z, \Delta T, u, v) = (0.5, 0.5, 2, 1, 1.5)$. After weighting, we then perform spectral clustering for a range of n_c (generally $n_{c0} - 1$ to $n_{c0} + 1$), recording pixel locations and the average values of the five target variables for all resulting clusters.

B3 Structure Tracking: Cluster Optimization

The optimization step selects the cluster containing the set of pixels carrying the highest apparent heat flow (i.e. clusters that are high excess temperature and velocity and contain the largest possible number of pixels), that also minimizes differences with the tracked structure of previous time steps (i.e. the tracking memory). In particular, for all candidate clusters obtained during the clustering step, we calculate the objective function

$$\Omega = M + \lambda ||P||, \tag{B2}$$

where M is a "data" term that optimizes for maximum heat flow, P is the "prior" term which evaluates similarity with the tracked cluster from previous time steps, and λ is a scalar regularization parameter which tunes the relative importance of the two terms. The algorithm tracks the cluster that minimizes Ω. The data optimization term

$$M = 1 - \left[\frac{\bar{T}_i \bar{V}_i A_i}{max(\bar{T}\bar{V}A)}\right], \tag{B3}$$

where the subscript i denotes a single candidate cluster, and $\bar{T}_i$, $\bar{V}_i$, and A_i are the normalized mean pixel temperature, mean vertical velocity, and area (expressed as number of pixels) of the cluster, respectively. The prior term P is the calculated difference between candidate clusters and instances of the tracked structure from previous frames, and contains four contributions:

$$\|P\| = \left[(w_T P_T)^2 + (w_V P_V)^2 + (w_A P_A)^2 + (w_D P_D)^2\right]^{1/2}. \tag{B4}$$

The scalars w_T, w_V, w_A, w_D are weights for the individual prior terms with default values of $(0.5, 0.25, 0.5, 2)$, respectively. These weights are distinct from the weights used for clustering in Section B2. The components of the prior term measure similarity with the tracked structure of previous time steps for temperature (P_T), vertical velocity (P_V), area (P_A), and position (P_D). These terms are, respectively,

$$P_T = \frac{|\sum_{j=1}^{n_{px}} T_j - \overline{\sum_{j=1}^{n_p x} T_{P,j}}|}{\overline{\sum_{j=1}^{n_p x} T_{P,j}}}, \tag{B5}$$

$$P_V = \frac{\|\bar{V} - \bar{V_P}\|}{\bar{V_P}}, \tag{B6}$$

$$P_A = \frac{\|A - A_P\|}{A_P}, \tag{B7}$$

$$P_D = \frac{1}{n_{px}\epsilon C_{95}} \sum_{j=1}^{n_{px}} D_j, \tag{B8}$$

where n_{px} is the number of pixels in a candidate cluster, subscript j denotes a pixel (i.e. summation over all pixels in a cluster), subscript P denotes the memory or "prior" structure. The first three prior terms (Equations B5 to B7) ensure that the target structure has similar temperature, velocity, and size to the tracked structure of previous frames. D_j is the computed Euclidean distance of a candidate cluster pixel to the nearest pixel of the prior tracked structure, and is zero for pixels that overlap with the prior structure. In the normalization factor for $P_{D,i}$, $C_{95} = v_{95}\frac{dt}{dx}$ is the pixel grid Courant Number, v_{95} is the 95th percentile (for the full video sequence) of Optical Flow vertical velocity, and ϵ is a scalar tolerance with a default value of 2.5. As an example, for a maximum rise velocity of 30 m/s, pixel dimension $dx = 3$ m, frame interval $dt = 0.1$ s, and tolerance $\epsilon = 2.5$, the grid speed $\frac{dx}{dt}$ is 75 m/s and $\epsilon C_{95} = 1$, which indicates that tracked structures are required to move at most about 1 pixel per frame on average. The final term $P_{D,i}$ therefore favors tracked structures for which the motion between frames does not greatly exceed realistic flow velocities. The Courant number velocity tolerance is also imposed in the warping step used to obtain the final tracked structure, as described below.

The prior values (T_P, V_P, A_P, D) are calculated using instances of the tracked structure from n_P previous frames (or for all previous frames at early time when fewer than n_P frames have been tracked). Importantly, the memory must capture a sufficient number of frames to both robustly detect the structure motion and to average out physical and unphysical noise in the detected clusters related to small fluctuations in the velocity field and in the Courant number. This requirement prevents minor variations in the detected clusters from sending the tracking algorithm off course from the target eddy structure. Here n_P is calculated internally using the modal Courant number as $n_P = |(u, v)|_{mode} dt/dx$, where $|(u, v)|_{mode}$ is the estimated mode of the absolute Optical Flow velocity field for all frames, which is generally much slower than the motion of the relatively fast and hot large turbulent eddies. For the three video sequences shown here, n_P varies from 5 to 9. (T_P, V_P, A_P) are determined from the mean value of the tracked structure across the previous n_P frames. To determine D, the prior structure is considered to include pixels that were included in the tracked structure for at least 3 of the preceding n_P frames. The resulting "prior mask" gives the outline of the structure from the previous time step and is outlined in dark blue in Figure 5d.

As with many optimization schemes, the choice of weights in the clustering and optimizations steps, and the regularization λ can have a significant impact on results. The default weights as listed were chosen based on the relative importance of variables. For example, the hottest features are consistently those emerging from the leading front of overturning structures, so temperature is the most robust measure for tracking the motion of the front and therefore has the largest weight. Also as a consequence, the location of structure fronts are generally robustly tracked using the default weight parameters. Capturing accurately the shape of structures is more challenging and in many instances required manual adjustment of the weights, or possible the regularization λ or velocity tolerance ϵ. User suggestions for the adjustment of weights are included in the code documentation.

B4 Structure Tracking: Memory Warping and Tracking Window Update

To obtain the final tracked structure, we first select pixels that are within the distance tolerance ϵC_{95} of the prior mask boundary, for pixels that are external (not included in the prior mask) and internal (included in the prior mask). This selection represents a physical limit for how much the turbulent structure should translate or deform within a single time step, based on their flow velocity. For pixels that lie within the new selected cluster, we add pixels outside the prior mask that are within the distance limit, and similarly remove prior pixels that are within this limit but are not in the selected cluster. This results in a small layer of pixels added at the structure leading edge and removed at the structure trailing tail, as shown in Figure 5d. The "warped mask" resulting from this process is defined as the "tracked structure" for the current frame, and is added to the prior memory as the most recent frame. Next, since tracked structures evolve in both position and shape, the position memory of the structure pixels from the previous n_P frames must also be updated at each time step in order for the distance optimization term P_D give accurate results (cumulative motions of about 1 to 5 pixels are typical over n_P frames). This step creates a prediction for the position and size of the structure in the next time step that will be used in the next cluster optimization. The pixel positions in structure memory are updated by translating them using the Optical Flow velocity field and rounding to the nearest pixel position. Finally, the tracking window position and size must be updated, since the turbulent structures both move and grow in size with progressive entrainment. The window changes position following the tracked structure centroid while maintaining a minimum distance from its leading edge, and adjusts its size to maintain the optimum number of clusters given by Equation B1. The aspect ratio is also adjusted to continually match the tracked structure. It is otherwise rectangular, except where truncated by encountering the boundaries of the column mask (Figure 5d). Changes in the tracking window between time steps are again limited by the velocity tolerance ϵC_{95}.

B5 Structure Tracking: Pixel Exclusion

For the purpose of data analysis on the tracked structures, it is preferable to ensure that any given pixel is only ever included in a single tracked structure so that all tracked structures have entirely separate data and their boundaries do not overlap. Initial tracked structures do overlap in some cases, typically when the trailing tail of a structure captures a part of the following structure, and generally not by more than a few percent of all tracked pixels. To correct for this overlap, we perform a final step to manually exclude pixels that are included in more than one structure. For each tracked structure, all pixels that are also included in a following structure at any given time step are removed.

Acknowledgments

We thank the researchers and staff of the Instituto Geológico Minero y Metalúrgico (INGEMMET) in Arequipa, Peru for hosting and facilitating our visit and fieldwork. Thanks to Dr. Franck Donnadieu at Laboratoire Magmas et Volcans, Clermont, France for organizing our participation in the field campaign. Special thanks to Professor John Stix at McGill University for the use of his thermal camera and assisting with data conversion. This work was supported by an NSERC Discovery Grant and NSERC Discovery Accelerator to AMJ.

We would like to thank and acknowledge the efforts of Dr. Mark Woodhouse and two anonymous reviewers, each of whom provided conscientious and thoughtful comments which greatly improved the manuscript.

References

Anilkumar, A. (1993, May). Geological implications and applications of high-velocity two-phase flow experiments. *Journal of Volcanology and Geothermal Research*, *56*(1-2), 145–160. doi: 10.1016/0377-0273(93)90056-W

ASF-DAAC. (2015). Dataset: ALOS PALSAR_Radiometric_Terrain_Corrected_high_res; Includes Material © JAXA/METI 2007. doi: 10.5067/Z97HFCNKR6VA

Aubry, T. J., Engwell, S., Bonadonna, C., Carazzo, G., Scollo, S., Van Eaton, A. R., ... Schmidt, A. (2021, May). The Independent Volcanic Eruption Source Parameter Archive (IVESPA, version 1.0): A new observational database to support explosive eruptive column model validation and development. *Journal of Volcanology and Geothermal Research*, 107295. doi: 10.1016/j.jvolgeores.2021.107295

Aubry, T. J., Jellinek, A. M., Carazzo, G., Gallo, R., Hatcher, K., & Dunning, J. (2017, September). A new analytical scaling for turbulent wind-bent plumes: Comparison of scaling laws with analog experiments and a new database of eruptive conditions for predicting the height of volcanic plumes. *Journal of Volcanology and Geothermal Research*, *343*, 233–251. doi: 10.1016/j.jvolgeores.2017.07.006

Bhamidipati, N., & Woods, A. W. (2017, December). On the dynamics of starting plumes. *Journal of Fluid Mechanics*, *833*, R2. doi: 10.1017/jfm.2017.762

Bloomfield, L. J., & Kerr, R. C. (2000, December). A theoretical model of a turbulent fountain. *Journal of Fluid Mechanics*, *424*, 197–216. doi: 10.1017/S0022112000001907

Bombrun, M., Jessop, D., Harris, A., & Barra, V. (2018, February). An algorithm for the detection and characterisation of volcanic plumes using thermal camera imagery. *Journal of Volcanology and Geothermal Research*, *352*, 26–37. doi: 10.1016/j.jvolgeores.2018.01.006

Bonadonna, C., Costa, A., Folch, A., & Koyaguchi, T. (2015, January). Chapter 33 - Tephra Dispersal and Sedimentation. In H. Sigurdsson (Ed.), *The Encyclopedia of Volcanoes (Second Edition)* (pp. 587–597). Amsterdam: Academic Press. doi: 10.1016/B978-0-12-385938-9.00033-X

Bonadonna, C., Genco, R., Gouhier, M., Pistolesi, M., Cioni, R., Alfano, F., ... Ripepe, M. (2011). Tephra sedimentation during the 2010 Eyjafjallajökull eruption (Iceland) from deposit, radar, and satellite observations. *Journal of Geophysical Research: Solid Earth*, *116*(B12). doi: 10.1029/2011JB008462

Borbas, E. (2015). *MOD07_L2 MODIS/Terra Temperature and Water Vapor Profiles 5-Min L2 Swath 5km.* Level 1 and Atmosphere Archive and Distribution System (LAADS). doi: 10.5067/MODIS/MOD07_L2.006

Brand, B. D., & Clarke, A. B. (2009, March). The architecture, eruptive history, and evolution of the Table Rock Complex, Oregon: From a Surtseyan to an energetic maar eruption. *Journal of Volcanology and Geothermal Research*, *180*(2), 203–224. doi: 10.1016/j.jvolgeores.2008.10.011

Bursik, M. (2001). Effect of wind on the rise height of volcanic plumes. *Geophysical Research Letters*, *28*(18), 3621–3624. doi: 10.1029/2001GL013393

Carazzo, G., Kaminski, E., & Tait, S. (2006, January). The route to self-similarity in turbulent jets and plumes. *Journal of Fluid Mechanics*, *547*, 137–148. doi: 10.1017/S002211200500683X

Carazzo, G., Kaminski, E., & Tait, S. (2008a, November). On the dynamics of volcanic columns: A comparison of field data with a new model of negatively buoyant jets. *Journal of Volcanology and Geothermal Research*, *178*(1), 94–103. doi: 10.1016/j.jvolgeores.2008.01.002

Carazzo, G., Kaminski, E., & Tait, S. (2008b). On the rise of turbulent plumes: Quantitative effects of variable entrainment for submarine hydrothermal vents, terrestrial and extra terrestrial explosive volcanism. *J. Geophys. Res.*, *113*(B9201). doi: 10.1029/2007JB005458

Carey, R. J., Houghton, B. F., & Thordarson, T. (2009, July). Abrupt shifts between wet and dry phases of the 1875 eruption of Askja Volcano: Microscopic evidence for macroscopic dynamics. *Journal of Volcanology and Geothermal Research*, *184*(3), 256–270. doi: 10.1016/j.jvolgeores.2009.04.003

Carlson, R. E., & Fritsch, F. N. (1985, April). Monotone Piecewise Bicubic Interpolation. *SIAM J. Numer. Anal.*, *22*(2), 386–400. doi: 10.1137/0722023

Caulfield, C. P., & Woods, A. W. (1998, April). Turbulent gravitational convection from a point source in a non-uniformly stratified environment. *Journal of Fluid Mechanics*, *360*, 229–248. doi: 10.1017/S0022112098008623

Cerminara, M., Esposti Ongaro, T., Valade, S., & Harris, A. J. L. (2015, July). Volcanic plume vent conditions retrieved from infrared images: A forward and inverse modeling approach. *Journal of Volcanology and Geothermal Research*, *300*, 129–147. doi: 10.1016/j.jvolgeores.2014.12.015

Chojnicki, K. N., Clarke, A. B., Adrian, R. J., & Phillips, J. C. (2014, December). The flow structure of jets from transient sources and implications for modeling short-duration explosive volcanic eruptions. *Geochemistry, Geophysics, Geosystems*, *15*(12), 4831–4845. doi: 10.1002/2014GC005471

Chojnicki, K. N., Clarke, A. B., Phillips, J. C., & Adrian, R. J. (2015a, August). The evolution of volcanic plume morphology in short-lived eruptions. *Geology*, *43*(8), 707–710. doi: 10.1130/G36642.1

Chojnicki, K. N., Clarke, A. B., Phillips, J. C., & Adrian, R. J. (2015b, February). Rise dynamics of unsteady laboratory jets with implications for volcanic plumes. *Earth and Planetary Science Letters*, *412*, 186–196. doi: 10.1016/j.epsl.2014.11.046

Cigna, F., Tapete, D., & Lu, Z. (2020, January). Remote Sensing of Volcanic Processes and Risk. *Remote Sensing*, *12*(16), 2567. doi: 10.3390/rs12162567

Ciriello, F., & Hunt, G. R. (2020, June). Analytical solutions and virtual origin corrections for forced, pure and lazy turbulent plumes based on a universal entrainment function. *Journal of Fluid Mechanics*, *893*. doi: 10.1017/jfm.2020.225

Clarke, A. B. (2013). Unsteady explosive activity. In R. M. C. Lopes, S. A. Fagents, & T. K. P. Gregg (Eds.), *Modeling Volcanic Processes: The Physics and Mathematics of Volcanism* (pp. 129–152). Cambridge: Cambridge University Press. doi: 10.1017/CBO9781139021562.007

Clarke, A. B., Esposti Ongaro, T., & Belousov, A. (2015, January). Chapter 28 - Vulcanian Eruptions. In H. Sigurdsson (Ed.), *The Encyclopedia of Volcanoes (Second Edition)* (pp. 505–518). Amsterdam: Academic Press. doi: 10.1016/B978-0-12-385938-9.00028-6

Clarke, A. B., Neri, A., Voight, B., Macedonio, G., & Druitt, T. H. (2002). Computational modelling of the transient dynamics of the August 1997 Vulcanian explosions at Soufrière Hills Volcano, Montserrat: Influence of initial conduit conditions on near-vent pyroclastic dispersal. *Geological Society, London, Memoirs*, *21*(1), 319–348. doi: 10.1144/GSL.MEM.2002.021.01.15

Clarke, A. B., Phillips, J., & Chojnicki, K. (2009, August). An investigation of vulcanian eruption dynamics using laboratory analogue experiments and scaling analysis. In T. Thordarson, S. Self, G. Larsen, S. K. Rowland, & A. Hoskuldsson (Eds.), *Studies in Volcanology: The Legacy of George Walker* (First ed., pp. 155–166). The Geological Society of London on behalf of The International Association of Volcanology and Chemistry of the Earth's Interior. doi: 10.1144/IAVCEl002.8

Clarke, A. B., Voight, B., Neri, A., & Macedonio, G. (2002, February). Transient dynamics of vulcanian explosions and column collapse. *Nature*, *415*(6874), 897–901. doi: 10.1038/415897a

Cole, P. D., Neri, A., & Baxter, P. J. (2015, January). Chapter 54 - Hazards from Pyroclastic Density Currents. In H. Sigurdsson (Ed.), *The Encyclopedia of Volcanoes (Second Edition)* (pp. 943–956). Amsterdam: Academic Press. doi: 10.1016/B978-0-12-385938-9.00054-7

Contini, D., & Robins, A. (2004, July). Experiments on the rise and mixing in neutral crossflow of plumes from two identical sources for different wind directions. *Atmospheric Environment*, *38*(22), 3573–3583. doi: 10.1016/j.atmosenv.2004.03.043

Coppola, D., Valade, S., Masias, P., Laiolo, M., Massimetti, F., Campus, A., … Valdivia, D. (2022, January). Shallow magma convection evidenced by excess degassing and thermal radiation during the dome-forming Sabancaya eruption (2012–2020). *Bull Volcanol*, *84*(2), 16. doi: 10.1007/s00445-022-01523-1

Cover, T., & Hart, P. (1967, January). Nearest neighbor pattern classification. *IEEE Transactions on Information Theory*, *13*(1), 21–27. doi: 10.1109/TIT.1967.1053964

Craske, J. (2017, April). The properties of integral models for planar and axisymmetric unsteady jets. *IMA Journal of Applied Mathematics*, *82*(2), 305–333. doi: 10.1093/imamat/hxw043

Craske, J., & van Reeuwijk, M. (2016, April). Generalised unsteady plume theory. *Journal of Fluid Mechanics*, *792*, 1013–1052. doi: 10.1017/jfm.2016.72

De Angelis, S., Diaz-Moreno, A., & Zuccarello, L. (2019, January). Recent Developments and Applications of Acoustic Infrasound to Monitor Volcanic Emissions. *Remote Sensing*, *11*(11), 1302. doi: 10.3390/rs11111302

Degruyter, W., & Bonadonna, C. (2012). Improving on mass flow rate estimates of volcanic eruptions. *Geophysical Research Letters*, *39*(16). doi: 10.1029/2012GL052566

Degruyter, W., & Bonadonna, C. (2013, September). Impact of wind on the condition for column collapse of volcanic plumes. *Earth and Planetary Science Let-*

ters, *377–378*, 218–226. doi: 10.1016/j.epsl.2013.06.041

Delichatsios, M. A. (1979, July). Time similarity analysis of unsteady buoyant plumes in neutral surroundings. *Journal of Fluid Mechanics*, *93*(2), 241–250. doi: 10.1017/S0022112079001877

Devenish, B. J., Rooney, G. G., Webster, H. N., & Thomson, D. J. (2010, March). The Entrainment Rate for Buoyant Plumes in a Crossflow. *Boundary-Layer Meteorol*, *134*(3), 411–439. doi: 10.1007/s10546-009-9464-5

Donnadieu, F. (2012). *Volcanological applications of Doppler radars: A review and examples from a transportable pulse radar in L-band.* INTECH Open Access Publisher.

Dürig, T., Gudmundsson, M. T., Dioguardi, F., Woodhouse, M., Björnsson, H., Barsotti, S., … Walter, T. R. (2018, July). REFIR- A multi-parameter system for near real-time estimates of plume-height and mass eruption rate during explosive eruptions. *Journal of Volcanology and Geothermal Research*, *360*, 61–83. doi: 10.1016/j.jvolgeores.2018.07.003

Dürig, T., Gudmundsson, M. T., Karmann, S., Zimanowski, B., Dellino, P., Rietze, M., & Büttner, R. (2015, November). Mass eruption rates in pulsating eruptions estimated from video analysis of the gas thrust-buoyancy transition—a case study of the 2010 eruption of Eyjafjallajökull, Iceland. *Earth, Planets and Space*, *67*, 180. doi: 10.1186/s40623-015-0351-7

Dye, B. C., & Morra, G. (2020, August). Machine learning as a detection method of Strombolian eruptions in infrared images from Mount Erebus, Antarctica. *Physics of the Earth and Planetary Interiors*, *305*, 106508. doi: 10.1016/j.pepi.2020.106508

Freret-Lorgeril, V., Gilchrist, J., Donnadieu, F., Jellinek, A. M., Delanoë, J., Latchimy, T., … Valade, S. (2020, March). Ash sedimentation by fingering and sediment thermals from wind-affected volcanic plumes. *Earth and Planetary Science Letters*, *534*, 116072. doi: 10.1016/j.epsl.2020.116072

Gaudin, D., Taddeucci, J., Scarlato, P., Harris, A., Bombrun, M., Del Bello, E., & Ricci, T. (2017, February). Characteristics of puffing activity revealed by ground-based, thermal infrared imaging: The example of Stromboli Volcano (Italy). *Bull Volcanol*, *79*(3), 24. doi: 10.1007/s00445-017-1108-x

Gerbe, M.-C., & Thouret, J.-C. (2004, August). Role of magma mixing in the petrogenesis of tephra erupted during the 1990–98 explosive activity of Nevado Sabancaya, southern Peru. *Bull Volcanol*, *66*(6), 541–561. doi: 10.1007/s00445-004-0340-3

Gilchrist, J. T. (2021). *Sediment waves and the gravitational stability of explosive eruption columns and ash clouds : Towards a new classification of explosive eruptions* (Doctoral dissertation, University of British Columbia). doi: 10.14288/1.0402355

Gilchrist, J. T., & Jellinek, A. M. (2021, September). Sediment waves and the gravitational stability of volcanic jets. *Bull Volcanol*, *83*(10), 64. doi: 10.1007/s00445-021-01472-1

Girault, F., Carazzo, G., Tait, S., Ferrucci, F., & Kaminski, É. (2014, May). The effect of total grain-size distribution on the dynamics of turbulent volcanic plumes. *Earth and Planetary Science Letters*, *394*, 124–134. doi: 10.1016/j.epsl.2014.03.021

Global Volcanism Program. (2013). *Sabancaya (354006).* Smithsonian Institution.

Gonnermann, H. M., & Manga, M. (2007). The Fluid Mechanics Inside a Volcano. *Annual Review of Fluid Mechanics*, *39*(1), 321–356. doi: 10.1146/annurev.fluid.39.050905.110207

Guerrero Tello, J. F., Coltelli, M., Marsella, M., Celauro, A., & Palenzuela Baena, J. A. (2022, January). Convolutional Neural Network Algorithms for Semantic Segmentation of Volcanic Ash Plumes Using Visible Camera Imagery. *Remote Sensing*, *14*(18), 4477. doi: 10.3390/rs14184477

Harris, A. (2013). *Thermal Remote Sensing of Active Volcanoes: A User's Manual.* Cambridge University Press.

Hewett, T. A., Fay, J. A., & Hoult, D. P. (1971, September). Laboratory experiments of smokestack plumes in a stable atmosphere. *Atmospheric Environment (1967)*, *5*(9), 767–789. doi: 10.1016/0004-6981(71)90028-X

Houghton, B., White, J. D. L., & Van Eaton, A. R. (2015, January). Chapter 30 - Phreatomagmatic and Related Eruption Styles. In H. Sigurdsson (Ed.), *The Encyclopedia of Volcanoes (Second Edition)* (pp. 537–552). Amsterdam: Academic Press. doi: 10.1016/B978-0-12-385938-9.00030-4

Hreinsdóttir, S., Sigmundsson, F., Roberts, M. J., Björnsson, H., Grapenthin, R., Arason, P., … Óladóttir, B. A. (2014, March). Volcanic plume height correlated with magma-pressure change at Grímsvötn Volcano, Iceland. *Nature Geoscience*, *7*(3), 214–218. doi: 10.1038/ngeo2044

Hunt, G. R., & Kaye, N. G. (2001, May). Virtual origin correction for lazy turbulent plumes. *Journal of Fluid Mechanics*, *435*, 377–396.

Ilanko, T., Pering, T. D., Wilkes, T. C., Choquehuayta, F. E. A., Kern, C., Moreno, A. D., … McGonigle, A. J. S. (2019, December). Degassing at Sabancaya volcano measured by UV cameras and the NOVAC network. *Volcanica*, *2*(2), 239–252. doi: 10.30909/vol.02.02.239252

Jaupart, C., & Tait, S. (1990, January). Dynamics of eruptive phenomena. *Reviews in Mineralogy and Geochemistry*, *24*(1), 213–238.

Jessop, D. E., Gilchrist, J., Jellinek, A. M., & Roche, O. (2016, November). Are eruptions from linear fissures and caldera ring dykes more likely to produce pyroclastic flows? *Earth and Planetary Science Letters*, *454*, 142–153. doi: 10.1016/j.epsl.2016.09.005

Jessop, D. E., & Jellinek, A. M. (2014, June). Effects of particle mixtures and nozzle geometry on entrainment into volcanic jets. *Geophysical Research Letters*, *41*(11), 3858–3863. doi: 10.1002/2014GL060059

Jia, H., Ding, S., Xu, X., & Nie, R. (2014, June). The latest research progress on spectral clustering. *Neural Comput & Applic*, *24*(7), 1477–1486. doi: 10.1007/s00521-013-1439-2

Kaminski, E., Tait, S., & Carazzo, G. (2005, March). Turbulent entrainment in jets with arbitrary buoyancy. *Journal of Fluid Mechanics*, *526*, 361–376. doi: 10.1017/S0022112004003209

Kaye, N. B., & Scase, M. M. (2011, August). Straight-sided solutions to classical and modified plume flux equations. *Journal of Fluid Mechanics*, *680*, 564–573. doi: 10.1017/jfm.2011.214

Korolev, S., Sorokin, A., Urmanov, I., Kamaev, A., & Girina, O. (2021, January). Classification of Video Observation Data for Volcanic Activity Monitoring Using Computer Vision and Modern Neural NetWorks (on Klyuchevskoy Volcano Example). *Remote Sensing*, *13*(23), 4747. doi: 10.3390/rs13234747

Koyaguchi, T., Suzuki, Y. J., & Kozono, T. (2010). Effects of the crater on eruption column dynamics. *Journal of Geophysical Research: Solid Earth*, *115*(B7). doi: 10.1029/2009JB007146

Lherm, V., & Jellinek, A. M. (2019, December). Experimental constraints on the distinct effects of ash, lapilli, and larger pyroclasts on entrainment and mixing in volcanic plumes. *Bull Volcanol*, *81*(12), 73. doi: 10.1007/s00445-019-1329-2

Linden, P. F. (2000). Convection in the Environment. In G. K. Batchelor, H. K. Moffatt, & M. G. Worster (Eds.), *Perspectives in fluid dynamics: A collective introduction to current research* (pp. 289–343). Cambridge University Press.

MacQueen, J. (1967). *Some methods for classification and analysis of multivariate observations.*

Morton, B. R. (1959, January). Forced plumes. *Journal of Fluid Mechanics*, *5*(1), 151–163. doi: 10.1017/S002211205900012X

Morton, B. R. (1971). The choice of conservation equations for plume models. *Journal of Geophysical Research (1896-1977)*, *76*(30), 7409–7416. doi: 10.1029/JC076i030p07409

Morton, B. R., Taylor, G. I., & Turner, J. S. (1956, January). Turbulent gravitational convection from maintained and instantaneous sources. *Proceedings of the Royal Society of London. Series A. Mathematical and Physical Sciences*, *234*(1196), 1–23. doi: 10.1098/rspa.1956.0011

National Academies of Sciences, E., and Medicine. (2017). *Volcanic Eruptions and Their Repose, Unrest, Precursors, and Timing.* Washington, DC: The National Academies Press. doi: 10.17226/24650

Ottino, J. M. (1989). *The Kinematics of Mixing: Stretching, Chaos, and Transport.* Cambridge University Press.

Patrick, M. R. (2007). Dynamics of Strombolian ash plumes from thermal video: Motion, morphology, and air entrainment. *Journal of Geophysical Research: Solid Earth*, *112*(B6). doi: 10.1029/2006JB004387

Patrick, M. R., Harris, A. J. L., Ripepe, M., Dehn, J., Rothery, D. A., & Calvari, S. (2007, June). Strombolian explosive styles and source conditions: Insights from thermal (FLIR) video. *Bull Volcanol*, *69*(7), 769–784. doi: 10.1007/s00445-006-0107-0

Prata, F., & Rose, B. (2015, January). Chapter 52 - Volcanic Ash Hazards to Aviation. In H. Sigurdsson (Ed.), *The Encyclopedia of Volcanoes (Second Edition)* (pp. 911–934). Amsterdam: Academic Press. doi: 10.1016/B978-0-12-385938-9.00052-3

Priestley, C. H. B., & Ball, F. K. (1955). Continuous convection from an isolated source of heat. *Quarterly Journal of the Royal Meteorological Society*, *81*(348), 144–157. doi: 10.1002/qj.49708134803

Richards, J. M. (1965, January). Puff motions in unstratified surroundings. *Journal of Fluid Mechanics*, *21*(1), 97–106. doi: 10.1017/S002211206500006X

Rowell, C. R. (2023, June). *Locally Optimized Clustering for Unsteady Structure Tracking.*

Rowell, C. R., Jellinek, A. M., & Gilchrist, J. T. (2023, January). Dataset: Tracking volcanic plume thermal evolution and eruption source unsteadiness in ground-based thermal imagery using spectral-clustering [Dataset]. doi: 10.6084/m9.figshare.21936582

Samaniego, P., Rivera, M., Mariño, J., Guillou, H., Liorzou, C., Zerathe, S., . . . Scao, V. (2016, September). The eruptive chronology of the Ampato–Sabancaya volcanic complex (Southern Peru). *Journal of Volcanology and Geothermal Research*, *323*, 110–128. doi: 10.1016/j.jvolgeores.2016.04.038

Saxena, A., Prasad, M., Gupta, A., Bharill, N., Patel, O. P., Tiwari, A., . . . Lin, C.-T. (2017, December). A review of clustering techniques and developments. *Neurocomputing*, *267*, 664–681. doi: 10.1016/j.neucom.2017.06.053

Scase, M. M. (2009). Evolution of volcanic eruption columns. *Journal of Geophysical Research: Earth Surface*, *114*(F4). doi: 10.1029/2009JF001300

Scase, M. M., Caulfield, C. P., Dalziel, S. B., & Hunt, J. C. R. (2006, September). Time-dependent plumes and jets with decreasing source strengths. *Journal of Fluid Mechanics*, *563*, 443–461. doi: 10.1017/S0022112006001212

Sharma, B. K., Kumar, A., & Murthy, V. M. (2010, March). Evaluation of seismic events detection algorithms. *J Geol Soc India*, *75*(3), 533–538. doi: 10.1007/s12594-010-0042-8

Shi, J., & Malik, J. (2000, August). Normalized cuts and image segmentation. *IEEE Transactions on Pattern Analysis and Machine Intelligence*, *22*(8), 888–905. doi: 10.1109/34.868688

Smith, C. M., Gaudin, D., Van Eaton, A. R., Behnke, S. A., Reader, S., Thomas, R. J., . . . Cimarelli, C. (2021). Impulsive Volcanic Plumes Generate Volcanic Lightning and Vent Discharges: A Statistical Analysis of Sakurajima Volcano in 2015. *Geophysical Research Letters*, *48*(11), e2020GL092323. doi: 10.1029/2020GL092323

Sparks, R. S. J. (1986). The dimensions and dynamics of volcanic eruption columns. *Bull Volcanol*, *48*(1), 3–15. doi: 10.1007/BF01073509

Sparks, R. S. J., & Wilson, L. (1976, August). A model for the formation of ignimbrite by gravitational column collapse. *Journal of the Geological Society*, *132*(4), 441–451. doi: 10.1144/gsjgs.132.4.0441

Sun, D., Roth, S., & Black, M. J. (2014, January). A Quantitative Analysis of Current Practices in Optical Flow Estimation and the Principles Behind Them. *Int J Comput Vis*, *106*(2), 115–137. doi: 10.1007/s11263-013-0644-x

Teixeira, J. (2013). *GES DISC Dataset: AIRS/Aqua L2 Standard Physical Retrieval (AIRS+AMSU) V006 (AIRX2RET 006).* AIRS Science Team.

Tournigand, P.-Y., Fernández, J. J. P., Taddeucci, J., Perugini, D., Sesterhenn, J., & Palladino, D. M. (2019, February). Time evolution of transient volcanic plumes: Insights from fractal analysis. *Journal of Volcanology and Geothermal Research*, *371*, 59–71. doi: 10.1016/j.jvolgeores.2018.12.007

Tournigand, P.-Y., Peña Fernandez, J. J., Taddeucci, J., Perugini, D., & Sesterhenn, J. (2017, April). Fractal analysis: A new tool in transient volcanic ash plume characterization. In *EGU General Assembly Conference Abstracts* (Vol. 19, p. 14643).

Tournigand, P.-Y., Taddeucci, J., Gaudin, D., Fernández, J. J. P., Bello, E. D., Scarlato, P., . . . Yokoo, A. (2017, December). The Initial Development of Transient Volcanic Plumes as a Function of Source Conditions. *Journal of Geophysical Research: Solid Earth*, *122*(12), 9784–9803. doi: 10.1002/2017JB014907

Tritton, D. J. (1988). *Physical fluid dynamics* (2nd ed.). Springer Science & Business Media.

Turner, J. S. (1962, July). The ‘starting plume’ in neutral surroundings. *J. Fluid Mech.*, *13*(3), 356–368. doi: 10.1017/S0022112062000762

Turner, J. S. (1969). Buoyant Plumes and Thermals. *Annual Review of Fluid Mechanics*, *1*(1), 29–44. doi: 10.1146/annurev.fl.01.010169.000333

Turner, J. S. (1973). *Buoyancy Effects in Fluids.* Cambridge: Cambridge University Press. doi: 10.1017/CBO9780511608827

Turner, J. S. (1986, December). Turbulent entrainment: The development of the entrainment assumption, and its application to geophysical flows. *Journal of Fluid Mechanics*, *173*, 431–471. doi: 10.1017/S0022112086001222

Turner, J. S., & Taylor, G. I. (1957, April). Buoyant vortex rings. *Proceedings of the Royal Society of London. Series A. Mathematical and Physical Sciences*, *239*(1216), 61–75. doi: 10.1098/rspa.1957.0022

Valade, S. A., Harris, A. J. L., & Cerminara, M. (2014, May). Plume Ascent Tracker: Interactive Matlab software for analysis of ascending plumes in image data. *Computers & Geosciences*, *66*, 132–144. doi: 10.1016/j.cageo.2013.12.015

van Reeuwijk, M., & Craske, J. (2015, November). Energy-consistent entrainment relations for jets and plumes. *Journal of Fluid Mechanics*, *782*, 333–355. doi: 10.1017/jfm.2015.534

van Reeuwijk, M., Salizzoni, P., Hunt, G. R., & Craske, J. (2016, November). Turbulent transport and entrainment in jets and plumes: A DNS study. *Phys. Rev. Fluids*, *1*(7), 074301. doi: 10.1103/PhysRevFluids.1.074301

van Reeuwijk, M., Vassilicos, J. C., & Craske, J. (2021, February). Unified description of turbulent entrainment. *Journal of Fluid Mechanics*, *908*, A12. doi: 10.1017/jfm.2020.836

von Luxburg, U. (2007, December). A tutorial on spectral clustering. *Stat Comput*, *17*(4), 395–416. doi: 10.1007/s11222-007-9033-z

Watson, L. M., Dunham, E. M., Mohaddes, D., Labahn, J., Jaravel, T., & Ihme, M. (2021). Infrasound Radiation From Impulsive Volcanic Eruptions: Nonlinear Aeroacoustic 2D Simulations. *Journal of Geophysical Research: Solid Earth*, *126*(9), e2021JB021940. doi: 10.1029/2021JB021940

Webb, E. B., Varley, N. R., Pyle, D. M., & Mather, T. A. (2014, May). Thermal imaging and analysis of short-lived Vulcanian explosions at Volcán de Colima, Mexico. *Journal of Volcanology and Geothermal Research*, *278–279*, 132–145. doi: 10.1016/j.jvolgeores.2014.03.013

Wilkes, T. C., Pering, T. D., & McGonigle, A. J. S. (2022, November). Semantic segmentation of explosive volcanic plumes through deep learning. *Computers & Geosciences*, *168*, 105216. doi: 10.1016/j.cageo.2022.105216

Witsil, A. J. C., & Johnson, J. B. (2020, September). Volcano video data characterized and classified using computer vision and machine learning algorithms. *Geoscience Frontiers*, *11*(5), 1789–1803. doi: 10.1016/j.gsf.2020.01.016

Woitischek, J., Edmonds, M., & Woods, A. W. (2021). On the Fluctuations in Volcanic Plumes. *Geophysical Research Letters*, *48*(3), e2020GL090594. doi: 10.1029/2020GL090594

Woitischek, J., Mingotti, N., Edmonds, M., & Woods, A. W. (2021, May). On the use of plume models to estimate the flux in volcanic gas plumes. *Nat Commun*, *12*(1), 2719. doi: 10.1038/s41467-021-22159-3

Woodhouse, M. J., Hogg, A. J., Phillips, J. C., & Sparks, R. S. J. (2013). Interaction between volcanic plumes and wind during the 2010 Eyjafjallajökull eruption, Iceland. *Journal of Geophysical Research: Solid Earth*, *118*(1), 92–109. doi: 10.1029/2012JB009592

Woodhouse, M. J., Phillips, J. C., & Hogg, A. J. (2016, May). Unsteady turbulent buoyant plumes. *Journal of Fluid Mechanics*, *794*, 595–638. doi: 10.1017/jfm.2016.101

Woods, A. W. (1988, June). The fluid dynamics and thermodynamics of eruption columns. *Bull Volcanol*, *50*(3), 169–193. doi: 10.1007/BF01079681

Woods, A. W. (1995). The dynamics of explosive volcanic eruptions. *Reviews of Geophysics*, *33*(4), 495–530. doi: 10.1029/95RG02096

Woods, A. W. (2010, January). Turbulent Plumes in Nature. *Annu. Rev. Fluid Mech.*, *42*(1), 391–412. doi: 10.1146/annurev-fluid-121108-145430

Zimanowski, B., Büttner, R., Dellino, P., White, J. D. L., & Wohletz, K. H. (2015, January). Chapter 26 - Magma–Water Interaction and Phreatomagmatic Fragmentation. In H. Sigurdsson (Ed.), *The Encyclopedia of Volcanoes (Second Edition)* (pp. 473–484). Amsterdam: Academic Press. doi: 10.1016/B978-0-12-385938-9.00026-2